Fall 2021

Implementation of Stereo Digital Image Correlation for In-Plane Strain Measurements to Quantify the Anisotropic Behavior, Plastic Flow, and Strain Hardening of Extruded Aluminum Alloy

Farzana Yasmeen

IMPLEMENTATION OF STEREO DIGITAL IMAGE CORRELATION FOR IN-PLANE STRAIN MEASUREMENTS TO QUANTIFY THE ANISOTROPIC BEHAVIOR, PLASTIC FLOW, AND STRAIN HARDENING OF EXTRUDED ALUMINUM ALLOY

by

Farzana Yasmeen

Bachelor of Science
Bangladesh University of Engineering & Technology, 2009

Master of Science
University of South Carolina, 2016

Submitted in Partial Fulfillment of the Requirements

For the Degree of Doctor of Philosophy in

Mechanical Engineering

College of Engineering and Computing

University of South Carolina

2021

Accepted by:

Michael Sutton, Major Professor

Xiaomin Deng, Committee Member

Addis A. Kidane, Committee Member

Dimitris Rizos, Committee Member

Tracey L. Weldon, Interim Vice Provost and Dean of the Graduate School

DEDICATION

This work is dedicated to my caring husband, beloved parents, and adorable daughter, who have been a constant source of support and encouragement during the challenges of my life.

ACKNOWLEDGEMENTS

This research was made possible through the assistance and continuous support of many different individuals and organizations. I wish to express my sincere appreciation to my advisor Professor Michael Sutton. His excellent guidance, teaching, leadership, encouraging words, patience, and extensive knowledge motivate me throughout the day. I have learned scientific knowledge and skill from him and how to approach and solve problems effectively and efficiently. I am blessed to work with such an outstanding advisor, and he is an invaluable treasure for my whole life.

My deepest gratitude is also reserved for Dr. Dimitris Rizos for his technical advice and financial support. I would like to particularly thank Dr. Xiaomin Deng for his research guidance and suggestions. I would also like to thank my thesis committee member, Dr. Addis A. Kidane, for his invaluable guidance. Special thanks to Dr.Jamil khan, Dr.Kevin Huang, and Dr. M Faisal Haider for sharing their valuable academic experience and knowledge.

I would also like to acknowledge graduate and undergraduate students in the Mechanics Materials and Nondestructive Evaluation group at the University of South Carolina.

ABSTRACT

The efficient use of metals is important in various industries, including aerospace, automotive, and energy systems. In each case, the type and range of combined loading conditions can be quite different. The approaches to stress analysis of such complex engineering components and assemblies often are limited to elastic conditions. For those cases where components are relatively thin, elastic-plastic conditions are present; there is continuing interest in assessing the accuracy of analytic and computational models for combined loading conditions. In such cases, experiments performed with axial and shear loads (e.g., tension-torsion) provide baseline data regarding the relationship between applied stresses and specimen strains. Since stereo digital image correlation (StereoDIC) has been used extensively in recent years to measure full-field surface deformations, including both surface strains and displacements, the methodology provides quantitative data regarding the specimen's non-uniform deformation response. In particular, the full-field and non-contacting capabilities of StereoDIC are especially advantageous when applied to thin-walled tubular specimens subjected to multimodal loading.

The first part of this work investigates the anisotropic behavior of two longitudinally extruded Al6061-T6 bars obtained from the same manufacturer. Since longitudinal extrusion is known to affect material isotropy, a comprehensive series of mechanical characterization experiments, including torsion for cylindrical specimens and tension for flat dog-bone specimens extracted at different orientations from the rod

materials were performed. The Barlat Yld91 yield function, which requires six parameters for generally mixed-mode predictions, was employed in this study. The Newton-Raphson numerical method was used to solve the nonlinear set of Barlat equations to determine six anisotropic parameters from the yield stresses acquired from uniaxial and simple torsion testing. The results show that the extruded Al6061-T6 bars have significant anisotropic behavior.

The second part of this work presents the effect of stress state and loading path on the elastic-plastic response and strain hardening of Al6061-T6 by performing combined tension-torsion, uniaxial tension, and simple torsion experiments on tubular specimens. Specialty grips and precision boring tools were developed for cylindrical specimen manufacturing and tension-torsion testing. StereoDIC was employed to measure reliable average surface strains while also providing full-field measurements to identify anomalies in material response due to machining imperfections and/or loading conditions. Mixed-mode loading experiments were performed in load-control mode using an electromechanical tension-torsion test frame. Results from proportional tension torsion experiments with stress ratio, β, defined as the ratio shear stress /normal stress in the range $0 \leq \beta \leq \infty$ were obtained. By using plastic work/dissipation to determine equivalent strain from multiaxial stress states, measurements demonstrated that the yield stress defined by the Von Mises effective stress vs. equivalent strain response varied with β by up to 14%. Conversely, when using the Barlat Yld91 anisotropic yield function to define modified effective stress, direct comparison of the Barlat effective stress versus equivalent strain data for all mixed-mode loading experiments to the uniaxial tension data demonstrated that the Barlat Yld91 effective stress versus equivalent strain was within ±4% of the uniaxial

data for all β, confirming that an anisotropic yield function should be employed to accurately predict plastic flow and strain hardening behavior in extrusions.

The third part of the work presents a combined theoretical and experimental material hardening behavior under only torsion loading for the same aluminum Al6061-T6 longitudinally extruded bars. The theoretical elastic, plastic and total shear strains due to applied shear stress are determined using incremental plasticity theory. A constitutive numerical model is developed for both isotropic (von Mises) and anisotropic (Barlat'91) yield criteria. Assuming isotropic strain hardening formulations to describe the post-yield behavior for both (von Mises and Barlat'91) yield criteria, the von Mises isotropic model predictions are shown to either underestimate or overestimate the data by up to 25% for both extrusions. Conversely, the constitutive model using the anisotropic (Barlat'91) yield criteria is in excellent agreement, with deviations from the experimental measurements by less than 5%, again demonstrating that plastic anisotropy is essential for accurate prediction of the mechanical behavior of longitudinally extruded Al6061-T6 bars.

Finally, an experimental investigation of stress-strain was conducted to understand the effect of non-proportional tension-torsion loading on several specimens. The experimental measurements for selected non-proportional loading experimental are presented, and recommendations for further investigation of the stress-strain behavior under nonproportional tension-torsion loading are provided.

TABLE OF CONTENTS

LIST OF TABLES

LIST OF FIGURES

CHAPTER 1

INTRODUCTION

1.1 BACKGROUND AND MOTIVATION

Present-day many automotive, aerospace, biomedical, and appliance industries emphasize the need for more efficient use of metals (Fig 1.1) in applications where reliability and safety are of paramount importance. Aircraft, shipbuilding, automotive, steam, and gas turbine industries require methods of analysis that are more accurate than any now in existence. Since weight reduction and increasing durability are important design considerations, it is necessary to know the yield behavior of materials, including both the yield surface and the elastoplastic behavior of structures that are loaded beyond the elastic range. Since the stress-strain response is nonlinear in the elastoplastic range, accurate predictions are more difficult, especially when the structure undergoes mixed-mode loading conditions. This dissertation presents a combined experimental and theoretical study regarding the response of longitudinally extruded Al6061-T6 bar material. By performing accurate machining of the bar stock into tubular and flat specimen geometries, a series of combined tension and torsion loading experiments are conducted. By subjecting the specimens to deformations in the elastic-plastic range and evaluating both isotropic and anisotropic yield criteria, the importance of incorporating anisotropy in theoretical models is clearly demonstrated. In the remainder of the chapter, motivation for this work is presented while also outlining the contributions presented in the following chapters.

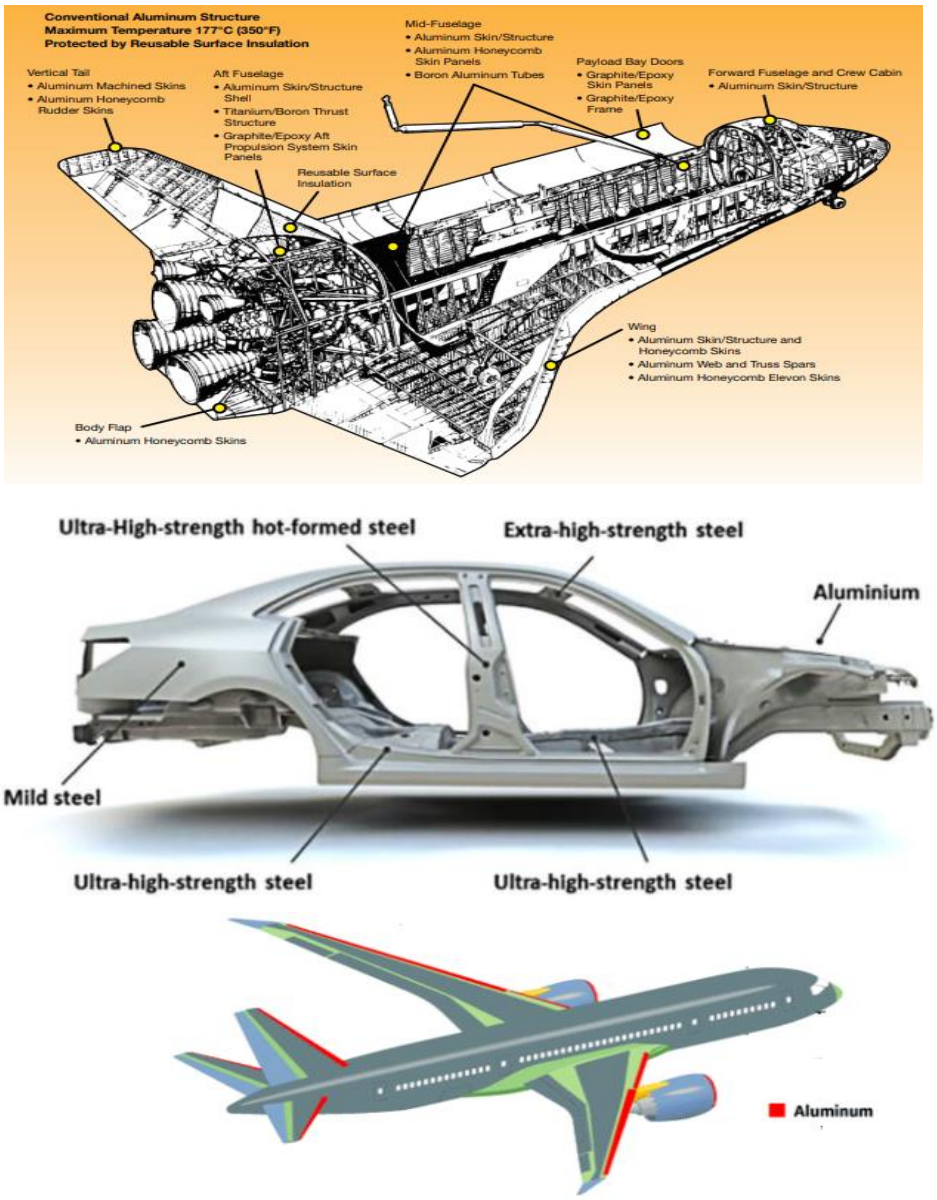

Figure 1.1 Use of metals in industries (a) Space shuttle: orbit structure (*www.nasa.gov*), (b) Car body consisting of components manufactured with different materials (Asnafi et al. 2019), (c) Aluminum in Boeing 787 (aviation.stackexchange.com)

1.2 SCOPE OF THIS DISSERTATION

Aluminum 6061 is one of the most broadly used aluminum alloys. Its weldability and formability make it suitable for a wide range of applications. Its high strength and corrosion resistance are particularly useful in architectural, structural, and motor vehicle applications

(thomasnet.com). The list of uses is exhaustive, but some significant extruded 6061 aluminum tube applications are architectural extrusions, aircraft parts, truck frames, bicycle frames, scuba tanks, electrical fittings, and automotive parts (hydro.com). Since the anisotropic yielding and hardening behavior of axially extruded Al6061-T6 tubular material has not been studied extensively, this dissertation work focuses on quantifying the anisotropic and hardening behavior of longitudinally extruded cylindrical Al 6061-T6 bar specimens that were obtained from McMaster-Carr.

The first objective of this study is to analyses the effects of anisotropy on the yielding behavior of two longitudinally extruded solid bar Al6061-T6 specimens, designated as MT1 and MT2. To predict anisotropic response, a six-parameter anisotropic yield function developed by Barlat, designated as the Barlat Yld91 criterion, is employed. All six Barlat Yld91 parameters are determined using data from (a) uniaxial tension experiments on specimens extracted from different directions in each extrusion and (b) simple torsion experiments for longitudinal tubular specimens machined from the bar stock. As part of the prediction process, isotropic strain hardening is used, an assumption that is consistent with those of most previous investigators. The post-yielding hardening parameters are determined from tensile experiments on a specimen extracted from the longitudinal direction in the extrusion.

The second objective of this study is to experimentally measure the plastic flow and strain hardening behavior of extruded Al6061-T6 MT1 tubular material by performing uniaxial tension, simple torsion, and combined tension-torsion loading of specimens machined from the extruded bar stock conditions. To ensure that the measured surface strain data on each thin-walled tubular specimen is a reliable average value, without local

spikes, gradients, or oscillations that may occur due to machining effects or loading changes, StereoDIC is used to acquire full-field measurements of in-plane strains. By inspecting the full-field measurements to identify anomalies and remove flawed data, there is increased confidence that the data is consistent with the underlying theory that is used to predict material response. Thus, a part of the scope of the research is to successfully demonstrate the use of StereoDIC for surface measurements on cylindrical specimens subjected to combined tension-torsion loading.

The third objective of this study is to predict elastic, plastic, and total shear strains during the simple torsional loading of tubular specimens machined from the extruded bar stock. To predict response, both incremental plasticity theory and the Barlat Yld91 anisotropic/ Von Mises isotropic yield criterion are used, where the elastic behavior is assumed to be consistent with the isotropic form of Hooke's law. As in the first objective, the six parameters for the Barlat Yld91 criterion are determined for the new set of the longitudinally extruded bar using the same specimen geometries. For comparison, the von Mises isotropic yield function with isotropic post-yield strain hardening is also used to predict the experimentally measured response. It is noted that the assumed isotropic hardening model is validated by comparing calculated elastic-plastic shear strains to model predictions for a specimen undergoing simple torsion loading. Fig. 1.2 presents and summarizes these research scopes and objectives.

1.3 OUTLINE OF THIS DISSERTATION

This dissertation is divided into a total of six chapters, including the current chapter that presents the scope of the work in this study. The introductory Chapter 2 presents a review

of earlier work, including a brief background for the StereoDIC measurement methodology.

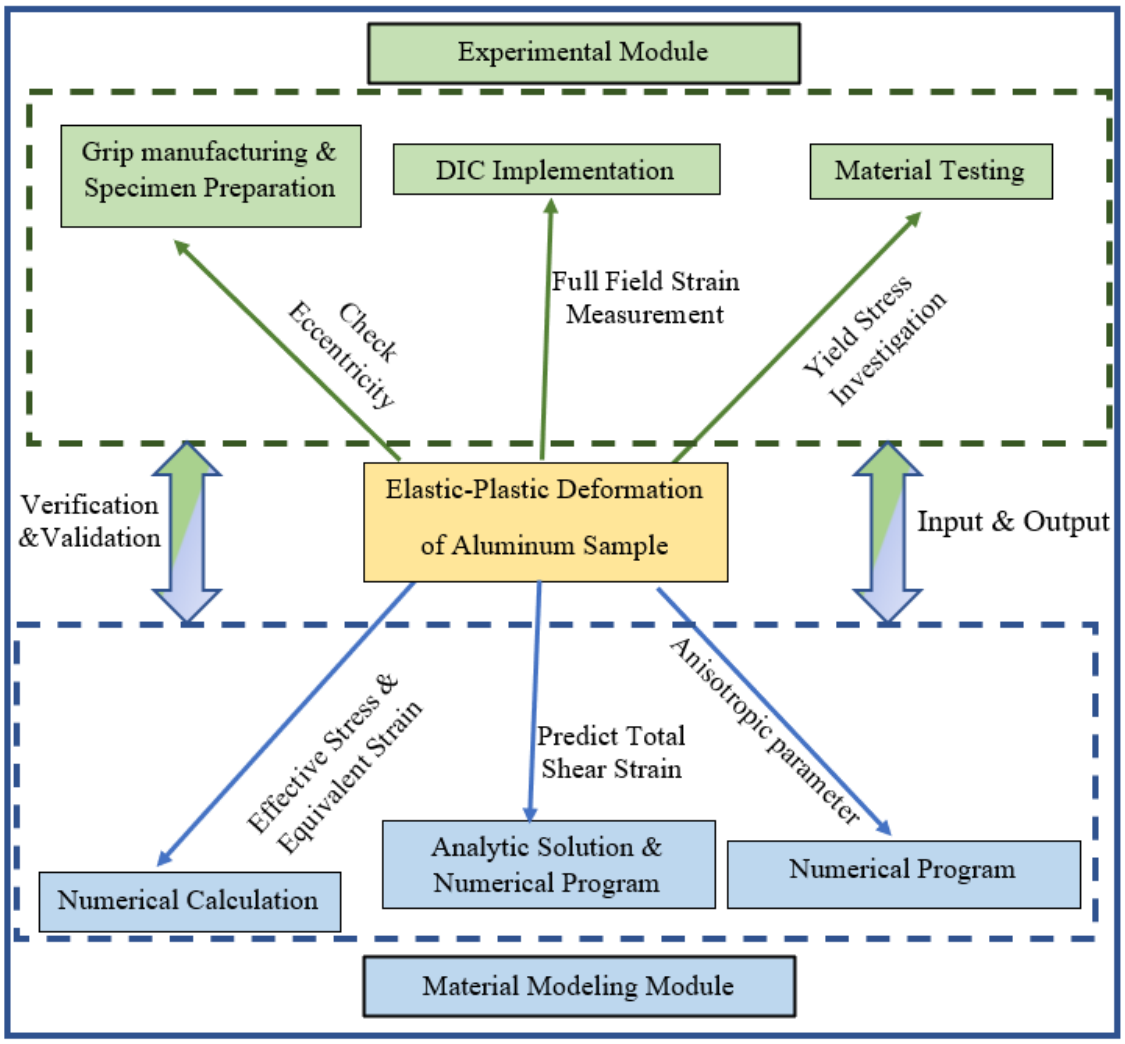

Figure 1.2 Research Scopes and objectives flow chart

Chapter 3 presents a review of the underlying theoretical concepts, including elasticity, isotropic and anisotropic yielding, and plasticity. As part of the review, modeling of anisotropic and isotropic material behavior and the procedures employed for parameter identification are discussed. Chapter 4 describes experimental issues including (a) load cell calibration, (b) detailed materials selection and (c) specimen geometries and machining

processes, (d) locations and orientations within bar stock for the uniaxial tension, simple torsion, and combined tension-torsion specimens and (e) descriptions for how loading applied for specimens in both MT1 and MT2 specimens. Chapter 5 presents the experimental data, along with a comparison of experimental results and model predictions. Chapter 6 provides a brief discussion of the key experimental issues resolved during this study. Finally, Chapter 7 presents conclusions from our research, summarizes the findings, and Chapter 8 outlines recommendations for future work along with the significant contributions of this research.

CHAPTER 2

LITERATURE REVIEW

2.1 INTRODUCTION

Since material behavior under linear elasticity conditions is straightforward and well established, the focus of this review will be on elastic-plastic deformations under combined loading where there is a continuing interest in assessing the accuracy of analytic and computational models. In such cases, experiments performed with materials that are subjected to multi-modal stress state conditions are important to provide baseline data regarding the relationship between applied stresses and specimen strains. Since there has been a number of experimental, theoretical, and computational studies focused on the plastic flow and strain hardening of metallic materials, this chapter presents a sampling of the relevant previous research regarding material behavior, including yield, plastic deformations, and the experimental method used in this study, digital image correlation techniques.

2.2 REVIEW WORK ON YIELD CRITERIA AND HARDENING RULE

Several experimental studies have been completed with thin-walled tubular specimens subjected to combined tension-torsion loading to improve understanding of yielding and plastic flow in selected material systems. Researchers seeking to improve understanding of the elastic-plastic behavior of nominally isotropic materials have identified different types

of hardening behavior. Tresca (1864) published his results on punching and extrusion experiments, formulating the Tresca yield criterion, which is also known as the maximum shear stress criteria. Saint-Venant (1870) and Levy (1870) used the Tresca criterion in their developments of the theory for rigid-perfectly plastic solid. Another well-known yield criterion was proposed by Ludwig on Mises (1913) on the basis of purely mathematical considerations. Currently, the yield functions of Tresca (1864) and von Mises (1913) are widely used for isotropic materials. In 1980, another popular yield criterion that is a generalization of the von Mises criterial was developed for isotropic materials and is designated the Hosford yield criterion. A number of researchers have used these isotropic yield functions to describe the yielding behavior of an aluminum alloy, including Haltom et al. (2013), Papasidero et al. (2015), Scales et al. (2016)) and their references.

Since manufacturing processes such as heat treatment, rolling, and extrusion may induce anisotropic material behavior, researchers have developed and applied anisotropic yield functions to predict how such material deforms under multi-axial loading (Hill, 1948,1979,1990;1993; 1998 Hosford, 1979; Gotoh, M.1977, Logan and Hosford, 1980; Barlat and Lian, 1989; Barlat et al., 1991, 1997a,1997b, 2003,2005; Karafillis and Boyce, 1993; Bron and Besson, 2004; Cazacu et al., 2006; Plunkett et al., 2008, Bai and Wierzbicki, 2008) to describe and predict the effects of initial anisotropy associated with changes in mechanical properties. One of the most significant criteria was developed by Prof. Rodney Hill. Hill (1948,1979) proposed a widely used quadratic yield criterion that includes six material parameters obtained from uniaxial tensile and shear experiments for the three principal directions. Later, Hill (1990;1993) presented a modified version of this model for sheet metal with in-plane anisotropy. Barlat et al. (1991, 1997a, 1997b, 2003,

2005) suggested different sets of anisotropic yield functions such as Yld91, Yld2000-2d, Yld 2004-8d, and Yld2004-18p, etc. Barlat et al. (1991) developed a Yld91 six-parameter yield function to model the anisotropy of aluminum. He presented the applicability of his Yld91 criteria for AA 2008-T4 and AA2024-T3 sheets and showed good agreement between the experiment and predicted results. Later Barlat extended the approach to linear transformation-based anisotropic yield functions Yld2004-8d and Yld2004-18p. Barlat et al. (2004) showed the effectiveness of his Yld2004-18p criteria for AA 6111-T4 and AA2090-T3 sheet samples, demonstrating that Yld2004-18p is a suitable constitutive model for the above-mentioned metal.

In addition, to yield criteria, several researchers, including Ludwik (1909), Hollomon (1945), Voce (1948), Swift (1952), and Ludwigson (1971), focused on the flow rule and work hardening behavior for nominally isotropic materials, with limited studies regarding the effect of anisotropy on strain hardening in aluminum alloys (Stoughton and Yoon (2009), Rousselier et al. (2010)).

2.3 PLASTICITY THEORY

After yielding, almost all real materials undergo plastic deformation. Hencky (1924) interpreted the von Mises criterion and demonstrated plastic yielding occurs when the elastic shear-strain energy reaches a critical value. Hencky's (1924) theory with Ilyushin (1947, 1961, 1963) has been considered an early theory of plasticity known as the deformation theory of plasticity. In this theory, the total strain can be expressed as a function of total stress. Such constitutive structure, typical for nonlinear elastic deformation in materials such as rubber, is in general inappropriate for plastic deformation since strain depends on both stress and stress history rather than simply a function of stress. Even with

this observation, the deformation theory of plasticity is applicable in the case of proportional or simple loading, cases where all stress components increase proportionally, or nearly so, without elastic unloading ever occurring (Kachanov 1971). The theory was especially efficient in bifurcation studies and the determination of necking and buckling loads (Hutchinson, 1974). The commonly accepted theory is the flow theory of plasticity (Hill 1950, 1967, 1979, Lubliner 1990) which is used in most analytical and computational studies of plastic deformation of metals and geomaterials. In this model, plastic deformation is a history-dependent phenomenon characterized by the nonlinearity and irreversibility of underlining physical processes (Bell, 1968). Consequently, in the flow theory of plasticity, the rate of strain can be determined from the rate of stress and the variables describing the current state of the material. The overall response is determined incrementally by integrating the rate-type constitutive and field equations along a given path of loading or deformation (Lubarda and Lee, 1981; Lubarda and Krajcinovic, 1995; Lubarda,1999).

2.4 REVIEW WORK OF COMBINED LOADING IN THE ELASTIC-PLASTIC REGION

Hecker (1976) has demonstrated that the Von Mises (1913) isotropic hardening model works well for initial yielding. However, there are increasing differences when predicting subsequent yielding when the second load path is in a different direction from the first one. IIyushin and Lensky (1968) reported on the elastic-plastic behavior of material undergoing mixed-mode stress states, noting that the Von Mises criteria works well in the elastic range but shows increasingly different effective stress-effective strain behavior in the plastic range with changes in mixed mode stress state. Ohashi and Tokuda (1973) reported experimental effective stress-equivalent strain data for tubular mild steel specimens

subjected to different loading paths, showing that hardening curves exhibit considerable deviation for different loading paths. Meguid and Malvern (1983) have shown that considerable differences exist between the Von Mises effective stress vs. equivalent plastic strain data for proportional and non-proportional combined torsion-tension, simple tension, and simple torsion loading paths when performing experiments using mild steel cylindrical specimens. Additional background regarding experimental investigations under combined stresses that have been performed to obtain the initial and subsequent yield behavior for different materials under different loading conditions can be found in Ivey (1961), Bertsch and Fmdley (1962), Phillips et al. (1972, 1974), Phillips, & Juh-Ling,(1972). Phillips and Tang(1974), Phillips and Moon (1977), Khan et al. (2009, 2010), Chen et al. (2019), Scales et al. (2019), and their references.

2.5 REVIEW OF ELASTIC-PLASTIC MODELS

Fourmeau et al. (2011) used high-strength AA7075-T651 plate material to investigate the effect of plastic anisotropy on the mechanical behavior of rolled aluminum plate experimentally and numerically. They used the Barlat Yld2004-18p anisotropic yield function with experimental measurements to demonstrate that the plate exhibited significant anisotropic behavior that was in good agreement with the Barlat Yld2004-18p predictions, deviating substantially from predictions using the von Mises isotropic yield criterion. Tardif & Kyriakides (2012) developed a 3D FE anisotropic (Yld2004-18p) and isotropic version (Von Mises and Hosford) model to extrapolate the experimental material response of the tensile test at larger strains of Al-6061-T6 sheet metal. In their studies, anisotropy was characterized by a set of uniaxial and biaxial tests conducted in parallel using an 18-parameter non-quadratic Yld2004-18p yield function. Material hardening was

obtained by comparing the measured and calculated force-displacement response and validated by the corresponding measured strains and the shape of the material neck. According to their study, the Yld2004-18p model matches well with experimental data, whereas the Von Mises and Hosford models exhibit larger deviation due from the measurements due to their isotropic nature. Farzana et al. (2021) studied the plastic flow and strain hardening behavior of extruded Al6061-T6 tubular material for a wide range of uniaxial tension, simple torsion, and combined tension-torsion loading conditions experimentally. The author used both isotropic and anisotropic versions of the yield functions for comparison to the experimental results, confirming the Barlat anisotropic yield function provides an accurate prediction of the plastic flow and strain hardening behavior in longitudinal extrusions. In another study, Farzana et al. (2021a) presented a combined theoretical and experimental investigation of plastic anisotropy and material hardening behavior under torsion loading for two longitudinally extruded aluminum Al6061-T6 circular bars. Incremental plasticity, isotropic and anisotropic yield functions, and an isotropic hardening rule are used to determine the theoretical elastic, plastic, and total shear strains from the applied shear stress. Results showed that the Barlat anisotropic yield criteria are in excellent agreement with experimental evidence for both extrusions. Due to a large number of previous investigations regarding the elastic-plastic behavior of aluminum, the listing provided below is believed to be those that are most directly applicable to our studies and include Korkolis and Kyriakides (2008a,2008b, 2009, 2011), Korkolis et al. (2010), Giagmouris et al. (2010), Seidt and Gilat (2013), Zhang(2015), Kuwabara et al. (2017), Esmaeilpour et al. (2017, 2018), Pahlevanpour et al. (2019), Mooney et al. (2019), and Kondori (2019) Rahmaan et al. (2020) and their references.

According to our literature survey, only a few studies have been published regarding the anisotropic behavior of extruded aluminum alloys.. Fjeldly and Roven (1996) studied the behavior of extruded plate of AA7108 alloy using texture analysis and uniaxial tension tests and showed that the alloy exhibits strong anisotropy in the plastic region. Lademo et al. (1999) characterized the mechanical response of extruded rectangular plates of aluminum alloys AA7108 and AA6063, demonstrating that the alloys exhibit significant anisotropy. They estimated the anisotropic yield functions of Hill (1948), Barlat and Lian (1989), Karafillis and Boyce (1993), and Barlat et al. (1997) as part of their study. Achani et al. (2009) presented their study of plastic anisotropy in extruded bars of aluminum alloys AA7003-T6 and AA6063-T6 by performing uniaxial tension tests in different directions. They calibrated both the Yld2004-18p and Yld2000-2d yield criteria, demonstrating that both alloys exhibit strong anisotropy.

Sutton et al. (1996) presented an approach based on incremental plasticity theory to determine the stresses and the associated elastic and plastic strains from the total strain measured on a sample surface. Kim et al. (2013) developed the virtual fields method (VFM) to determine the constitutive parameters by calculating the stress fields from the heterogeneous strain fields. They proved that selecting the proper hardening law is important to predict the actual stress-strain relation. More background on this subject can be found in Pannier et al. (2006), Avril et al. (2008), Coppieters et al. (2011), and Coppieters & Kuwabara (2014).

2.6 DIGITAL IMAGE CORRELATION METHOD

Digital image correlation (DIC) is a computer-vision-based, non-contacting measurement technique capable of measuring full-field deformation on a specimen's surface (Sutton

(2009)) subjected to general loading and/or temperature condition. DIC originated and was devised for planar surfaces undergoing in-plane deformations in the early 1980s (Peters (1981), Sutton (1983)), and is most often designated as 2D-DIC. In principle, 2D-DIC gives accurate results when a nominally planar specimen is subjected to in-plane mechanical loading. In such cases, the planar surfaces experience in-plane deformations. If a single viewing camera is placed perpendicular to the specimen, then the measured deformations would reflect the true deformations under ideal conditions. Later these ideas were further developed and shown to be experimentally effective by Sutton et al. (1986) and Chu et al. (1985). Nowadays, 2D-DIC continues to be used to measure strain on a planar surface in a wide range of industry and engineering studies (Geymonat and Pagano (2003), Liu et al. (2019), Dzaye et al. (2019), del Rey Castillo et al. (2019)), though its use has declined considerably due to developments of StereoDIC (3D-DIC) in the 1990s. In the early 1990s (Kahn-Jetter,& Chu (1990), Luo (1993, 1994)) extended the method of the general 3D motion of curved or planar surfaces. Known today as either 3D-DIC or more descriptively as StereoDIC, the method uses two or more cameras to view the specimen and record digital images of a common region. Using an entirely different set of imaging equations, known as perspective projection, StereoDIC performs cross-camera subset matching to obtain the true, three-dimensional (3D) position of each point on a general, planar or non-planar object. StereoDIC systems (Sutton et al. (2008), Yasmeen et al. (2016, 2018, 2021)) have been used to obtain surface strains and three-dimensional displacements at a dense set of surface locations on a planar or a curved surface, overcoming the inherent limitations of a 2D-DIC system. The advantages of StereoDIC techniques are (i) simplicity of the experimental setup, (ii) measurements can be obtained for both microscale and macroscale

specimens that have either planar or curved surfaces, (iii) high measurement accuracy for displacements and strains, (iv) applicable for both dynamic loading and high-temperature experiments and (v) effective in the presence of large rotations, large translations, and high strains. Since that time, the DIC techniques have become the most popular measurement method throughout the world. Recent research works in a wide range of physics, aerospace, civil, biomedical, and mechanical engineering applications using Stereo DIC strain measurement techniques include the follows as a partial listing (Sutton et al.(2001,2007), Helm et al., (2003), Yan et al.,(2007), Peth et al. (2010), Helfrick et al. (2011), Chen et al. (2013), Sutradhar et al. (2014), Shao et al. (2016), Dzayeet et al. (2019), Huňady et al. (2019), Zhou et al. (2019), Yasmeen et al. (2021)). Specific details for the StereoDIC measurement technique used in this dissertation are presented in Section 4.2.4 Digital image correlation.

CHAPTER 3

YIELDING, HARDENING, AND PLASTICITY THEORY

3.1 OVERVIEW

This chapter reviews the material constitutive models, yield criteria, and plasticity theory. Since plastic behavior is important in a wide range of applications, strain hardening behavior such as isotropic and kinematic hardening are also reviewed. Since plasticity theory attempts to predict the behavior of metals under permanent deformation, the four major elements include 1) stress-strain relationship describing the uniaxial loading behavior of the material; 2) yield criterion distinguishing between multiaxial elastic and elastic-plastic behavior; 3) flow or deformation rule relating stresses to the corresponding strains or strain increments, and 4) hardening rule describing yield surface evolution during deformation. A brief description of each component is given in this chapter. Both incremental and deformation plasticity are discussed in this chapter.

3.2 STRESS-STRAIN RELATIONSHIP

Strain is a non-dimensional measure describing material deformation that results from applied stress. Stress is defined locally as the increment of force divided by an increment in the material cross-sectional area. Constitutive equations relate stresses to strains at each point so that knowledge of material properties is crucial for accurate elastic-plastic predictions. Typical stress-strain data reveal many of the properties of a material, such as

the elastic modulus, Poisson's ratio, hardening response, plastic modulus, and tangent modulus. Since properties are uniquely obtained from a uniaxial stress-strain experiment, it is important to understand and experimentally obtained stress-strain curves.

3.2.1 Parameters involved in the elastic-plastic analysis

Fig. 3.1 presents a typical uniaxial stress-strain curve. The material property known as Young's modulus or the elastic modulus, E, is the slope of the early proportional part of the stress-strain curve. It is one of the most important properties of solid materials and is defined as

$$E = \frac{\sigma}{\varepsilon} \tag{3-1}$$

This relationship is true when the stresses and strain are within the proportional limit. However, the elastic-plastic part of the stress-strain curve of the material is not linear. A deformation theory or an incremental procedure is often adopted to explain the elastic-plastic part of the stress-strain curve. In this dissertation work, incremental plastic strain theory is considered. In this theory, the incremental total strain is the sum of an elastic part, $d\varepsilon^e$, and a plastic part, $d\varepsilon^p$:

$$d\varepsilon = d\varepsilon^e + d\varepsilon^p \tag{3-2}$$

The infinitesimal stress increment, $d\sigma$, is related to the infinitesimal strain increment, $d\varepsilon$, by

$$d\sigma = E_T d\varepsilon \tag{3-3}$$

where E_T, is the tangent modulus that varies during plastic deformation. The instantaneous slope of the stress-strain curve shown in Fig. 3.1 is the tangent modulus. The tangent

modulus quantifies the "softening" or "hardening" of material that generally occurs when it begins to yield.

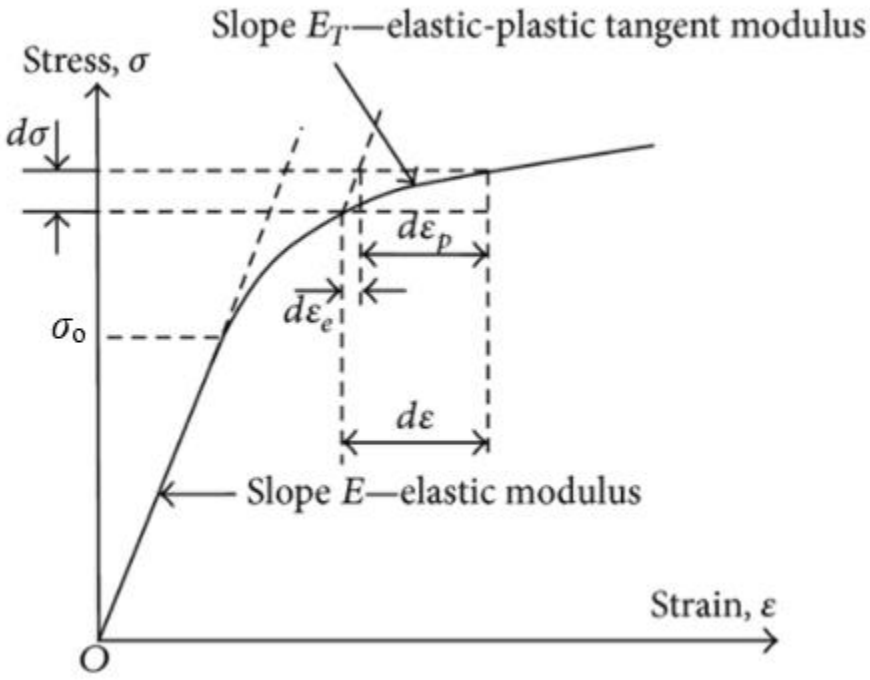

Figure 3.1 Elastic and tangent modulus on stress-strain curves (MC Elliotis, 2013)

Poisson's ratio is another material parameter that describes the expansion or contraction of material in directions perpendicular to the loading direction. These material properties can be determined from a simple uniaxial loading in the elastic range of loading. For an isotropic material, Poisson's ratio is defined as

$$\upsilon = -\frac{\varepsilon_{lateral}}{\varepsilon_{axial}} \tag{3-4}$$

3.2.2 Modeling Plastic Behavior Under Uniaxial loading

The uniaxial stress-strain curve can be idealized in the plastic range. The curve can be used to determine the type of hardening and whether elastic deformations are significant. Fig. 3.2 shows four types of stress-strain curves. An elastic-perfectly plastic material response

model is shown in Fig. 3.2 (a). In this case, the effect of work hardening is neglected and assumes plastic flow occurs when the stress reaches its yield stress, σ_0. Thus, the uniaxial stress-strain relation can be expressed as

$$\varepsilon = \frac{\sigma}{E} \quad for\ \sigma < \sigma_0 \tag{3-5}$$

$$\varepsilon = \frac{\sigma}{E} + \varepsilon^P \quad for\ \sigma > \sigma_0 \tag{3-6}$$

Fig. 3.2(b) presents the elastic-linear hardening model. In the elastic-linear hardening model, the stress-strain curve is approximated by two straight lines. The intersection of the two lines occurs at the yield stress, σ_0, with a corresponding yield strain. The first line represents the elastic region, and this region has a slope equal to the elastic modulus, E. The second line represents the idealized hardening behavior, which has a slope equal to the tangent modulus, E_T. The uniaxial tension stress-strain relations can be expressed as

$$\varepsilon = \frac{\sigma}{E} \quad for\ \sigma < \sigma_0 \tag{3-7}$$

$$\varepsilon = \frac{\sigma_0}{E} + \frac{1}{E_t}\ (\sigma - \sigma_0\ )\ for\ \sigma > \sigma_0 \tag{3-8}$$

Fig. 3.2(c) presents the elastic-power law hardening model. The elastic-power law hardening model is oftentimes used to fit the experimental stress-strain curve since many materials exhibit a non-linear hardening response beyond yielding. The uniaxial tension stress-strain relations can be expressed as

$$\varepsilon = \frac{\sigma}{E} \quad for\ \sigma < \sigma_0 \tag{3-9}$$

$$\varepsilon = (\frac{\sigma}{K})^{\frac{1}{n}};\ \sigma = K(\varepsilon)^n = \sigma_0(\frac{\varepsilon}{\varepsilon_0})^{\frac{1}{N}}\ for\ \sigma > \sigma_0 \tag{3-10}$$

where, k=$\frac{\sigma_0}{(\varepsilon_0)^{\frac{1}{n}}}$ and n=$\frac{1}{N}$ are the two constants, which are considered to be material characteristics when determined through optimal fitting to experimental data.

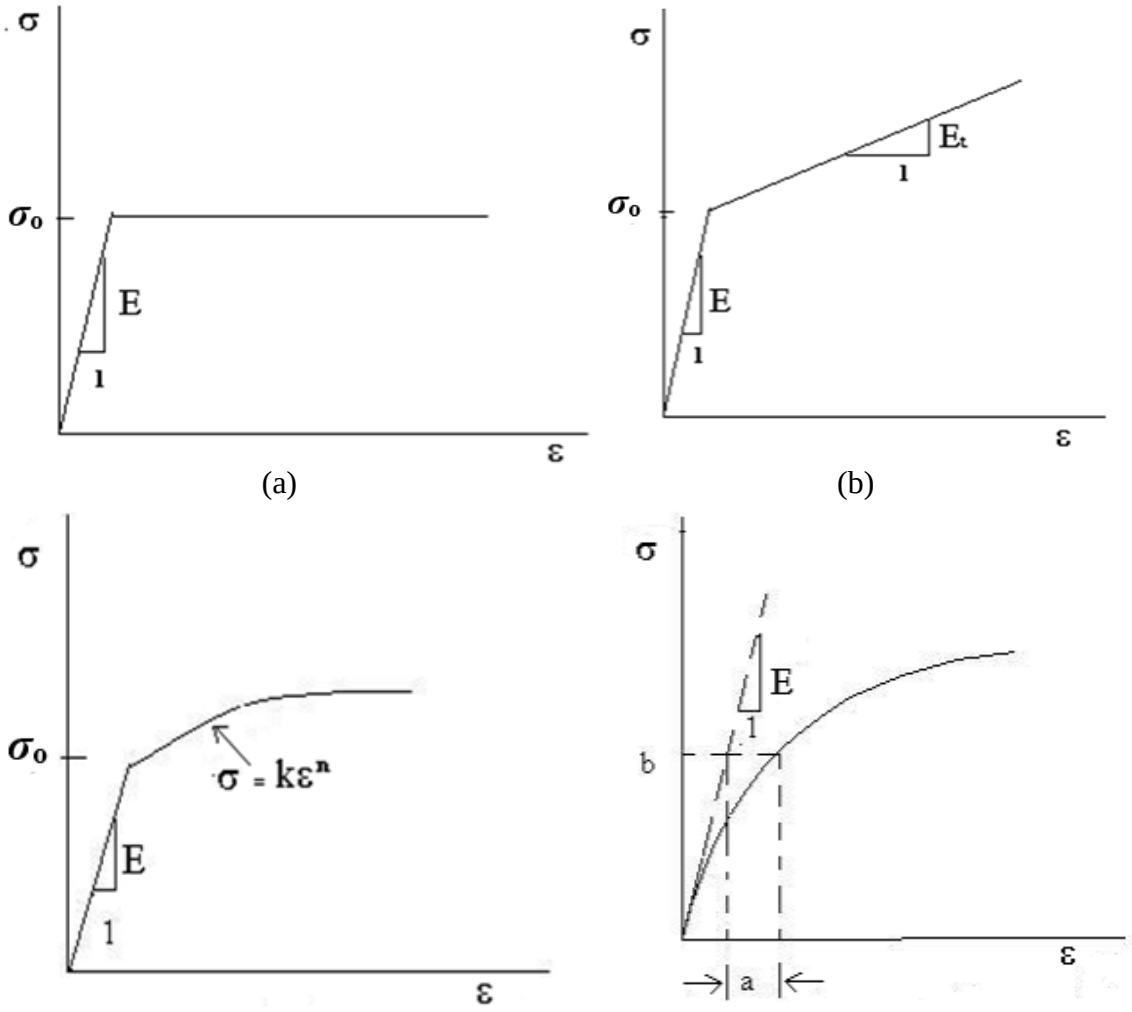

Figure 3.2 Idealized stress-strain curves (a) Elastic-perfectly plastic model, (b) Elastic-linear hardening model, (c) Elastic-power law hardening model, (d) Ramberg-Osgood Model (elsevierhealth.com)

Fig. 3.2(d) presents the Ramberg-Osgood model (1943). This model suggested the following relation for the representation of the nonlinear stress-strain curve

$$\varepsilon = \frac{\sigma}{E} + a(\frac{\sigma}{b})^n \quad (3\text{-}11)$$

where a, b, and n are constants that can be obtained from the experimental stress-strain curve. The initial slope of the curve takes on the value of the elastic modulus E at $\sigma = 0$, with non-linear response occurring for all non-zero stresses. This model uses three fitting parameters and can be used to obtain a better fit of the experimental stress-strain curves.

3.3 YIELD CRITERIA

Yield criteria are generally written in terms of stresses; defining the stress state(s) at a point must satisfy in order for the material to incur permanent macroscopic deformation (i.e. yield). The onset of initial yielding at a point when undergoing uniaxial tension is shown in Fig. 3.2 as occurring at the stress σ_o. However, when a point is subjected to complex, three-dimensional stress states, the combination of stresses that induces yielding is more complex to define, with the work of many of the historically important solid mechanicians (e.g., Tresca, von Mises, Hill, Bell) contributing to the effort. Conceptually, when the stresses at a point are "below" yielding, then the deformations associated with slight increases in stress will result in elastic (i.e. reversible) macroscopic strains. When stresses at a point satisfy the yield criterion, any additional increments in stress will result in additional elastic and plastic deformations. For mixed-mode loading conditions, the stress state at yielding is a function of all components of the stress tensor, σ_{ij} with i = 1, 2, 3 and j = 1, 2, 3 A general form for an initial yield criterion can be expressed as

$$F(\sigma_{ij}, K) = 0 \tag{3-12}$$

where K is the material hardening parameter determined from experimental measurements. Several initial yield conditions have been proposed by a number of researchers presented

in the literature review section. In this section, the common initial isotropic and anisotropic yield criteria are presented.

Table 3.1 lists some of the major phenomenological yield functions proposed to describe the material response, including anisotropic, orthotropic, and isotropic behavior. For the various anisotropic yield functions, the column designated ‘shear’ in Table 3.1 indicates whether shear terms appear in the anisotropic yield function formulation. The column labeled ‘parameters’ indicates the number of unknown coefficients that appear in the yield function and require experimental determination by performing experiments on specimens extracted from different orientations in the material. Table 3.1 is a modified version of the list presented in Barlat et al.(1991). The isotropic yield criteria, e.g., Tresca (1864) criterion, von Mises (1913), and Hosford criterion (1980), are discussed in this section. The anisotropic yield criteria developed by Hill (1948,1979) and Barlat (1991, 2005) are also reviewed in this section.

Table 3.1 Phenomenological yield function

Yield Criterion	Type	Shear	Parameters
Tresca(1864)	Isotropy	-	-
Von Mises(1913)	Isotropy	-	-
Hill(1948)	Anisotropy	Yes	6
Hosford (1972)	Isotropy	-	-
Hill(1979)	Anisotropy	-	3
Barlat(1991)	Anisotropy	Yes	6
Barlat(2003)	Anisotropy	-	8
Barlat(2005)	Anisotropy	-	18

3.3.1 Tresca yield criterion

Tresca's (1864) yield criterion, also known as the maximum shear stress criterion, is the earliest yield criterion. For stresses applied in two dimensions, the Tresca yield criteria form a hexagonal shape, as shown graphically in Fig. 3.3., with yielding in the 1 and 2 directions when the shear stress = $\sigma_o/2$. In three dimensions, the Tresca criterion states that yielding occurs at a critical value of the maximum shear stress, Y, that is present when yield occurs in simple tension. The criterion can be expressed as:

$$Y = |\max(\sigma_1, \sigma_2, \sigma_3) - \min(\sigma_1, \sigma_2, \sigma_3)|/2 = \sigma_0/2 \tag{3-13}$$

where σ_1, σ_2, σ_3 are principal stresses, and σ_0 is the yield stress that can be determined from uniaxial tension experiments.

After the Tresca criterion was developed, researchers have attempted to generalize the approach by defining an “effective stress” to describe yielding, a concept that is especially relevant for hardening materials since the hardening response is obtained from uniaxial data. Instead of using the maximum shear stress, the concept of effective tensile stress was proposed to predict yielding under multiaxial loading conditions that are consistent with results from simple uniaxial tensile tests. Effective stress ($\bar{\sigma}$), and equivalent strain ($\bar{\varepsilon}$) are then related to each other using the hardening parameter obtained from uniaxial experiments. With this modification, a generalized form of the Tresca criterion using effective stress is

$$\bar{\sigma} = |\max(\sigma_1, \sigma_2, \sigma_3) - \min(\sigma_1, \sigma_2, \sigma_3)|/2 \tag{3-14}$$

Equivalent strain will be discussed in the latter part of this chapter,

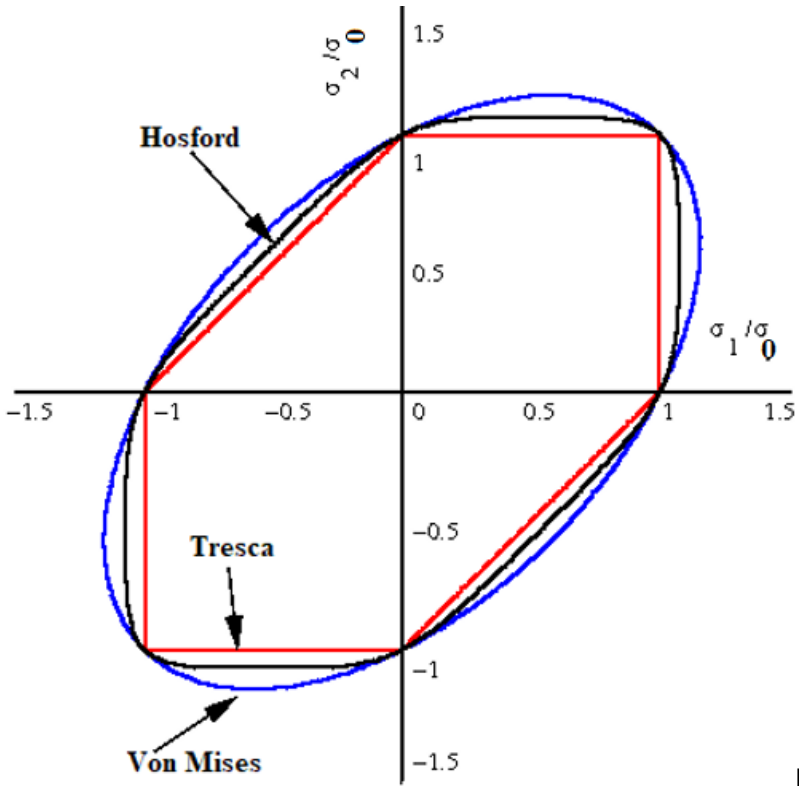

Figure 3.3 Schematic drawing of the yield surfaces of the Tresca, Von Mises, and Hosford yield criteria (wikipedia.org)

3.3.2 Von Mises yield criterion

According to the von Mises (1913) yield criterion, yielding begins when the distortion energy for a mixed-mode stress state is equal to that in a uniaxial tension specimen at yielding. The von Mises yield criteria is an ellipse in principal stress space shown in Fig. 3.3. The von Mises yield condition can be written as

$$Y = \frac{3}{2} S_{ij} S_{ij} - \sigma_0^2 = 0 \tag{3-15}$$

where S_{ij} is the deviatoric stress tensor, σ_0 is the initial yield stress. The deviatoric stress tensor can be expressed in terms of the stress tensor σ_{ij},

$$S_{ij} = \sigma_{ij} - \frac{\sigma_{kk}}{3} \delta_{ij} \tag{3-16}$$

where, δ_{ij} is Kronecker delta and where repeated indices indicate sum over the range (i.e., $\sigma_{kk} = \sigma_{11} + \sigma_{22} + \sigma_{33}$)

The von Mises effective stress can be defined as

$$\bar{\sigma} = \bar{\sigma}_{VM} = \sqrt{\frac{3}{2} S_{ij} S_{ij}} \tag{3-17}$$

The von Mises yield criterion in terms of principal stresses is

$$\sqrt{\frac{1}{2}\{(\sigma_1 - \sigma_2)^2 + (\sigma_1 - \sigma_3)^2 + (\sigma_3 - \sigma_2)^2\}} = \sigma_0 \tag{3-18}$$

where, σ_1, σ_2 and σ_3 are principal stresses and σ_o is the yield stress. Thus, the von Mises equivalent stress. $\bar{\sigma}$, in term of principal stresses is defined by

$$\bar{\sigma} = \bar{\sigma}_{VM} = \sqrt{\frac{1}{2}\{(\sigma_1 - \sigma_2)^2 + (\sigma_1 - \sigma_3)^2 + (\sigma_3 - \sigma_2)^2\}} \tag{3-19}$$

3.3.3 Hosford yield criterion

A generalized form of the Von Mises criteria is proposed by Hosford (1980):

$$Y = |\sigma_1 - \sigma_2|^n + |\sigma_2 - \sigma_3|^n + |\sigma_3 - \sigma_1|^n = 2{\sigma_0}^n \tag{3-20}$$

When $n = 0$ or $n \to \infty$, the Hosford criterion reduces to the Tresca yield criterion. When n = 2, the Hosford criterion reduces to the von Mises yield criterion. For body-centered cubic (BCC) materials, n=6, and for face-centred cubic (FCC) materials n=8. In principle, the values of n correspond to the number of easy slip planes in the material system. The Hosford yield surface lies between the yield surface of Tresca and von Mises, as shown in Fig. 3.3. Like Tresca and von Mises, the Hosford effective stress can be defined as

$$\bar{\sigma} = \sqrt[n]{\frac{1}{2}|\sigma_1 - \sigma_2|^n + |\sigma_2 - \sigma_3|^n + |\sigma_3 - \sigma_1|^n} \tag{3-21}$$

3.3.4 Hill yield criterion

The earliest and simplest version of the Hill yield criterion for an anisotropic material response was a simple extension of the von Mises yield criterion and had a quadratic form. This quadratic Hill's (1948) anisotropic yield function can be expressed as:

$$Y = \mathrm{F}(\sigma_{22} - \sigma_{33})^2 + \mathrm{G}(\sigma_{33} - \sigma_{11})^2 + \mathrm{H}(\sigma_{11} - \sigma_{22})^2 + 2\mathrm{L}\tau_{23}^2 + 2\mathrm{M}\tau_{31}^2 + 2\mathrm{N}\tau_{12}^2 = 2\bar{\sigma}^n \quad (3\text{-}22)$$

The material will yield when $Y \geq 0$ and In Eq. (3-22) F, G, H, L, M, N are constants determined experimentally. The quadratic Hill yield criterion is pressure independent and depends only on the deviatoric stresses, predicting the same yield stress in tension and in compression.

Later, Hill (1979) extended his previously proposed criterion to a generalized yield criterion as the following form

$$Y = F|\sigma_2 - \sigma_2|^m + G|\sigma_3 - \sigma_1|^m + H|\sigma_1 - \sigma_2|^m + \mathrm{L}|2\sigma_1 - \sigma_2 - \sigma_3|^m + \mathrm{M}|2\sigma_2 - \sigma_3 - \sigma_1|^m + \mathrm{N}|2\sigma_3 - \sigma_1 - \sigma_2|^m = 2\bar{\sigma}^m \quad (3\text{-}23)$$

where σ_1, σ_2 and σ_3 are principal stresses, F, G, H, L, M, N are the anisotropic parameters, and m is a material-constant that is > 1 and anisotropy dependent.

3.3.5 Barlat Yield Criterion

Barlat et al. (1991) have developed several anisotropic yield function models for anisotropic plasticity in materials. This section covers some of the relevant Barlat et al. yield functions as there are too many to list here. Barlat six parameter yield function Yld91 is one of the popular yield functions among researchers since it only requires six parameters

for predictions. For an anisotropic material, the effective stress, $\bar{\sigma}$ = $\bar{\sigma}_B$, defined by Barlat et al. (1991), is employed in these studies. Here the yield function, Y, is given in terms of $\bar{\sigma}$ as follows

$$Y = |S_1 - S_2|^m + |S_2 - S_3|^m + |S_3 - S_1|^m = 2\bar{\sigma}^m \tag{3-24}$$

with m being an integer and m = 8 for FCC materials such as aluminum alloys. Here Y can be expressed in terms of stress invariants J_2 and J_3 as follows

$$Y = (3J_2)^{\frac{m}{2}}\left\{\left[2\cos\left(\frac{2\theta+\pi}{6}\right)\right]^m + \left[2\cos\left(\frac{2\theta-3\pi}{6}\right)\right]^m + \left[-2\cos\left(\frac{2\theta+5\pi}{6}\right)\right]^m\right\} = 2\bar{\sigma}^m = 2\bar{\sigma_B}^m \tag{3-25}$$

where the parameter $\theta = cos^{-1}\left(\frac{J_3}{J_2^{\frac{3}{2}}}\right)$ J_2 and $J_3$the second and third invariant of the deviatoric stress tensor S_{ij}. In the anisotropic yield function S_{ij}, J_2 and J_3 are defined by

$$[S] = \begin{bmatrix} S_x & S_{xy} & S_{zx} \\ S_{xy} & S_y & S_{yz} \\ S_{zx} & S_{yz} & S_z \end{bmatrix} = \begin{bmatrix} \frac{C-B}{3} & H & G \\ H & \frac{A-C}{3} & F \\ G & F & \frac{B-A}{3} \end{bmatrix}$$

$$[S] = \begin{bmatrix} \frac{cC-bB}{3} & hH & gG \\ hH & \frac{aA-cC}{3} & fF \\ gG & fF & \frac{bB-aA}{3} \end{bmatrix}$$

$$J_2 = \frac{(fF)^2 + (gG)^2 + (hH)^2}{3} + \frac{(aA-cC)^2 + (cC-bB)^2 + (bB-aA)^2}{54}$$

$$J_3 = \frac{(cC - bB)(aA - cC)(bB - aA)}{54} + fghFGH$$
$$- \frac{(cC - bB)(fF)^2 + (aA - cC)(gG)^2 + (bB - aA)(hH)^2}{6}$$

In these equations, $A = \sigma_y - \sigma_z,\ B = \sigma_z - \sigma_x,\ C = \sigma_x - \sigma_y,\ F = \sigma_{yz},\ G = \sigma_{zx},\ H = \sigma_{xy}$ The variables a, b, c, f, g, and h are material-specific anisotropic yield function parameters. For an isotropic material, all six parameters are equal to 1. The parameter, θ, in Eq. 3-25 is unrelated to rotations associated with coordinate transformations in either plane stress or plane strain.

Barlat et al. 2005 suggested a new material model Yld2004- 18p, which describes the anisotropic behavior of metals in a full three-dimensional stress state:

$$Y = \sum_{i=1}^{3}\sum_{j=1}^{3}\left|\tilde{S}_i' - \tilde{S}_j''\right|^a = \left|\tilde{S}_1' - \tilde{S}_1''\right|^a + \left|\tilde{S}_1' - \tilde{S}_2''\right|^a + \left|\tilde{S}_1' - \tilde{S}_3''\right|^a + \left|\tilde{S}_2' - \tilde{S}_1''\right|^a + \left|\tilde{S}_2' - \tilde{S}_2''\right|^a + \left|\tilde{S}_2' - \tilde{S}_3''\right|^a + \left|\tilde{S}_3' - \tilde{S}_1''\right|^a + \left|\tilde{S}_3' - \tilde{S}_2''\right|^a + \left|\tilde{S}_3' - \tilde{S}_3''\right|^a = 4\bar{\sigma}^a \quad (3\text{-}26)$$

with a = 6 and a = 8 for BCC and FCC materials, respectively

where $\tilde{S}_i'$ and $\tilde{S}_j''$ are the eigenvalues of the transformed stress tensors $\tilde{\boldsymbol{s}}'$ and $\tilde{\boldsymbol{s}}''$ respectively. The model introduces anisotropy through two linear transformations to construct the tensors $\tilde{\boldsymbol{s}}'$ and $\tilde{\boldsymbol{s}}''$ from the Cauchy stress tensor σ. The transformed stresses are functions of the deviatoric stress tensors.

$$\boldsymbol{s} = \boldsymbol{\sigma} - \frac{1}{3}tr(\boldsymbol{\sigma})\mathbf{1} \quad (3\text{-}27)$$

These transformed stresses are commonly derived in vector format from a transformation through the matrices $\boldsymbol{C}'$, and $\boldsymbol{C}''$

$$\tilde{\boldsymbol{s}}' = \boldsymbol{C}'\boldsymbol{s}, \text{ and } \tilde{\boldsymbol{s}}'' = \boldsymbol{C}''\boldsymbol{s} \quad (3\text{-}28)$$

fully expressed by:

$$\begin{Bmatrix} \tilde{s}'_{xx} \\ \tilde{s}'_{yy} \\ \tilde{s}'_{zz} \\ \tilde{s}'_{yz} \\ \tilde{s}'_{zx} \\ \tilde{s}'_{xy} \end{Bmatrix} = \begin{bmatrix} 0 & -c'_{12} & -c'_{13} & 0 & 0 & 0 \\ -c'_{21} & 0 & -c'_{23} & 0 & 0 & 0 \\ -c'_{31} & -c'_{32} & 0 & 0 & 0 & 0 \\ 0 & 0 & 0 & c'_{44} & 0 & 0 \\ 0 & 0 & 0 & 0 & c'_{55} & 0 \\ 0 & 0 & 0 & 0 & 0 & c'_{66} \end{bmatrix} \begin{Bmatrix} s_{xx} \\ s_{yy} \\ s_{zz} \\ s_{yz} \\ s_{zx} \\ s_{xy} \end{Bmatrix} \quad \text{and}$$

$$\begin{Bmatrix} \tilde{s}''_{xx} \\ \tilde{s}''_{yy} \\ \tilde{s}''_{zz} \\ \tilde{s}''_{yz} \\ \tilde{s}''_{zx} \\ \tilde{s}''_{xy} \end{Bmatrix} = \begin{bmatrix} 0 & -c''_{12} & -c''_{13} & 0 & 0 & 0 \\ -c''_{21} & 0 & -c''_{23} & 0 & 0 & 0 \\ -c''_{31} & -c''_{32} & 0 & 0 & 0 & 0 \\ 0 & 0 & 0 & c''_{44} & 0 & 0 \\ 0 & 0 & 0 & 0 & c''_{55} & 0 \\ 0 & 0 & 0 & 0 & 0 & c''_{66} \end{bmatrix} \begin{Bmatrix} s_{xx} \\ s_{yy} \\ s_{zz} \\ s_{yz} \\ s_{zx} \\ s_{xy} \end{Bmatrix}$$

The matrices $\boldsymbol{C}'$, and $\boldsymbol{C}''$ are not necessarily symmetric and contain in total 18 parameters to describe the anisotropy of the yield function. More information regarding the calibration of this yield function can be found in the previous study by the authors (Barlat et al. 2005 and van den et al. 2016). As a brief illustration, Yld2004- 18p can be used when there is extensive experimental data available from specimens obtained along different orientations from the original sample. For example, uniaxial tension data for 0°, 15°, 30°, 45°, 60°, 75° and 90° from the rolling direction and simple torsion data for four additional out-of-plane stress components. Such experiments are challenging to complete, making the approach less attractive to investigators. Additional anisotropic Barlat yield functions can be found from the following literature (Barlat and Lian, 1989; Barlat et al., 1997a,1997b, 2003,2005).

3.4 ELASTIC AND PLASTIC DEFORMATION

As discussed in the previous section, the stress-strain state in a material due to applied loading can be either elastic or elastic-plastic, depending upon the magnitudes of the applied loads. In the elastic, reversible deformation case, the body returns to its original shape upon load removal. If the load is sufficiently high, plastic deformations will occur, causing the body to undergo irreversible deformations when the load is removed. In this section, the theory of elastic and plastic deformations is presented. The first part discussed the linear elastic response of the material during elastic and plastic deformation. The second part presents theories that describe the plastic response of the material under plastic deformation. In a literature survey including (Hencky, 1924, Ilyushin, 1947,1963, Levy, 1871 and von Mises,1913, Prandtl, 1924, Reuss, 1930), two theories associated with plastic deformation are discussed; the deformation theory of plasticity relating total plastic strains to the stresses, and incremental or flow theory of plasticity relating plastic strain increments to stresses.

3.4.1 Elastic deformation

The relationship between stress and strain in the elastic range is generally linear and reversible until the yield point. The generalized Hooke's law describes the linear elastic relationship for isotropic materials and can be expressed as

$$\varepsilon_{ij}^{e} = \frac{1}{E}(\sigma_{ij} - \upsilon(\sigma_{kk}\delta_{ij} - \sigma_{ij})) \tag{3-29}$$

where E and v are Young's modulus and Poisson's ratio discussed in section 3.2. respectively. These relationships apply to both elastic and plastic deformation cases, with

E and ν are determined during the elastic loading process. Superscript “e” in Eq. (3-29). indicates elastic strains. For elastic deformation, the total strain is equal to the elastic strain. On the other hand, to obtain the total strain when both elastic and plastic strains occur, the plastic strains must be added to the elastic strain.

$$\varepsilon_{ij} = \varepsilon_{ij}^{e} + \varepsilon_{ij}^{p} \tag{3-30}$$

3.4.2 Deformation plasticity

The earliest theory of plasticity, also known as the deformation theory of plasticity, was proposed by Hencky(1924) and Ilyushin (1947,1963)in which total plastic strain is a function of total stresses. The deformation theory of plasticity theory is applicable in problems of proportional or simple loading, in which all stress components increase proportionally, or nearly so, without elastic unloading ever occurring (Budiansky, 1959; Kachanov, 1971). The plastic stress-strain relationship suggested by Hencky, assuming small strains, can be written as

$$\varepsilon_{ij}^{p} = \Phi S_{ij} \tag{3-31}$$

where Φ is a scalar-valued function that can be determined from the experiment. For hardening materials, Φ depends on the effective stress (e.g., von Mises equivalent stress, $\bar{\sigma}$, and an equivalent total plastic strain, $\bar{\varepsilon}^{p}$). The equivalent plastic strain can be expressed as

$$\bar{\varepsilon}^{p} = \sqrt{\frac{2}{3}\varepsilon_{ij}^{p}\varepsilon_{ij}^{p}} \tag{3-32}$$

The effective stress-equivalent plastic strain curve in the uniaxial case is considered to be the same as the equivalent stress-equivalent plastic strain for complex states of stress.

3.4.3 Incremental theory of plasticity

In the classical theory of plasticity, Levy (1871) and von Mises (1913) separately suggested total incremental strain relates the current state of stress. Later, Prandtl (1924) for plane strain and Reuss (1930) proposed equations for an arbitrary stress state that are used as specific forms in the plastic constitutive equation or flow rule of Hill (Hill, 1950). To obtain the incremental total strain during elastic-plastic loading, incremental plastic strains must be added to the incremental elastic strains by rewriting Eq. (3-2)

$$d\varepsilon_{ij} = d\varepsilon_{ij}^{e} + d\varepsilon_{ij}^{p}$$

The elastic strain increment in Eq. (3-2) can be determined from Hooke's law

$$d\varepsilon_{ij}^{e} = \frac{1}{E}\{(1+\upsilon)d\sigma_{ij} - \upsilon d\sigma_{kk}\delta_{ij}\} \tag{3-33}$$

The plastic part of Eq. (3-2) can determine using the flow rule:

$$d\varepsilon_{ij}^{p} = d\lambda \frac{\delta Y}{\delta \sigma_{ij}} \tag{3-34}$$

where Y is a yield function, and $d\lambda$ is a scalar called the plastic multiplier.

This form of the flow rule is called an associated flow rule, and the assumption of co-directionality is called the normality condition of plastic flow and the normal to the yield function. More detailed studies regarding associated and non-associated flow theory can be found in the references (Bland,1957, Maier & Hueckel, 1979, and Lademo et al., 1999).

For plastic deformation, increments in plastic work/dissipation in terms of increments in equivalent plastic strain are employed to define effective stress and thus connect general multiaxial states to uniaxial experimental results in the following way;

$$dW^P = \bar{\sigma}.d\bar{\varepsilon}^p = \sigma_{ij}.d\varepsilon_{ij}^p \quad (3\text{-}35)$$

In the plastic strain range for an elastic-plastic material, increments of elastic strain components $d\varepsilon_x^e$, $d\varepsilon_y^e$, $d\varepsilon_z^e$ and the plastic strain increments $d\varepsilon_x^p$, $d\varepsilon_y^p$, $d\varepsilon_z^p$ should be handled separately. As note earlier, Prandtl treated this problem for plane-strain and Reuss (Budapest Technical University) showed the expression for all strain components. For example,

$$d\varepsilon_{xx} = d\varepsilon_{xx}^e + d\varepsilon_{xx}^p = \frac{1}{E}\{d\sigma_{xx} - \upsilon(d\sigma_{yy} + d\sigma_{zz})\} + \frac{1}{3}d\lambda\{2\sigma_{xx} - (\sigma_{yy} + \sigma_{zz})\}$$

$$d\varepsilon_{yy} = d\varepsilon_{yy}^e + d\varepsilon_{yy}^p = \frac{1}{E}\{d\sigma_{yy} - \upsilon(d\sigma_{xx} + d\sigma_{zz})\} + \frac{1}{3}d\lambda\{2\sigma_{yy} - (\sigma_{xx} + \sigma_{zz})\}$$

$$d\varepsilon_{zz} = d\varepsilon_{zz}^e + d\varepsilon_{zz}^p = \frac{1}{E}\{d\sigma_{zz} - \upsilon(d\sigma_{xx} + d\sigma_{yy})\} + \frac{1}{3}d\lambda\{2\sigma_{zz} - (\sigma_{xx} + \sigma_{yy})\} \quad (3\text{-}36)$$

$$d\varepsilon_{xy} = d\varepsilon_{xy}^e + d\varepsilon_{xy}^p = \frac{1}{E}(1+\upsilon)d\sigma_{xy} + d\lambda\sigma_{xy}$$

$$d\varepsilon_{yz} = d\varepsilon_{yz}^e + d\varepsilon_{yz}^p = \frac{1}{E}(1+\upsilon)d\sigma_{yz} + d\lambda\sigma_{yz}$$

$$d\varepsilon_{zx} = d\varepsilon_{zx}^e + d\varepsilon_{zx}^p = \frac{1}{E}(1+\upsilon)d\sigma_{zx} + d\lambda\sigma_{zx}$$

3.5 HARDENING RULE-MIXED MODE LOADING

Effective stress, $\bar{\sigma}$ and equivalent plastic strain, $\bar{\varepsilon}^p$ can be used to model plastic deformation and hardening in a multimodal stress state case. According to effective stress, $\bar{\sigma}$ and equivalent plastic strain, $\bar{\varepsilon}^p$ concept the effective stress- equivalent plastic strain data should follow the same universal plastic stress-strain response as measured in the uniaxial case. (Kelly, P., 2013). Hardening rules describe how the yielding condition changes during

plastic deformation as a function of loading. For unloading situations, hardening rules also describe the onset of reversed yielding. In the uniaxial test case, a specimen will deform up to yield and then generally undergo hardening, as shown Fig. 3.4; perfectly plastic response is also shown in Fig 3.4. The perfectly plastic case occurs when stresses reach the yield point (A), and plastic deformation is maintained as long as the stress is σ_y. If the stress is decreased, elastic unloading occurs. In the hardening case, once the material reaches its yield point, the stress needs to be continuously increased in order to continue plastic deformation. If the stress is held constant, for example, at B, no further plastic deformation will occur; at the same time, no elastic unloading will occur. This condition cannot be possible in the perfectly plastic case, where there is plastic deformation or elastic unloading. There are two widely used hardening rules: 1) isotropic hardening and 2) kinematic hardening. The simplest case, which corresponds to the expansion of the yield surface, is called isotropic hardening. Pure translation of the yield surface is called kinematic hardening. The combined case of expansion and translation is called mixed hardening. It is important to utilize an appropriate hardening rule for complex mixed-mode loading. Fig. 3.4 shows an experimentally obtained stress-strain curve with typical hardening behavior.

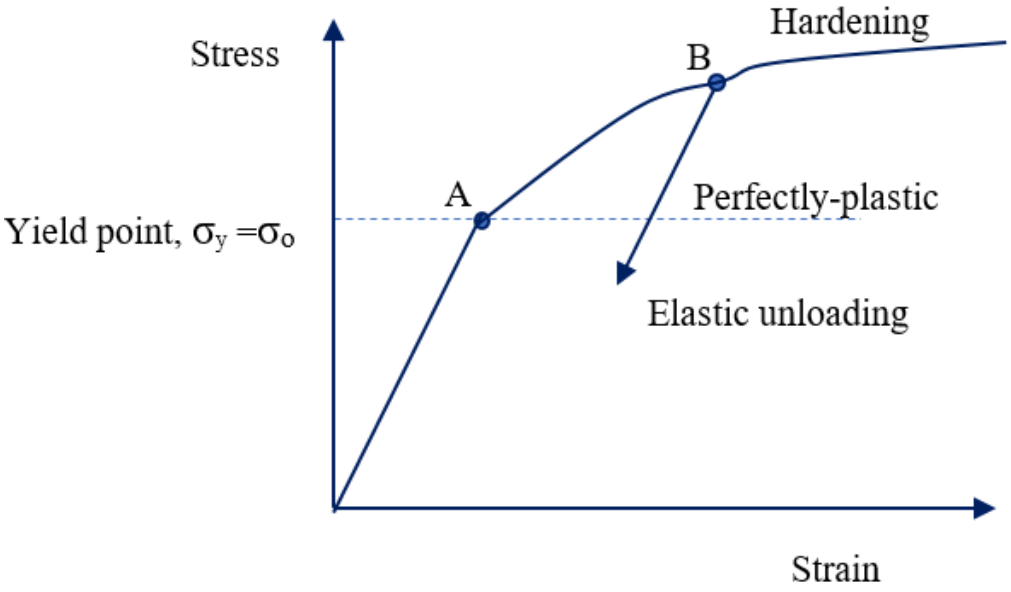

Figure 3.4 A phenomenological uniaxial stress-strain curve showing typical hardening plastic behavior of materials in uniaxial tension

The equation for yielding is written;

$$F(\sigma_{ij}, K^{\alpha}) = 0 \tag{3-37}$$

with the hardening parameters K^{α}, α = 1,2,..., characterizing how the current yield surface changes its size, shape, and position with plastic loading. Initially and during elastic loading, the hardening parameters, $K^{\alpha} = 0$, i.e., it follows that

$$F(\sigma_{ij}, 0) = 0 \tag{3-38}$$

Eq. (3-37) describes how the yield surface's size, shape, and position changes through the hardening parameters and how this occurrence is given by a hardening rule; i.e., hardening rules are isotropic, kinematic, and mixed hardening. This will be further described in the following section.

3.5.1 Isotropic Hardening

The isotropic hardening rule was proposed by Hill (Hill, 1950), where the yield surface grows with a fixed center during plastic deformation, effectively changing the yield stress as the material becomes elastic-plastic. The subsequent yield criteria is an expanded version of the initial one with the same shape and position, as shown in Fig. 3.5.

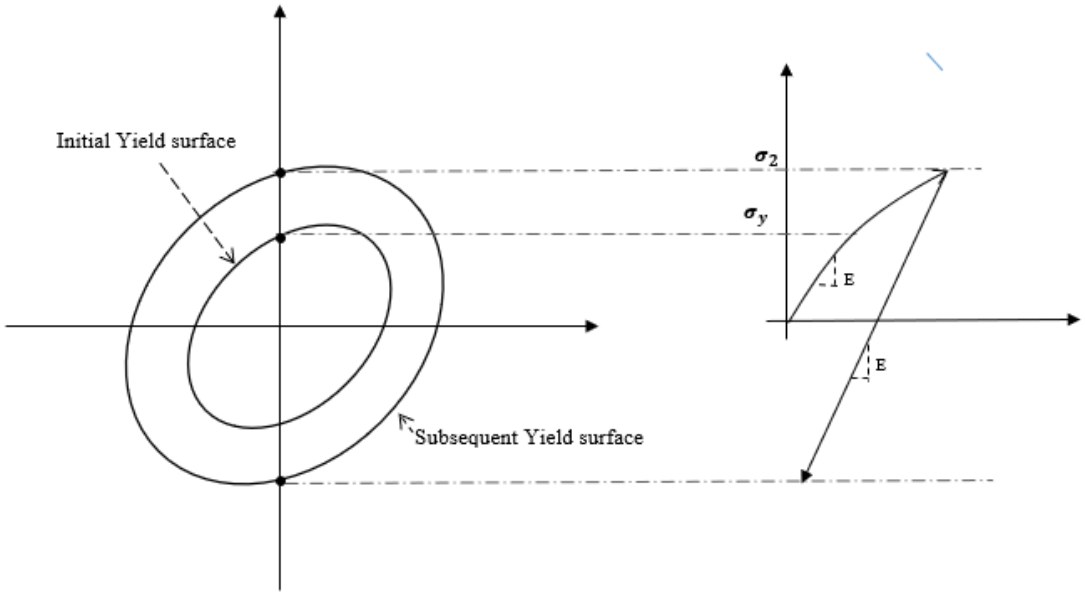

Figure 3.5 Schematic representation of initial and subsequent yield surface according to isotropic hardening. on the deviatoric plane and in tension-compression test conditions

In some cases, it is observed that the behavior of metal specimens in tension and compression is similar so that the current yield stresses in tension and compression are the same. However, in some other metals, as the material is deformed in tension, the yield stress in tension is increased while that in compression is decreased (Fig. 3.6). Metals, where this is true, are exhibiting the Bauchinger effect. In most cases, metals exhibiting this effect tend to maintain essentially isotropic plastic behavior. However, in other cases, the effect can introduce apparent anisotropic plastic behavior. For example, in some

materials that are initially loaded beyond the initial yield in a specific direction, when incurring subsequent loading in that direction, the material would exhibit higher yield stress relative to subsequent loading in other directions.

Based upon the preponderance of usage in the existing literature, in this work, the author used isotropic hardening to describe the change which occurs in the equivalent stress, defining the size of the yield surface as a function of accumulated plastic strain. The main advantage of the isotropic hardening rule is that it is very simple to use. There is only one scalar internal variable and for isotropic hardening, the loading surface can be written as

$$F\left(\sigma_{ij}, K^{\alpha}\right) = F\left(\sigma_{ij}\right) - K = 0 \tag{3-39}$$

where K is the isotropic hardening parameter. K is typically equivalent to the yield strength that increases with effective plastic strain $\bar{\varepsilon}^{p}$ determined from a uniaxial tension experiment. Eq. (3-39) represents the radius of the yield surface. During plastic deformation, the yield surface expands in stress space when material hardening occurs.

As mentioned earlier, effective stress and equivalent plastic strain can be used to define hardening in mixed mode loading and uniaxial loading. There are different representations of isotropic hardening function available in the literature (Ludwik, 1909), Hollomon, 1945, Voce, 1948, Swift, 1952, and Ludwigson, 1971) Later, different researchers (Kleemola and Nieminen, 1974)) validated the hardening function that provides the best fit the experimental stress-strain curves of different materials. The most common hardening functions are presented in Table 3.2.

Table 3.2 Isotropic Hardening Functions

Isotropic Hardening	Function
Holloman(1944)	$\overline{\sigma}(\bar{\varepsilon}^p) = K(\bar{\varepsilon}^p)^n$
Ludick(1909)	$\overline{\sigma}(\bar{\varepsilon}^p) = \sigma_0 + K(\bar{\varepsilon}^p)^n$
Swift(1947)	$\overline{\sigma}(\bar{\varepsilon}^p) = K(\varepsilon_0 + \bar{\varepsilon}^p)^n$
Voce(1948)	$\overline{\sigma}(\bar{\varepsilon}^p) = \sigma_0 + K(1 - e^{-b\bar{\varepsilon}^p})^n$
Prager(1938)	$\overline{\sigma}(\bar{\varepsilon}^p) = \sigma_0 \tanh\left(\frac{E\bar{\varepsilon}^p}{\sigma_0}\right)$

3.5.2 Kinematic hardening

There is one major drawback when using the isotropic hardening rule. Non-monotonic loadings, including stress reversals and phenomena such as the Bauschinger effect, i.e., reduced strength in subsequent loadings opposite the initial, Bauschinger (1881), cannot be predicted. The kinematic hardening rule proposed by Prager (Prager, 1956) and later modified by Ziegler (Ziegler, 1959) was developed to predict non-monotonic behavior. In the kinematic hardening rule, the initial yield criterion is allowed to translate, i.e., change position, but not the size or shape, as illustrated in Fig. 3.6.

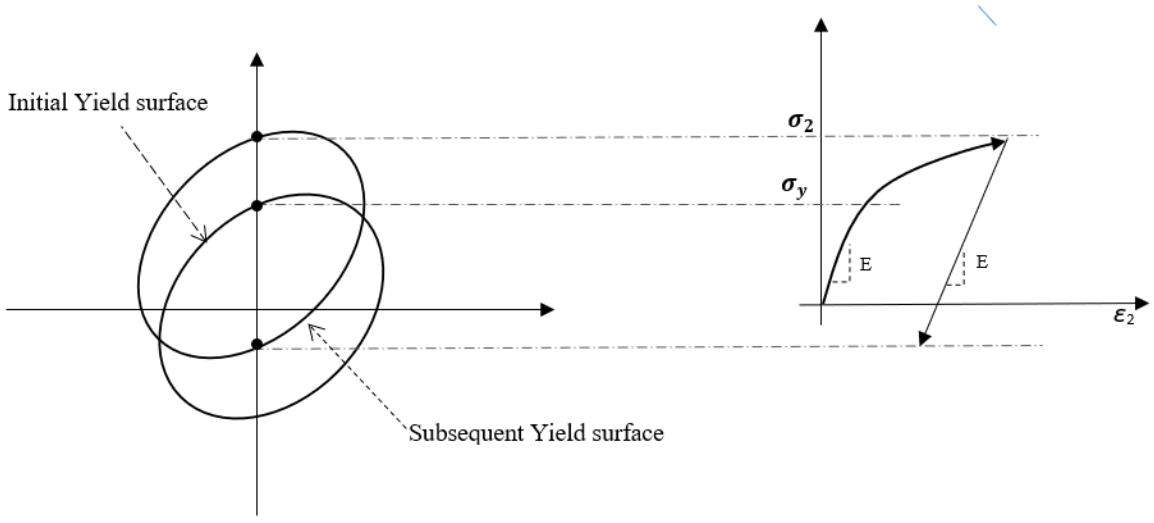

Figure 3.6 Schematic representation of initial and subsequent yield surface according to kinematic hardening on the deviatoric plane and in tension-compression test conditions

For kinematic hardening, Eq. (3-39) can be rewritten as

$$F(\sigma_{ij}, K^{\alpha}) = F(\sigma_{ij} - \alpha_{ij}) = 0 \tag{3-40}$$

where, α_{ij} is called the back-stress tensor describing the current position of the center of the yield surface. Prager (Prager, 1956) assumed that translation of the yield surface depended linearly on the plastic strain increment according to

$$d\alpha_{ij} = c.d\varepsilon_{ij}^{p} \tag{3-41}$$

where *c* is a constant characterizing the material response. With an associated flow, the translation becomes parallel to the normal to the yield surface at the stress point.

Ziegler (Ziegler, 1959), on the other hand, proposed the translation to be parallel to the reduced stress tensor, which can be written as

$$d\alpha_{ij} = d\mu(\sigma_{ij} - \alpha_{ij}) \tag{3-42}$$

where $d\mu$ is a positive scalar that depends on material and strain history. The main disadvantage of Eq. (3-42)is that if a stress space is considered that is not in the full 9-dimensional stress space, it is not consistent.

3.5.3 Mixed hardening rule

The mixed hardening rule is, as the name indicates, a mixture between the isotropic and the kinematic hardening rule. The concept was introduced by Hodge (Hodge, 1957), with the goal of fixing yield surface shape while allowing the size and position of the surface to change with plastic loading. The concept is shown graphically in Fig. 3.7.

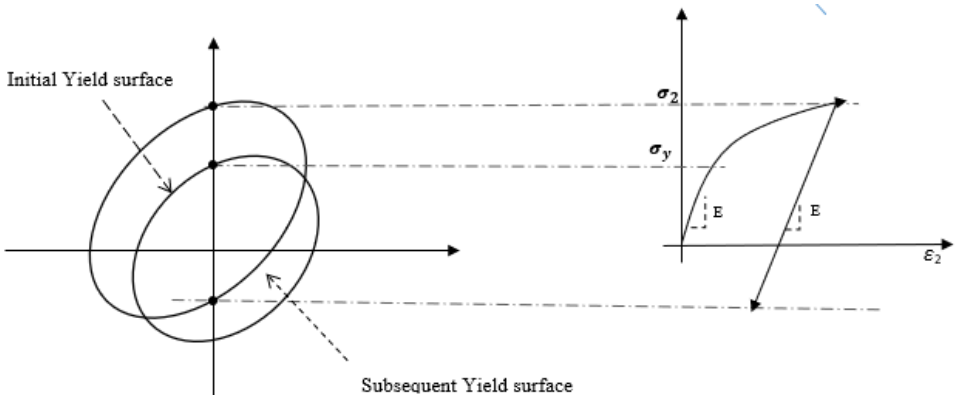

Figure 3.7 Schematic representation of Initial and subsequent yield surface according to mixed hardening on the deviatoric plane and in tension-compression test conditions

Eq. (3-39) can be rewritten as

$$F(\sigma_{ij}, K^{\alpha}) = F(\sigma_{ij} - \alpha_{ij}) - K = 0 \tag{3-43}$$

when considering mixed hardening. The hardening parameters, K^{α}, consists of both the back-stress tensor, α_{ij} , and the hardening parameter, K.

CHAPTER 4

EQUIPMENT, MATERIALS, AND EXPERIMENTAL SETUP

4.1 SPECIMEN AND EXPERIMENTAL CONSIDERATION

The extruded rod material used in this research was obtained from McMaster-Carr (https://www.mcmaster.com/). Three 1.83 m long extruded rods, designated as "original bar', with nominal outer diameter d_o = 28.575mm, were acquired. Two of them (Al6061-T6 MT1) were from the same batch, and the other one (Al6061-T6 MT2) were from a different batch. The reported mechanical properties and nominal chemical composition for nominally similar specimens MT1 and MT2 bars are shown in Table 4.1. To improve our understanding of the large differences in ultimate and yield stresses shown in Table 4.1, Fig. 4.1 shows the microstructure of a longitudinal-radial plane for both the MT1 and MT2 specimens, which are nominally from bars undergoing the same extrusion process. High magnification optical images of the grains and microstructure present in the middle of the MT1 and MT2 specimens were acquired using a Keyence VH-Z500R microscope. In Fig. 4.1, the x-axis represents the radial direction in the bar, and the y-axis represents the longitudinal direction in the bar. A series of metallurgical preparatory steps were required to obtain these images, including sectioning, mounting, grinding, polishing, and etching to prepare specimens for imaging. Grinding, polishing, and etching was performed using standard metallographic procedures.

Several tubular and dog bone specimens are extracted at different orientations of the original bar stock for both MT1 and MT2 materials to perform the required experiments. The specimens and orientations are shown in Fig. 4.2. As shown in Fig 4.2, longitudinal tubular specimens are designated the LDT specimens and were extracted from the central portion of the bars with the longitudinal direction (arbitrarily Y-axes) of the specimen oriented along the length of the bar (Y-axis in Fig. 4.2). The flat dog-bone specimens are extracted from the original bars oriented along with radial directions at circumferential angles, $\phi = 0^0$, $-45^{0,}$ and 90^0 with respect to an arbitrarily selected X-axis direction in the Z-X plane (see Fig. 4.2). These specimens are designated as radial direction dog bone (RDD) specimens and are denoted by RDD0, RDD45, and RDD90, respectively. RDD specimens have a length of 10 mm. In addition to the radial specimens, another set of flat dog-bone specimens oriented along the length of the specimen (Y-axis in Fig. 4.2) are extracted. These are designated as Longitudinal Direction Dogbone (LDD) specimens. Details regarding sample fabrication procedures are presented in Sections 4.1.2 and 4.1.3.

The specimens described above are manufactured for three different purposes. One purpose is to conduct experiments for the determination of all six of the Barlat Yld91 anisotropic yield function parameters for material MT1 and separately for material MT2. For this purpose, two different shaped dog-bone samples (three radially oriented and one longitudinally oriented) and a thin-walled tubular sample are extracted from the original Al-6061T6 MT1 and MT2 bars for calibration of the model. The second purpose was to conduct experiments for MT1 materials under uniaxial tension, combined proportional torsion tension, and simple torsion loading for comparison to model predictions. For that, thin-walled tubular samples were extracted from the original Al-6061T6 MT1 bar. The

third purpose was to use the last set of thin-walled tubular samples manufactured from the original Al-6061T6 MT1 and MT2 bar and conduct simple torsion experiments to compare experimental measurements to predictions using the incremental theory of plasticity model developed with both the isotropic and anisotropic yield functions.

Table 4.1 Mechanical properties and chemical composition of Al6061-T6 given by the manufacturer

Rod stock	Alloy		6061-T6 MT1	6061-T6 MT2
	Dia (mm)		28.575	28.575
Mechanical Properties	Ultimate strength (MPa)	Min	317.2	341.3
		Max	327.5	375.8
	Yield strength (MPa)	Min	286.1	319.3
		Max	299.4	355.8
	Elongation (%)	Min	16.5	15.8
		Max	18	19.5
Chemical composition	Si		0.71	0.76
	Fe		0.28	0.37
	Cu		0.33	0.33
	Mn		0.05	0.11
	Mg		0.89	0.90
	Cr		0.05	0.11
	Zn		0.02	0.06
	Ti		0.02	0.03

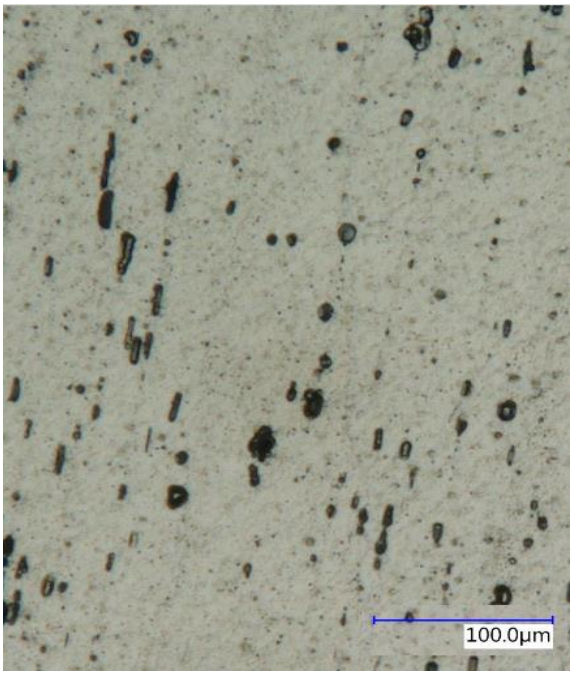

(a)

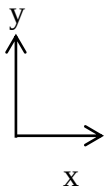

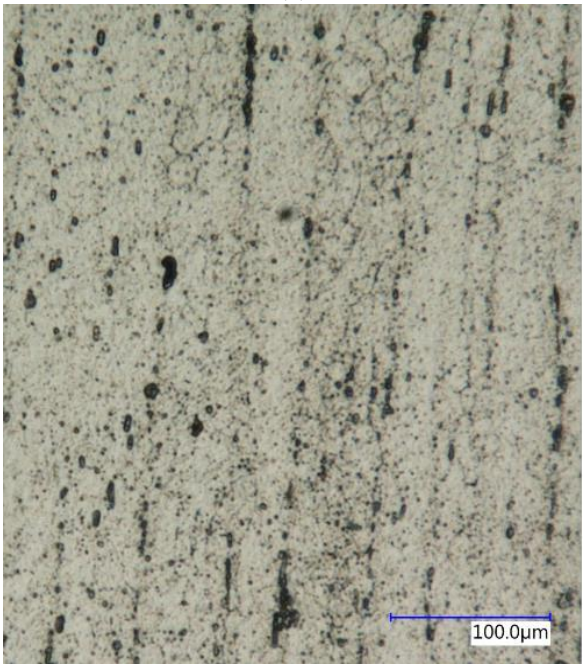

(b)

Figure 4.1 Microstructure of (a) Al6061-T6 MT1, and (b) Al6061-T6 MT2 longitudinally extruded tubular specimens. Images obtained at 1000X using Keyence microscope. The axes x and y represent the radial and longitudinal directions, respectively

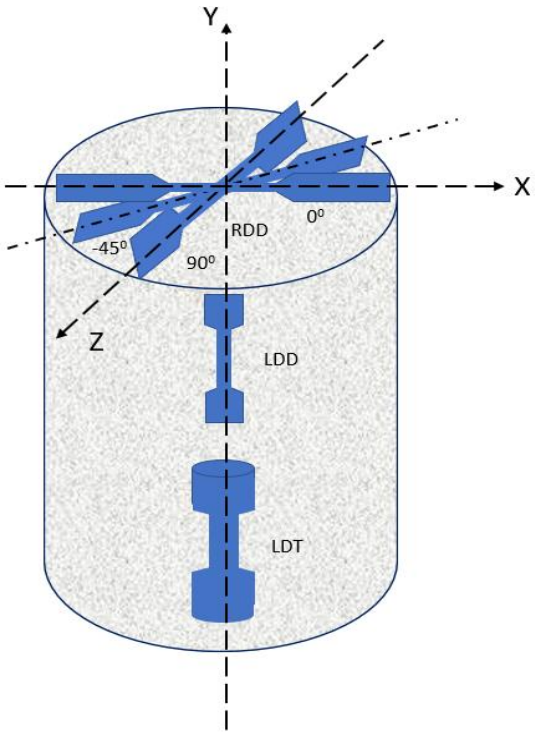

Figure 4.2 Tension, torsion, and combined torsion tension specimens fabricated from 28.575mm dia 6061-T6 MT1 and MT2 aluminum bar. X and Y are orthogonal radial directions selected arbitrarily, and Z is along the length of the cylindrical extruded bar stock.

4.1.1 Local to global coordinate transformation details

Since loading is applied along the longitudinal axis of the specimens, which does not always correspond to global axes, a local specimen coordinate system *x*-*y*-*z* (with *x* along the tensile loading axis) is defined. Fig. 4.3 shows the orientation of the local specimen coordinate system *x*-*y*-*z* for all five specimen geometries and orientations. In this work, the local coordinate system (*x,y,z)* for all four dog bone specimens is shown in Fig. 4.3. The *x*-direction is along each specimen's longitudinal axis, the *y*-direction is in the plane of the specimen surface, and *z* is orthogonal to the planar specimen's surface. For the LDT specimens shown in Fig. 4.2, the longitudinal direction of the tubular specimens is denoted by *x*, with *y* and *z* corresponding to arbitrary, orthogonal radial directions.

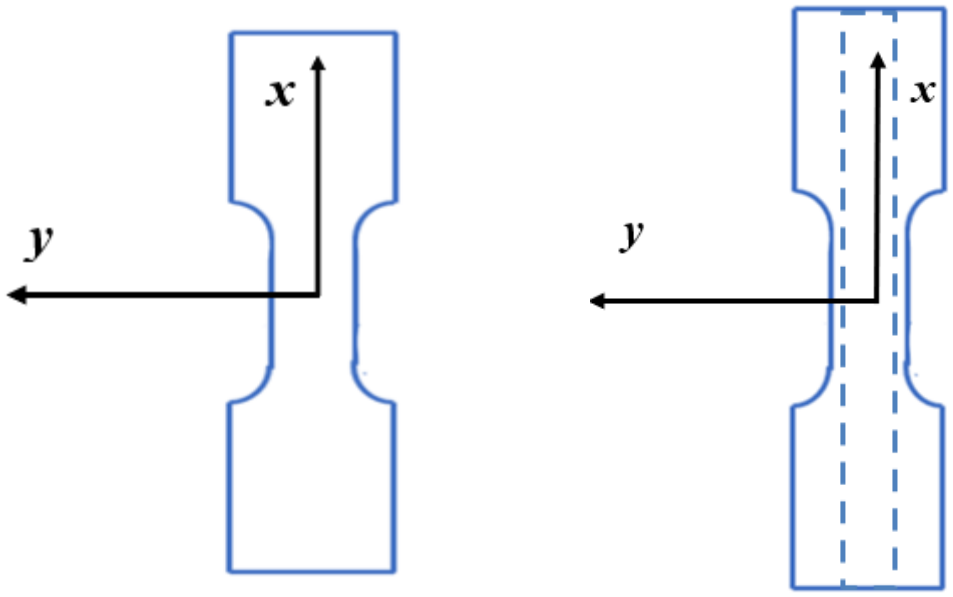

(a) (b)

Figure 4.3 Local specimen coordinate system for (a) flat dog-bone specimens and (b) tubular specimens. The longitudinal specimen axis is *x* for both specimen types

Table 4.2 shows the vector transformation from the global coordinate system to each local coordinate system shown in Fig. 4.3. The transformation matrices associated with Table 4.2 are used to transform stresses in the global system into the measured stresses in the local specimen coordinate system, developing the equations required to determine the Barlat Yld91 yield function parameters.

Table 4.2 Coordinate transformation from the global system (X, Y, Z) to local specimen system (x. y, z) for all five specimen geometries

Local / coordinate Specimen	***x***	***y***	***z***
RDD (0^o)	X	Y	Z
RDD (90^o)	- Z	Y	X
RDD (-45^o)	$\sqrt{2}/2$ (X - Z)	Y	$\sqrt{2}/2$ (X + Z)
LDD	X	Y	Z
LDT	X	Y	Z

4.1.2 Tubular Sample preparation

First, several 144.4 mm long tubular test specimens are extracted from the Al-6061T6 MT1 and MT2 bar extrusions. These specimens are machined to an outer diameter of 25.4 mm, with a measured internal diameter of 12.954 mm. As shown in Fig 4.4, a 30.48mm long test section with thickness 1.27mm and 3.175mm radii on each end is machined at mid-length. The specific geometry was designed to maintain a nearly uniform planar stress level in the central portion of the test section and avoid torsional buckling. Machining is performed using the internal diameter as a reference to ensure optimal concentricity with minimum wall eccentricity of the specimen. The inner and outer diameters of the tubular sample are measured using a Zeiss micro-computed tomography (MicroXCT) and mechanically via a T-gage and digital micrometer to assess the accuracy of the machining process. Table 4.3 shows the measured thickness of the specimen using micro-XCT. Fig. 4.5 presents XCT results and the measured test section thicknesses for the Al 6061-T6 sample. Results from these measurements indicate that the eccentricity (shift in the position of specimen longitudinal axis) in the gage section has a standard deviation less than +/- 0.001 mm over the length of the specimen.

4.1.3 Dog bone Specimen Preparation

As remarked in Section 4.1 and shown schematically in Fig 4.2, dog-bone specimens at different orientations are extracted from the same original bar. In this study, flat dog-bone specimens are extracted from the original bar in radial directions at different circumferential angles with respect to an arbitrarily selected X-axis direction in the Z-X plane (see Fig. 4.2). RDD Specimens are extracted from different radial directions, e.g., 0^0, $-45^{0,}$ and 90^0 with respect to the X-axis and denoted by RDD0, RDD45, and RDD90,

respectively. As presented in Fig 4.6, RDD specimens have a gauge length of 10 mm, a width of 3mm, and a thickness of 2mm. In addition to the radial specimens, another set of flat dog-bone specimens oriented along the length of the specimen (Y-axis in Fig. 4.2) are extracted. The LDD specimens have a longer gage length than the RDD specimen. As shown in Fig. 4.7, the gauge length of LDD samples is 50.8 mm with a width of 6.30 mm and a thickness of 5.08mm. The shoulder of specimens (RDD and LDD) were designed based on special grip requirements.

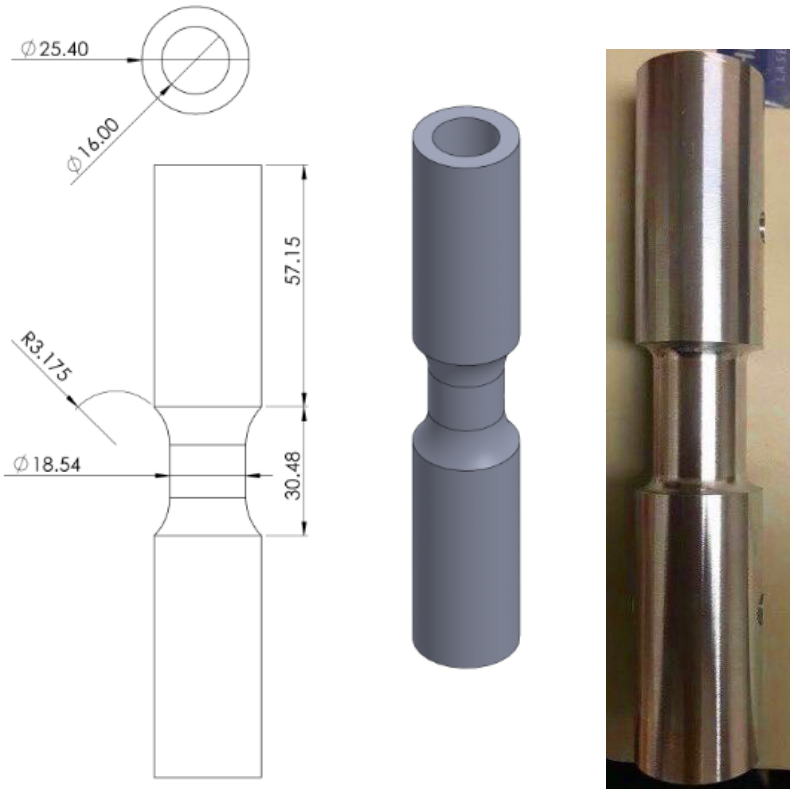

(a) (b)

Figure 4.4 Tubular specimen constructed in the longitudinal direction (LDT) from original bar (a) drawing of the test section, and (b) photograph of the test section. All units in mm.

Table 4.3 Measured thickness of the specimen using micro-XCT

Trial	Length(mm)	Outer Dia(mm)	Inner Dia(mm)	Thickness(mm)
1	30.5054	18.62511	16.08392	1.27061
2	30.48	18.57721	16.0593	1.258951
3	30.5054	18.57491	16.0593	1.257808
Mean	30.49693	18.59241	16.06751	1.262456
SD	0.014665	0.028342	0.01421	0.007084

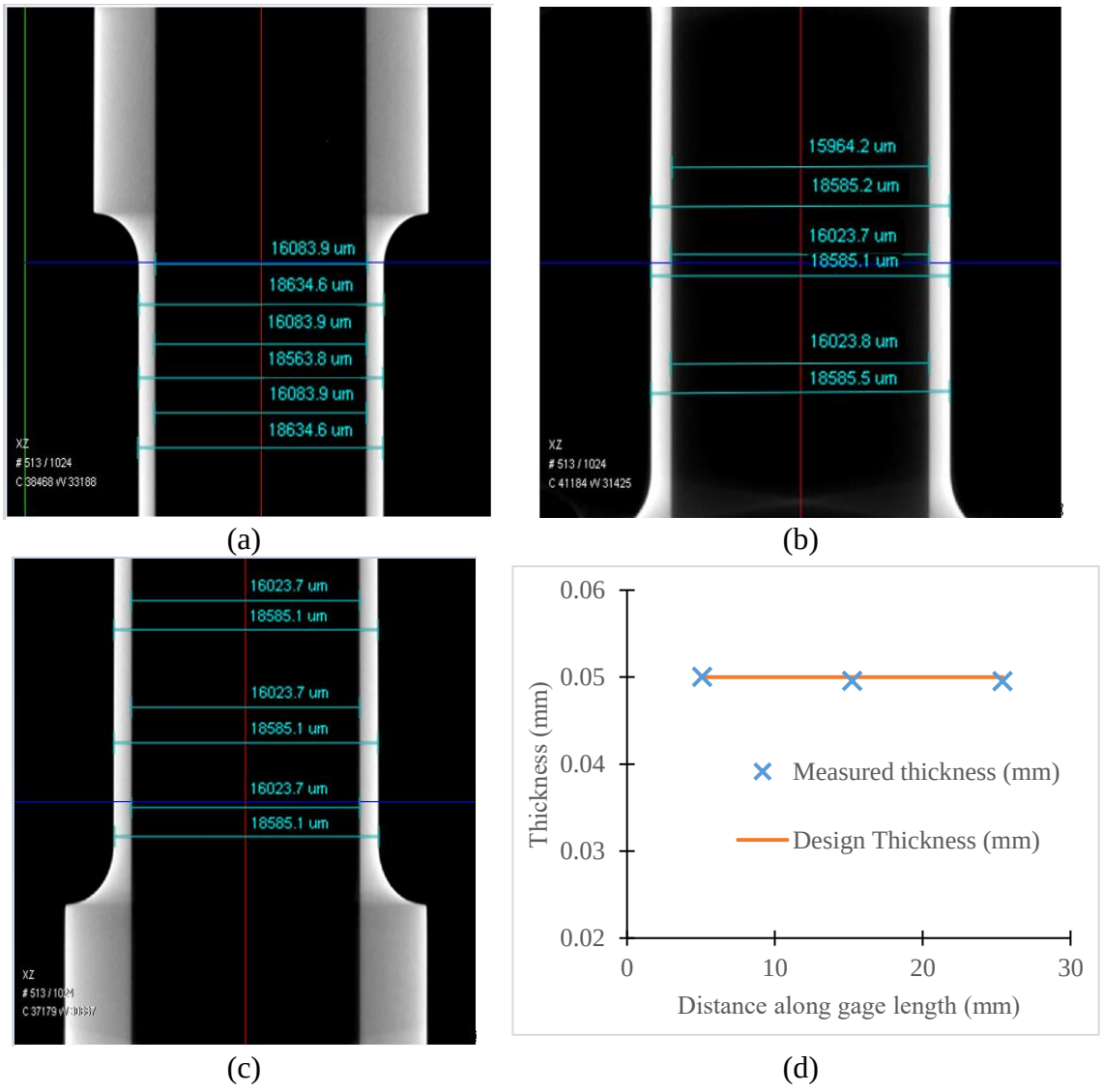

(a) (b) (c) (d)

Figure 4.5 XCT images with measurements in gauge region of the specimen including (a) top, (b) middle, and (c) bottom portions from XCT for a typical sample, (d)Graph of measured and design thicknesses of sample test region at top, middle and bottom of gage length. Variability is the order of 0.001mm.

4.2 INSTRUMENTATION

4.2.1 Tension Torsion Loading

The specimen is mounted in a TestResources electromechanical servo-controlled test machine with a capacity of 22 kN/300 N-m (5 kip/2.7 kips-inch) so that each specimen could be subjected to axial, torsional or axial-torsional loading in proportional/non-proportional combinations under load or displacement control. The test frame uses a variable speed electric motor, a gear reduction system, and a large mechanical screw to move the crosshead up or down and apply a torsional moment to the specimen. The test machine is shown in Fig 4.8. The rotary actuator transmits torque and rotation through an intermediate drive shaft, which includes a torsional load cell. The load cell, in turn, is connected to the lower gripping head. The servo motor or servo actuator moves at a controlled speed or loading rate. Electromechanical actuators are matched to static test applications, and electrodynamic and servo-hydraulic power packs can be used for higher-speed applications. They all deliver constant speed or torsional loading rates, which are tightly controlled. The tension-torsion load cell and displacement transducers record the axial force, torque, and the corresponding far-field axial and rotational displacements in real-time via a computer-based data acquisition system.

Custom gripping fixtures are designed and manufactured to attach the specimen to the test frame. The grip is made of grade 17-4 stainless steel. The fixture consists of a lower grip and an upper grip. Fig. 4.9 shows a schematic of the fixture with a mounted specimen, and Fig. 4.10 shows the entire load frame with a data acquisition system. Each lower and upper grip consists of three different parts. The 1st part, designated the base, is 19.05 mm (0.75 in) long and 114.3 mm (4.5 in) in diameter. The base part connects with an upper

load cell (lower load cell) using ¼-28 x 25.4 mm (1") Allen head cap screws. The design of the second part of the grip is complex and has multiple diameters. One portion of the 2nd part of the grip is 12.7 mm (0.5 in) long and 114.3 mm (4.5 in) in diameter on one side connecting with the base part using ¼-28 x 25.4 mm (1 in) Allen head cap screws. The other side of the 2nd part has a 57.15 mm (2.25 in) long and 69.85 mm (2.75-in) outer dia with 25.4 mm (1-in) inner dia half-circular tube. This side of the 2nd part is used to hold the sample using six bolts (grade 9 3/8-24 x 38.1 mm (1-1/2 in)) and two set screws (6.35mm (1/4 inch)). The third part of the grip is another half-circular tube with the same dimensions as the other side of 2nd part. To increase resistance to specimen slippage during torsional loading, two small holes were machined in the grip portion of the sample (Fig. 4.4) so that two set screws could be inserted. It is noted that the initial design combined the 2nd and 3rd parts into a single unit. When an initial set of trial experiments indicated slight slippage during torsional loading, the unit was cut into two pieces using an EDM system, with set screws inserted and used to increase the resistance of the grip to rotational slippage. The grips are shown in Fig. 4.10, along with the complete experimental setup, including the electromechanical tension-torsion test machine. Alignment of the system is verified using multiple uniaxial strain gages and rosette strain gages bonded to a 25.4 mm diameter solid aluminum calibration bar, as shown in Figs. 4.11 and 4.12, respectively. In the first experiment, tension is applied from 0 to 8000 N at a rate of 25 N/s. Results from the tension test are shown in Fig. 4.13(a). A second experiment is performed using the same strain gauge configuration while applying torque from 0 to 120 N-m at 0.1 N-m/s. The results for the simple torsion experiment are shown in Fig. 4.13(b). A third experiment is conducted, duplicating the procedure described for the second experiment while using two strain gauge

rosettes. The results from the second simple torsion experiment are shown in Fig. 4.14. The results presented in Figs. 4.13(a), 4.13(b), and 4.14 show that the results are consistent with expectations. The largest deviation is 50με for the axial strain due to torsional loading where γ_{max} = 1500με, confirming that the load cell and fixtures are well aligned when using the TestResources tension-torsion loading system. Proper specimen alignment within the test frame is essential to eliminate bending moments and off-axis torsional twisting of the specimen. The presence of such effects will invalidate the analysis of the elastic-plastic response, which is `based on the assumption that torque and axial load are the only mechanical moments and forces applied to the specimen.

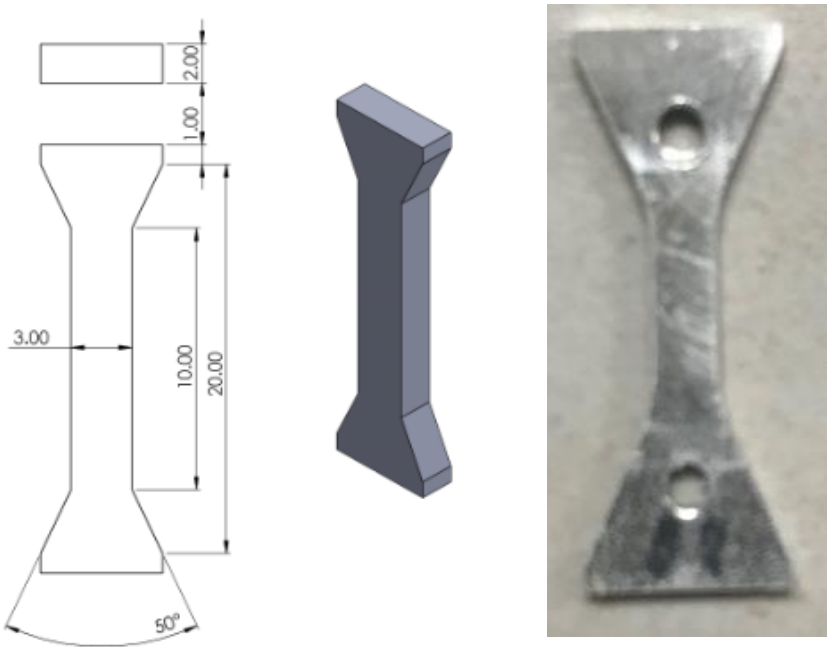

(a) (b)

Figure 4.6 Dog bone specimen constructed in the radial direction (RDD) (a) drawing of the test section, and (b) photograph of the test section. All units in mm.

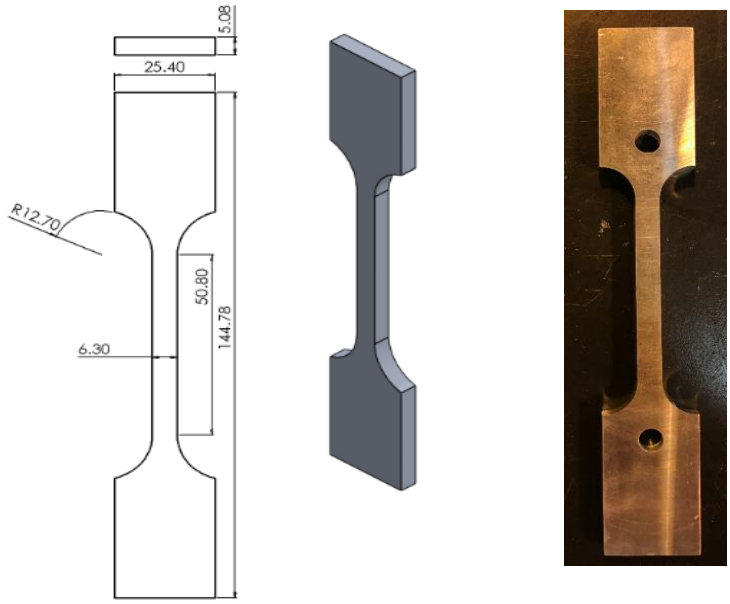

(a) (b)

Figure 4.7 Dog bone specimen constructed in the longitudinal direction (LDD) from original bars (a) drawing of the test section, and (b) photograph of the test section. All units in mm.

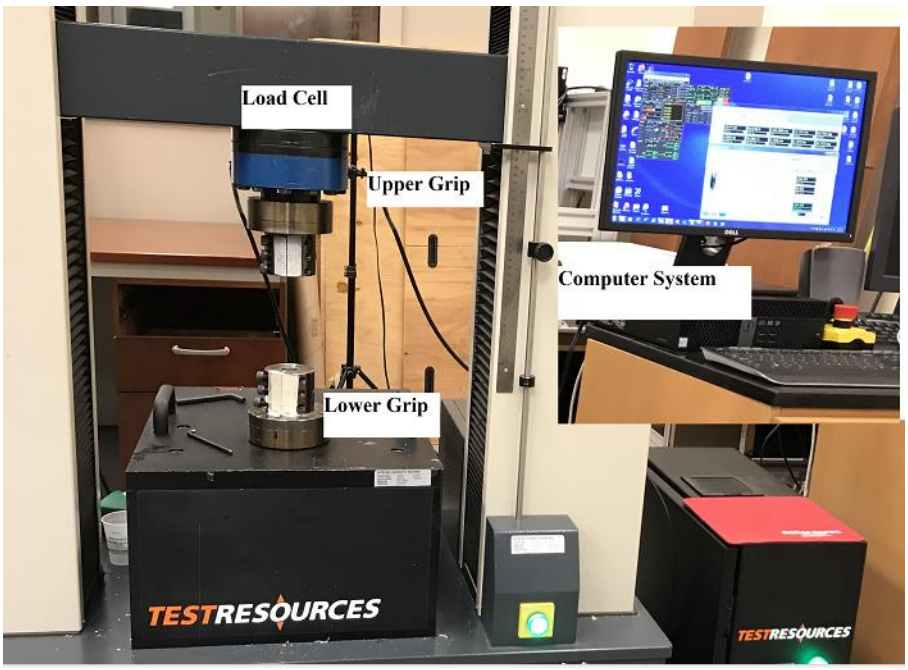

Figure 4.8 TestResources load frame equipped for uniaxial tension, combined tension torsion, and simple torsion testing

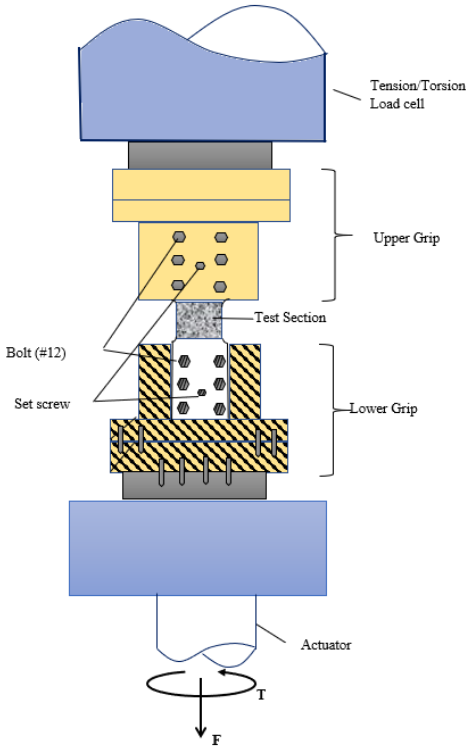

Figure 4.9 Schematic of the Grip with a mounted specimen

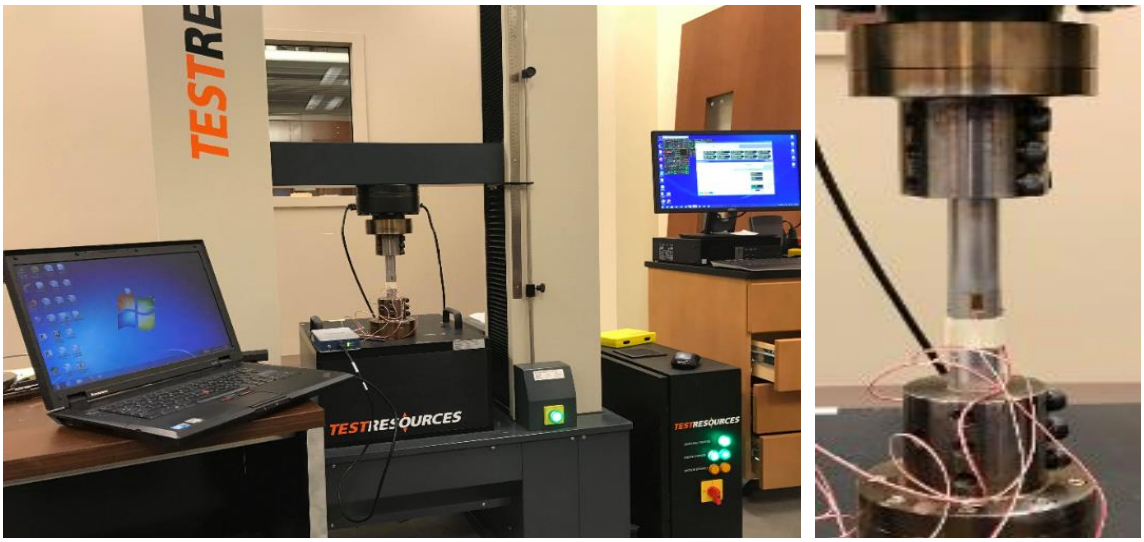

(a) (b)

Figure 4.10 Experimental setup for calibration studies: (a) Strain gage with NI Signal Express data acquisition system positioned with the electromechanical tension-torsion testing system. (b) test fixture with calibration bar and attached strain gages.

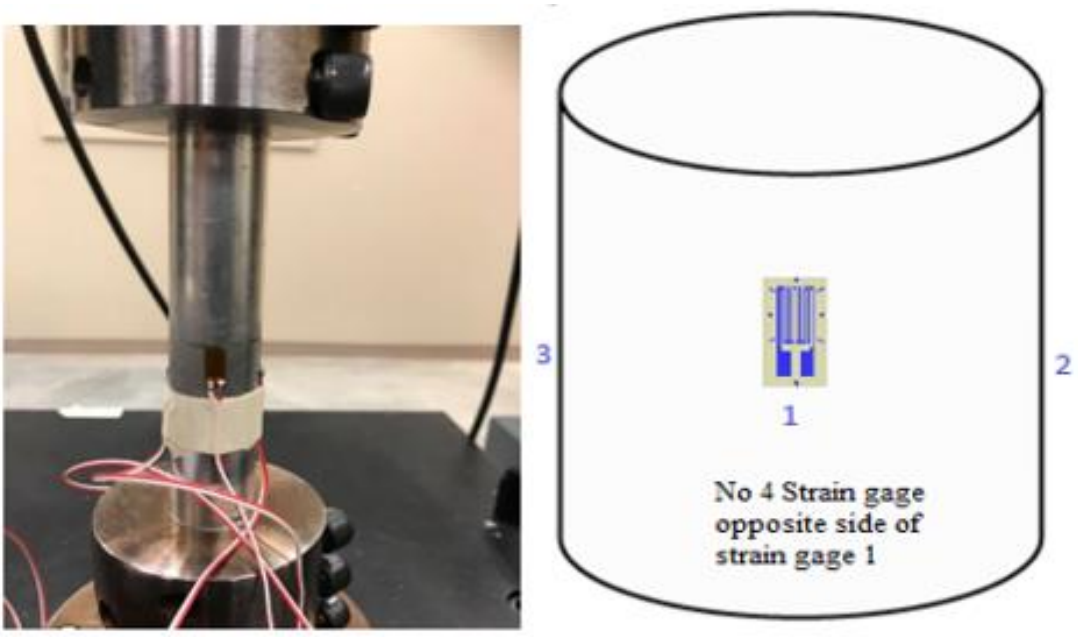

Figure 4.11 Actual and schematic images of strain gage on Aluminum 1in (25.4mm) solid specimen

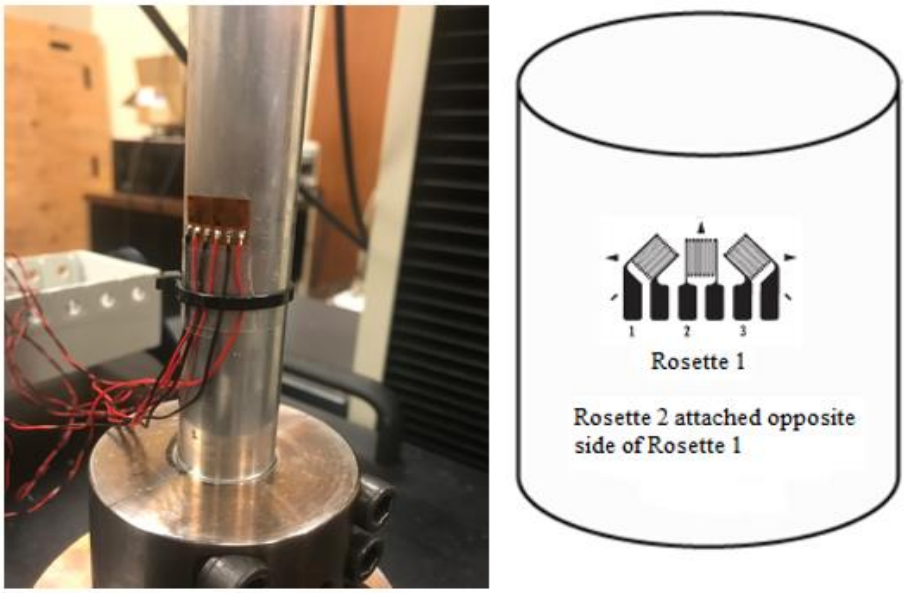

Figure 4.12 Actual and schematic images of Rosette strain gage on Aluminum 1in (25.4mm) solid specimen

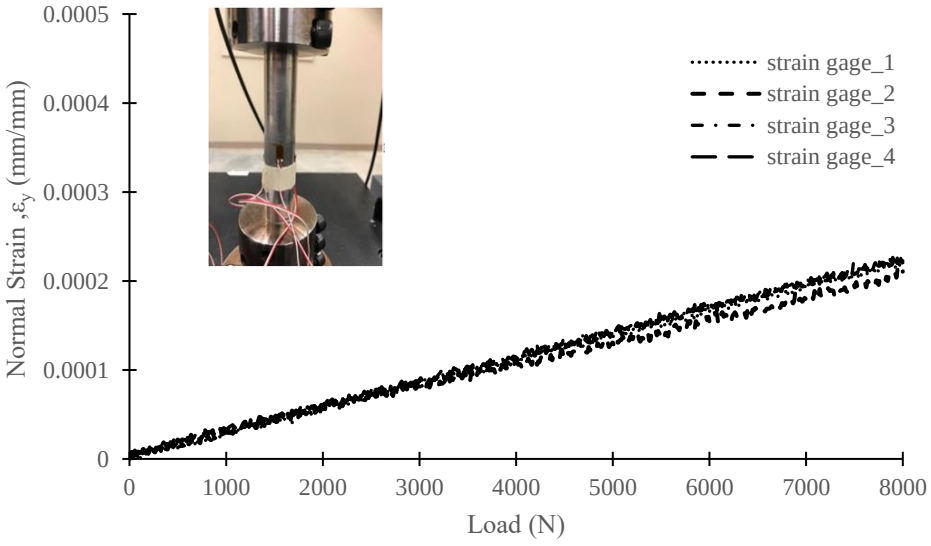

(a)

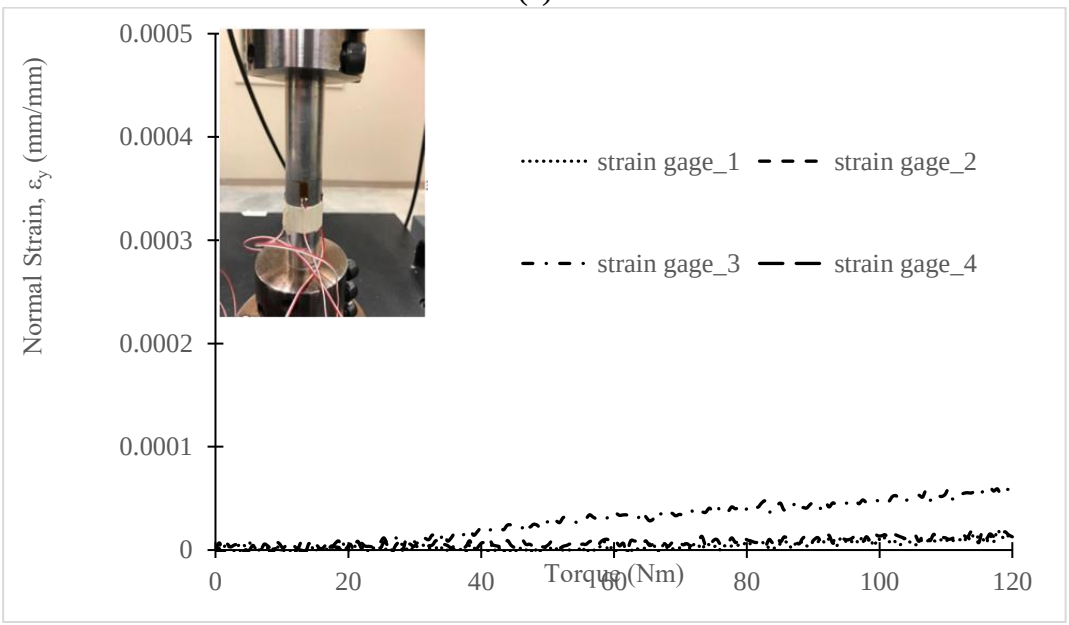

(b)

Figure 4.13 Experimental result from calibration studies including (a) normal strain vs. axial load for uniaxial tensile experiment and (b) normal strain vs. torque for torsion experiment using four strain gage configurations for measurements.

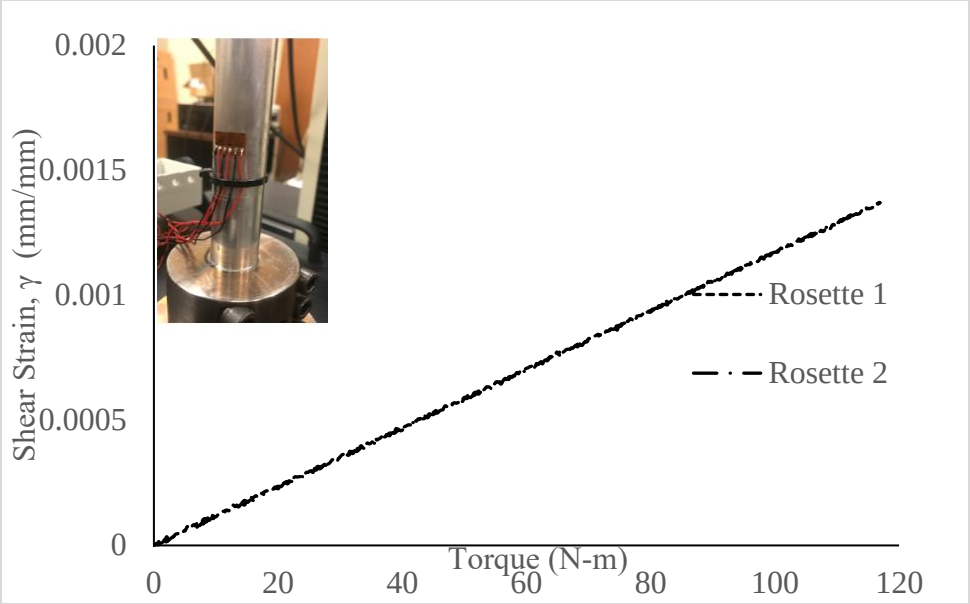

Figure 4.14 Experimental results for shear strain vs. torque for torsion experiment with two strain gage rosette configurations Psylotech micro-tensile test

4.2.2 Psylotech micro-tensile test

The Psylotech μTS system is a flexible mesoscale test system that is designed to be used in conjunction with a microscope and stereo digital image correlation (StereoDIC) system to measure stress/strain, stress relaxation, and creep experiments on a wide range of materials. The system consists of three main components: the mechanical load frame, control computer, and test hub. The system is controlled with a Windows 7 x64 based Intel PC. The computer controls the test frame in real-time. The control computer is currently separate from the StereoDIC image acquisition computer but is synchronized with the loading process. The system is controlled with a National Instrument's LabVIEW Program and PCI Express data acquisition card [DAQ card]. All the software and hardware are installed on the computer. The test system is shown in Fig. 4.15.

4.2.3 MTS material testing system

In these studies, the LDD specimens were tested on a separate electromechanical test frame; an MTS Exceed Series E43 Material Test System. The system is comprised of a load frame, electronic frame controller, and testing software. The load frame has a rectangular shape and includes a base unit and two vertical columns. The two-column models have a fixed upper transverse beam. Precision ball screws drive the moving crosshead on the load frame. The crosshead is coupled to the ball screw(s) with high-strength, precision ball nuts, and rides on ball bearings. This configuration is very efficient in minimizing friction and wear. The load frame drive is within the frame base. The drive motor is connected to the lower end of the ball screws by a series of belts and drive pulleys. On the two-column machines, motor rotation drives synchronous rotation of the ball screws, which moves the crosshead up or down. The test system is shown in Fig. 4.16.

4.2.4 Stereo digital image correlation

Surface strain measurements for all tubular specimens subjected to tension, torsion, and combined tension-torsion were conducted using the non-contacting measurement method StereoDIC (Sutton et al., 2009. StereoDIC requires two or more cameras to view the region of interest. Fig. 4.17 shows a general schematic of the process used with a pinhole perspective projection model to convert stereo digital images into the full-field 3D measurement of surface positions and surface displacements for all points, P, on an object that is imaged by the cameras. To perform stereo-triangulation with both cameras and obtain metric surface data, the stereo camera system must be calibrated in a common world coordinate system.

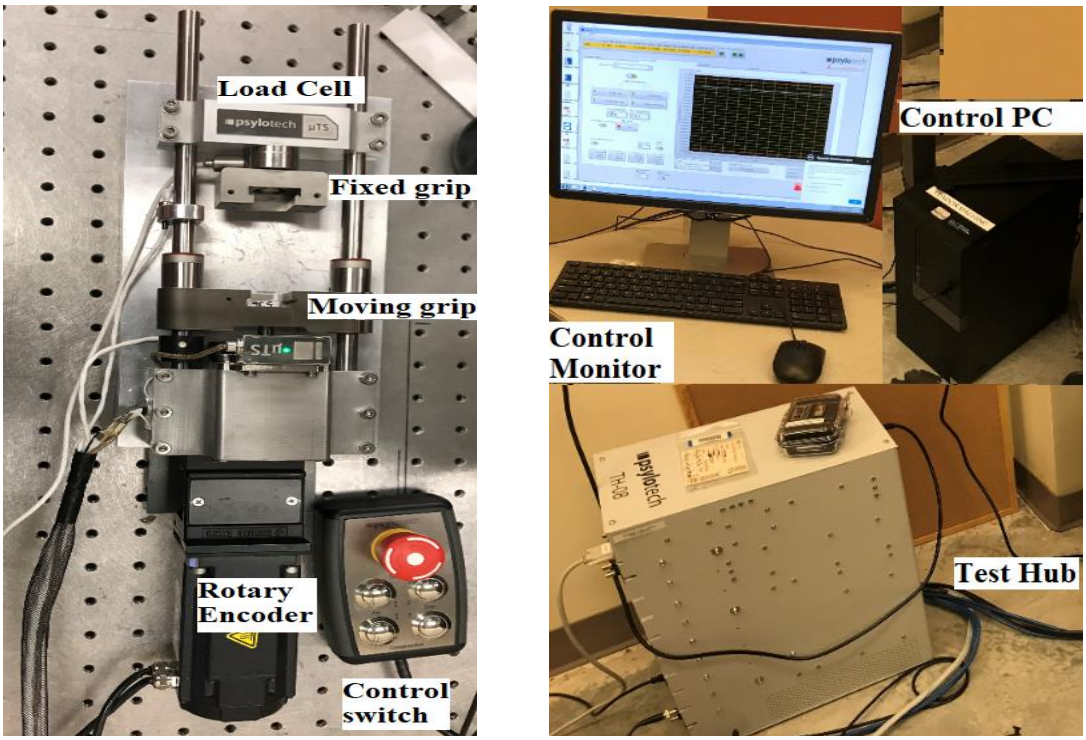

(a) (b)

Figure 4.15 Psylotech (a) µTS system, (b) Test Hub, Control PC, Control PC Monitor

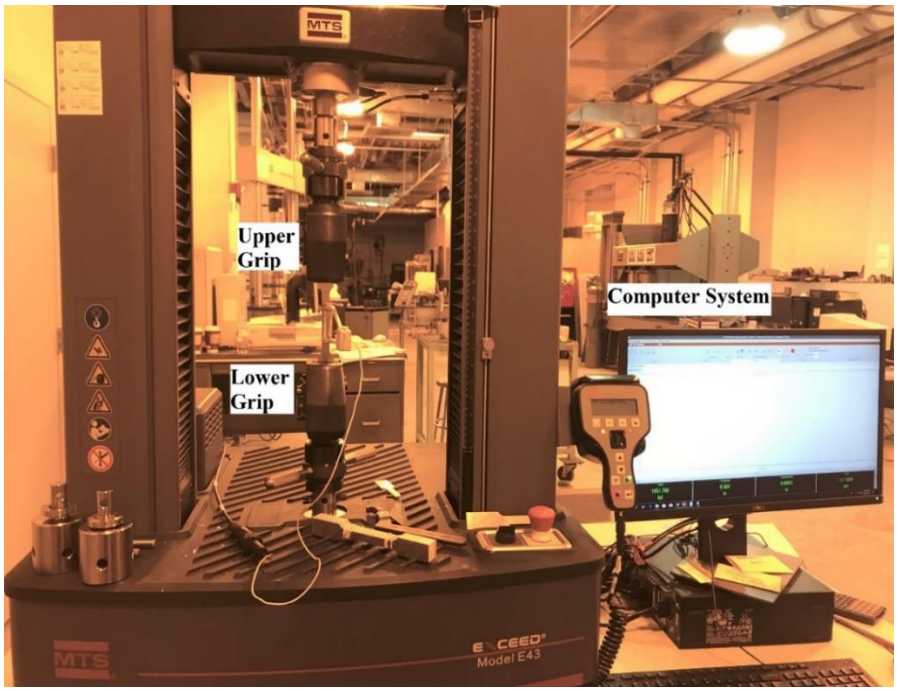

Figure 4.16 MTS Model E43Electromechanical Test System

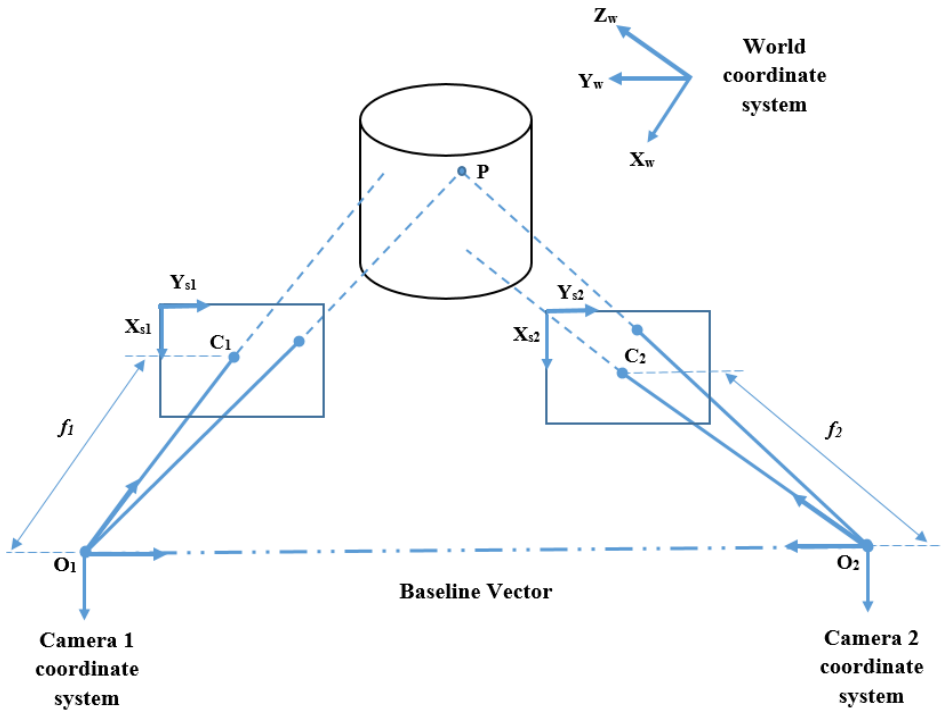

Figure 4.17 Schematic of the process used with a perspective projection model to convert stereo digital images into 3D measurements of position and displacement

As shown in Fig. 4.17, stereo views of a common grid pattern may be used to define a common world coordinate system for all cameras, thereby providing the basis for relating image locations in all cameras to a common 3D position. The calibration process establishes transformations between the common world coordinate system and each camera's sensor plane coordinate system. As shown in previous studies (Sutton et al., 2008, 2009, Yasmeen et al.,2017, 2018), stereovision systems use multiple camera views to estimate all three components of displacement simultaneously. Hence, the measured 3D displacement field should be such that the in-plane components of displacement are and the out-of-plane components are measured simultaneously.

Calibration of the stereovision system is performed using 20-60 images of a translated and rotated planar dot pattern with reasonably well-known spacing (Sutton et al.

(2008, 2009), Yasmeen et al., (2017, 2018)). For a stereovision system (stereo-rig), different calibration parameters are presented in Fig. 4.18. Fig. 4.19 shows the photograph of the StereoDIC camera system and a stereomicroscope for acquiring stereo images to be analyzed with StereoDIC software. Detailed specifications for the camera systems that are used in the experiments are provided in Sections 4.3.2 and 4.3.3.

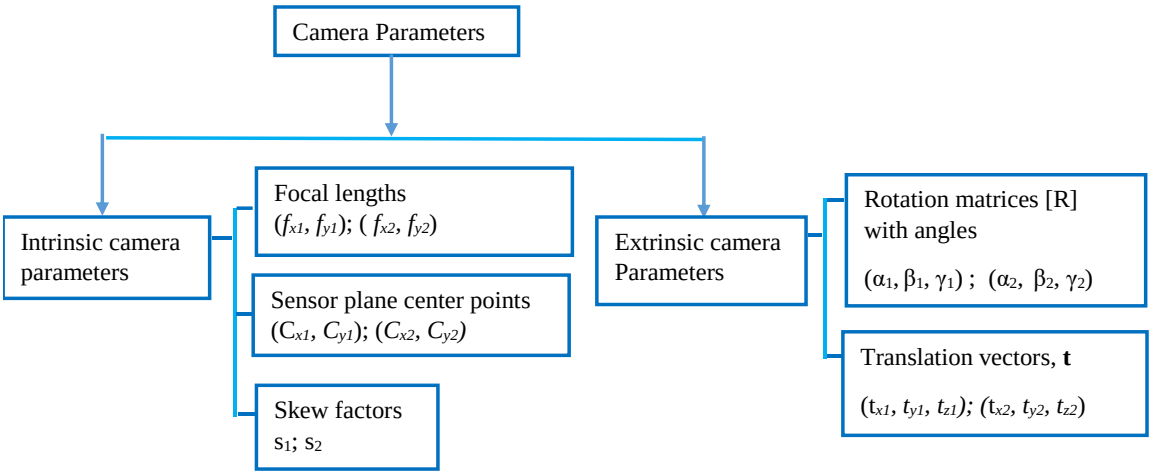

Figure 4.18 Calibration parameters (Yasmeen et al. 2018)

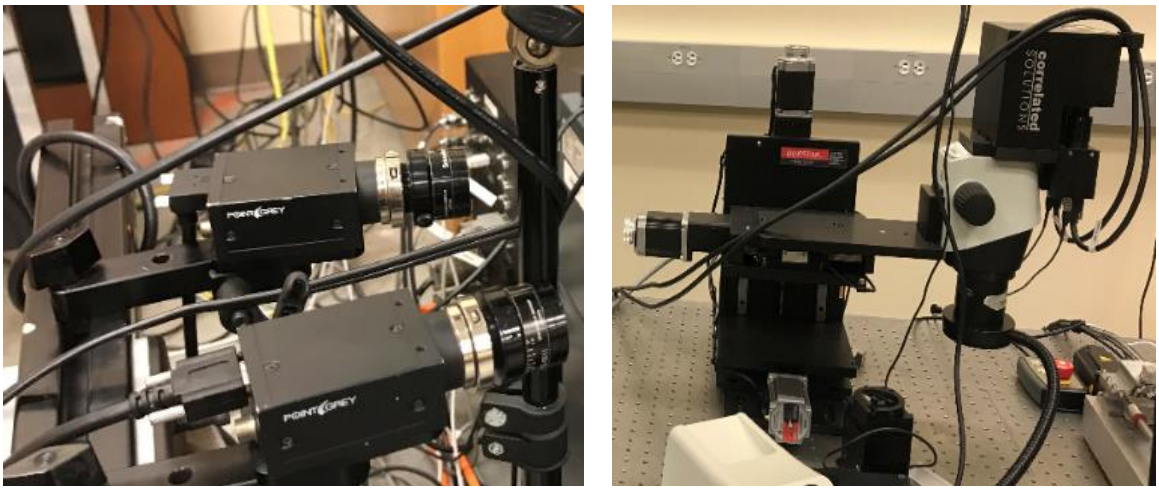

(a) (b)

Figure 4.19 (a) StereoDIC camera system. (b) Stereomicroscope for high magnification stereo imaging.

4.3 EXPERIMENTAL PROCEDURE-

4.3.1 Tubular Specimens

In this work, several experiments are performed with the calibrated test system shown in Fig. 4.8. These include (a) uniaxial tension, (b) proportional tension-torsion, and (c) simple torsion loading of the 144.78 mm long tubular specimens. In all cases, the nominal applied axial stress and shear stress (σ_{YY}, σ_{XY}) in the central gauge section of the specimens are calculated using the measured loads and specimen geometry. For the tubular specimen undergoing torsion-tension loading, the axial tensile stress $\sigma_{yy} = F_y/A_y$ and the torsional shear stress $\sigma_{xy} = T / r A_y$ (Meguid and Malvern(1983)). In these equations, F_y is the axial force, A_y is the cross-sectional area given by $A_y = \pi (r_o^2 - r_i^2)$, T is the torque, r is the mean radius for thin-walled specimens $r = (r_o + r_i) /2$, with outer and inner tube radii r_o and r_i, respectively.

For LDT specimens undergoing torsion-tension loading, the combined loading parameter, β, is defined as follows:

$$\beta = \frac{\sigma_{XY}}{\sigma_{YY}}, \qquad \beta = constant > 0 \tag{4-1}$$

with $0 \leq \beta \leq \infty$, For $\beta = 0$, the specimen is undergoing uniaxial loading. For $\beta = \infty$, the specimen is undergoing simple torsion.

The following process describes the various loading states achieved in this work. As shown in Table 4.4, two experiments are performed for each β. In all cases, the results are within 1% for the measured average strains in the region of interest. For each β, the average strain from the two experiments for each set of loads is used for further analysis.

All experiments were performed in load control mode: torque control for torsion ($\beta = \infty$), tensile load control for tension ($\beta = 0$), and both torque and tensile load control for all other β. Since the primary interest is in the stress-strain state for the central gauge section (outside diameter of 18.54 mm with constant 1.27mm thickness), Table 4.4 details the stress loading paths for uniaxial tension, proportional tension-torsion, and torsional loading, with sample experimental data for all loading paths given in Fig. 4.20.

The axial and shear strains on the surface of the specimen were measured using stereo imaging to acquire synchronized images and VIC-3D version 9 software from Correlated Solutions Inc. (www.correlatedsolutions.com) to perform StereoDIC. To obtain speckle images for StereoDIC, each aluminum specimen is lightly coated with flat white paint and then speckled using a can of flat black spray paint. The resulting speckle pattern and the corresponding grey-level histogram for the recorded pattern are shown in Fig. 4.21

Since the LDT specimens undergo relatively large rotations during torsional loading, the macroscale grid in Fig. 4.22 (a) with 14 x 10 dots on a 5mm spacing was rotated 20-60 times to acquire stereo images that were analyzed using the Large Angle Calibration" (LAC) process (Yasmeen et al., 2018). The experimental setup used for tubular specimens, including the stereovision optical imaging system, is shown in Fig. 4.23. After mounting both cameras on a rigid crossbar, the crossbar is secured to a tripod, and the stereo-vision system is positioned at approximately 1 m from the specimen surface. Cameras were oriented at a relatively small stereo angle of 9.5°, which was considered acceptable since the main goal was to analyze in-plane rather than out-of-plane motions of the specimen. Table 4.5 summarizes all components in the stereovision optical system. As mentioned above, the commercial VIC-3D DIC software is used to determine surface

strains. Table 4.5 shows the camera lenses and StereoDIC calibration parameters obtained by the VIC-3D software during calibration. To estimate random variability in the surface strain measurements using StereoDIC, the central regions of fifteen images of the specimen acquired with no load are analyzed. The standard deviations in each in-plane strain component with no load are shown in Table 4.6. Inspection of Table 4.6 shows that the maximum variability range is ± 47.1με, which represents a standard deviation of 15.7με.

Since all strain data are obtained through analysis of non-contacting stereovision images with image analysis performed by the VIC-3D software package; it is important to know the level of variability in the average strain measurements for the axial strain, $\varepsilon_{yy\ mean}$, and the in-plane shear strain, $\varepsilon_{xy\ mean}$, where x is the tangential direction to the surface at each point (corresponding to the circumferential direction at any point for cylindrical specimens).

For the cylindrical torsion-tension specimens in Table 4.4, Table 4.7 shows both the average strains $\varepsilon_{xy\ mean,}$ and $\varepsilon_{yy\ mean}$, the amplitudes of the total ranges, designated $(\varepsilon_{xy})_{var}$ and $(\varepsilon_{yy})_{var}$, and the ratios $(\varepsilon_{xy\ mean})/(\varepsilon_{xy})_{var}$ and $\varepsilon_{yy\ mean})/(\varepsilon_{yy})_{var.}$ Also shown is the ratio of the variability in ε_{yy} and ε_{xy} during mechanical loading relative to the baseline Noise Level when no load is applied, designated NL. In our experiments, the measured baseline no-load strain Noise Level is NL = 50με for all strain components. . Though not shown in the table, similar results are obtained for variability in the strain, $\varepsilon_{xx\ mean}$, which is relatively small in comparison to $\varepsilon_{yy\ mean}$ and $\varepsilon_{xy\ mean.}$. Table 4.7 outlines typical variability in strain measurements using macro-scale stereovision system LDT specimen in the case of β = 0.936.

Fig. 4.24 presents strain and strain rate versus time data for uniaxial tension, simple torsion, and combined proportional torsion-tension loading experiments of the tubular specimen. As shown in Fig. 4.24, strain rates are extremely low for all loading conditions; since the degree of sensitivity of Al 6061-T6 to strain rate is minimal at low strain rates (Nicholas,1981), these results indicate that measurements from all experiments in this work are not affected by the low applied strain rates.

Table 4.4 Multiaxial stress states in central gage section for various loading paths

Path No	Path Description	Material	β	σ_{xx} (Mpa)	σ_{xy} (Mpa)	Number of Experiments
1	Tension loading	MT1	0	321.05	0	2
2	Proportional	MT1	0.234	289.50	67.78	2
3	Proportional	MT1	0.468	245.24	114.84	2
4	Proportional	MT1	0.936	172.69	161.73	2
5	Proportional	MT1	1.872	103.03	192.98	2
6	Simple Torsion	MT1 and MT2	∞	0	208.36	6

4.3.2 Dog bone specimens

Two different experimental setups are used for the RDD and LDD dog-bone specimens shown in Figs. 4.6 and 4.7, respectively. The experimental plan for the tension experiments using dog-bone specimens is given in Table 4.8.

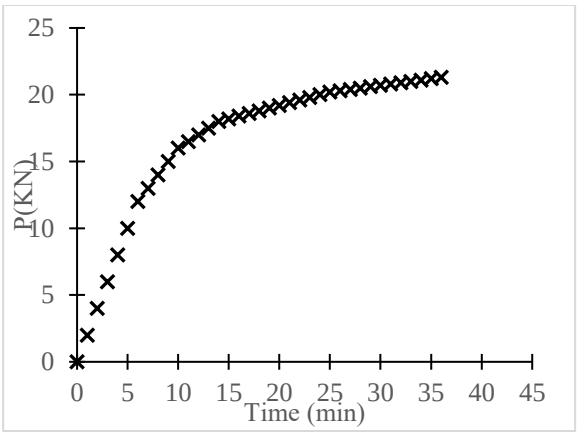

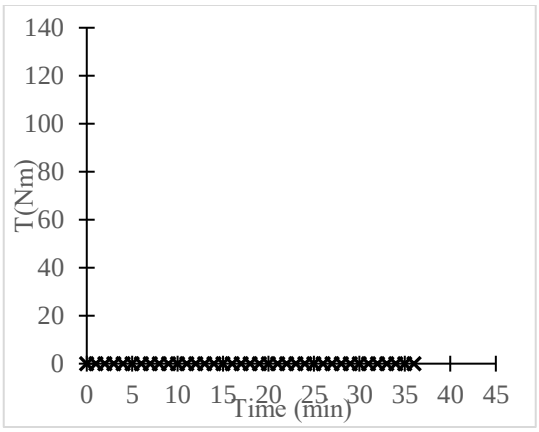

(a) β = 0

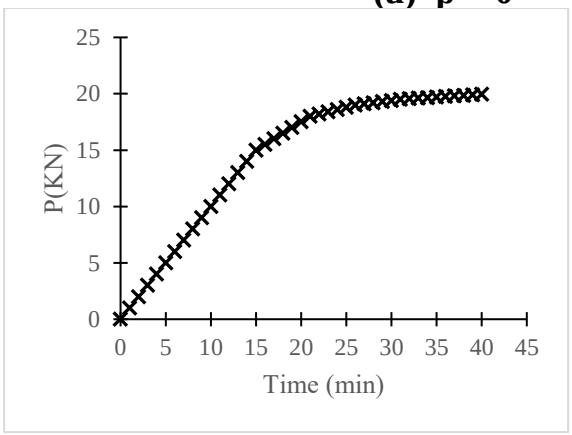

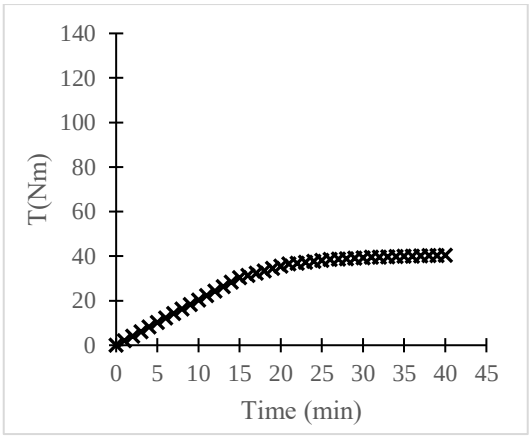

(b) β = 0.234

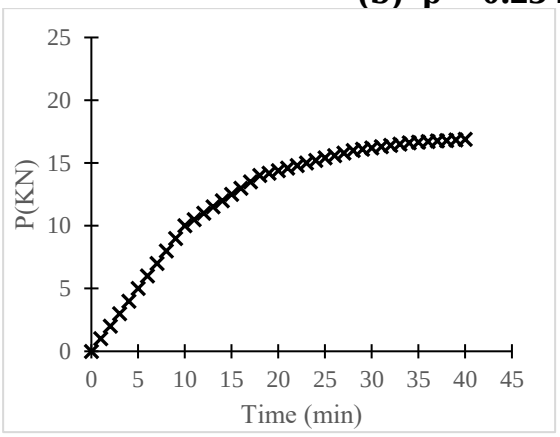

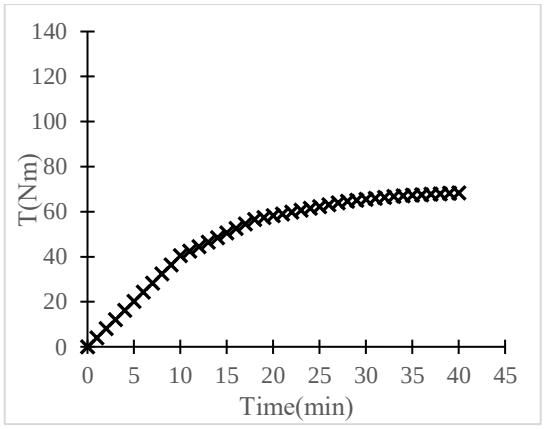

(c) β = 0.468

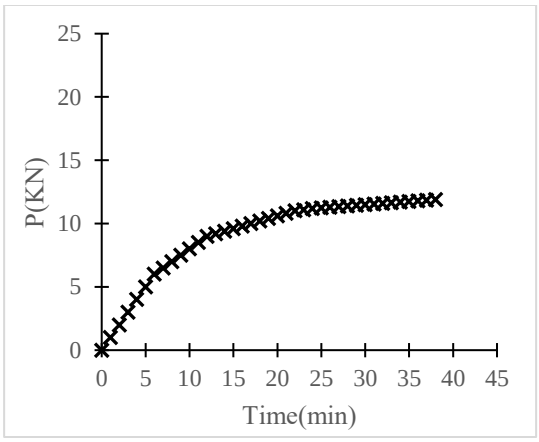

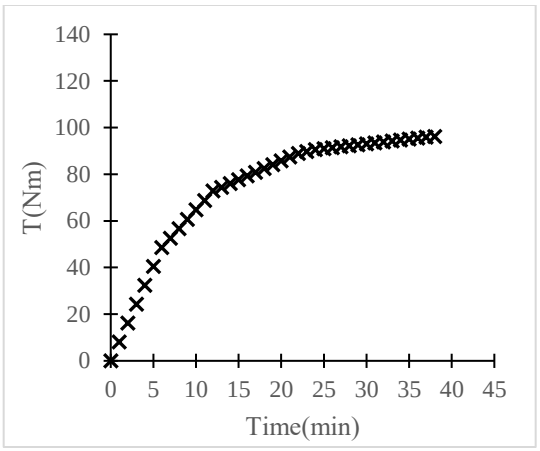

(d) β = 0.936

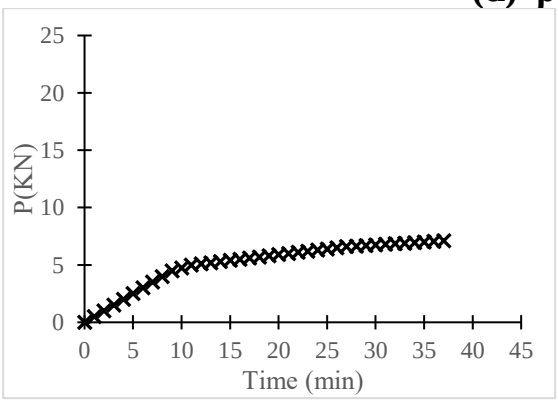

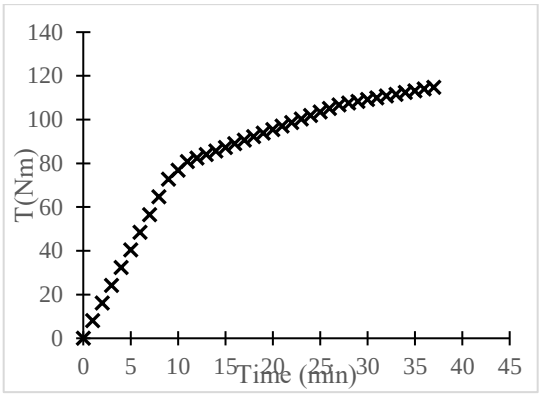

(e) β = 1.872

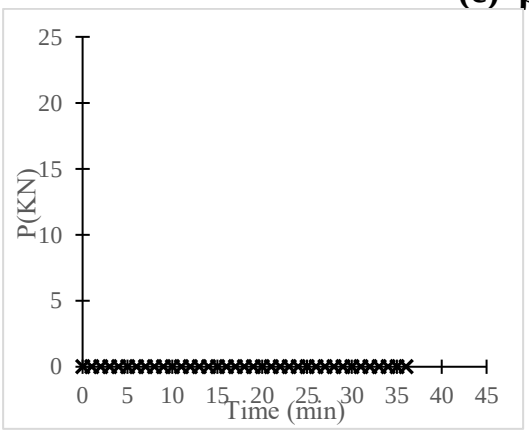

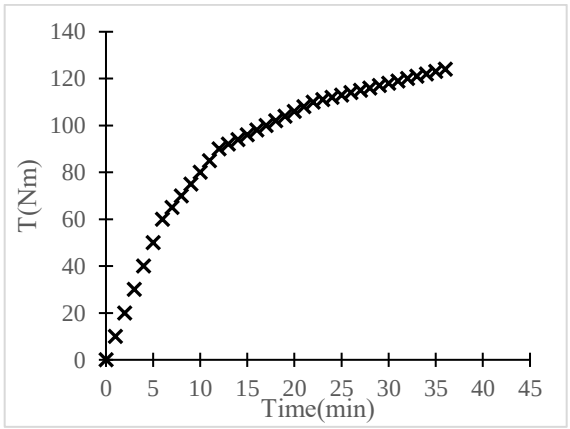

(f) β = ∞

Figure 4.20 Axial load vs. Time and Torque vs. Time for tubular specimens subjected to (a) uniaxial tension, β = 0, (b) tension-torsion, β = 0.234, (c) tension-torsion, β = 0.468, (d) tension-torsion, β = 0.936, (e) tension-torsion, β = 1.872, (f) torsion, β = ∞

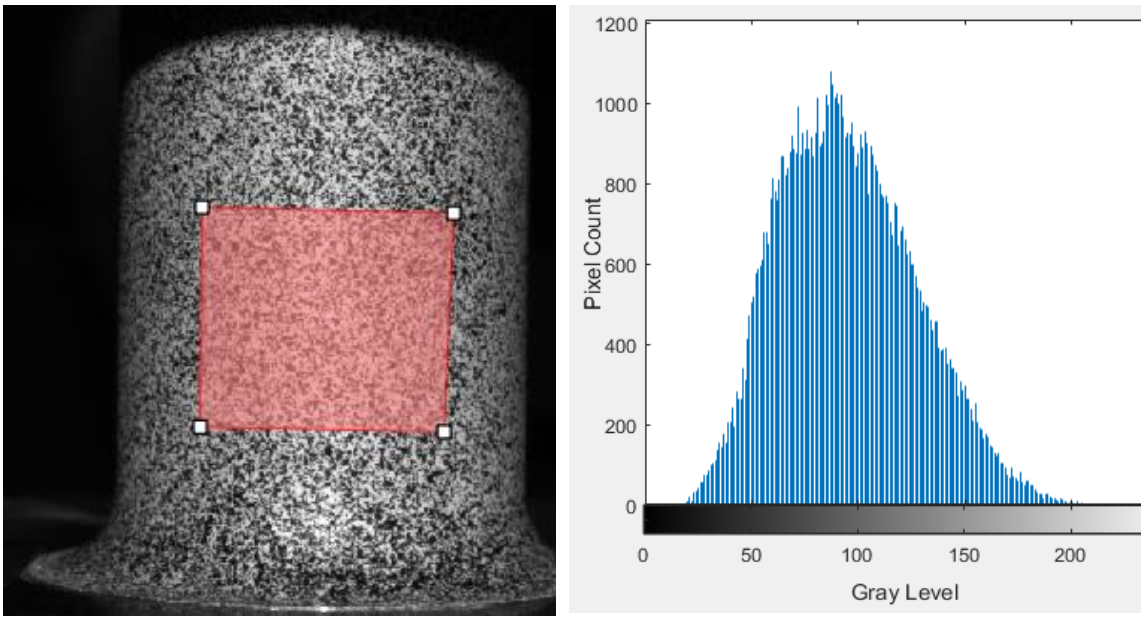

(a) (b)

Figure 4.21 Speckle Pattern on a tubular specimen with (a) square 250 x250 pixel^2 region where strain data is analyzed and (b) grey level histogram for pattern.

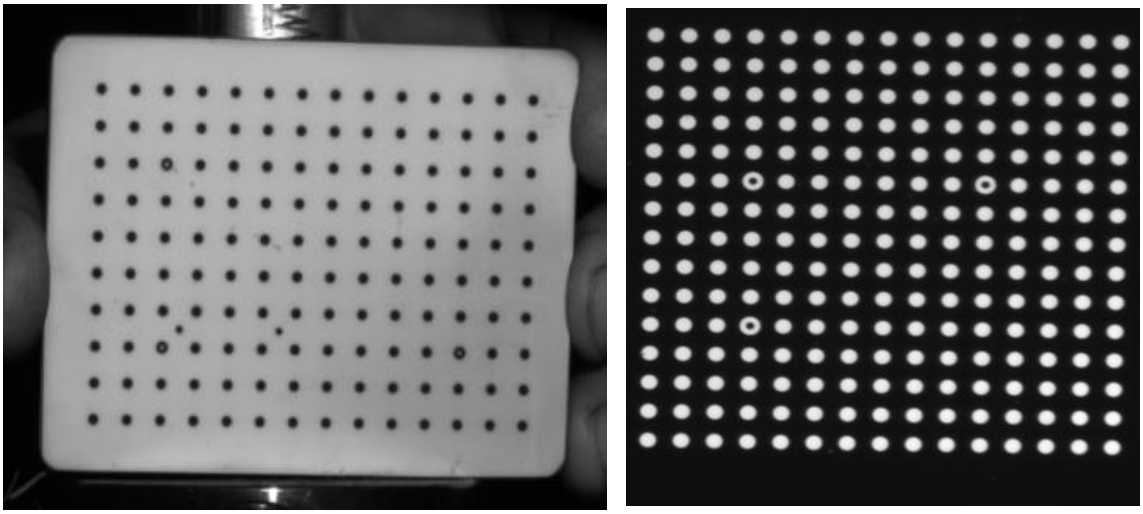

(a) (b)

Figure 4.22 Calibration grid for calibration of stereovision systems using (a) macroscale camera system with VIC-3D software (14 × 10 dot grid, 5 mm) (b) CSI microscope and VIC-3D software (15×15 dot grid, 0.28 mm) .

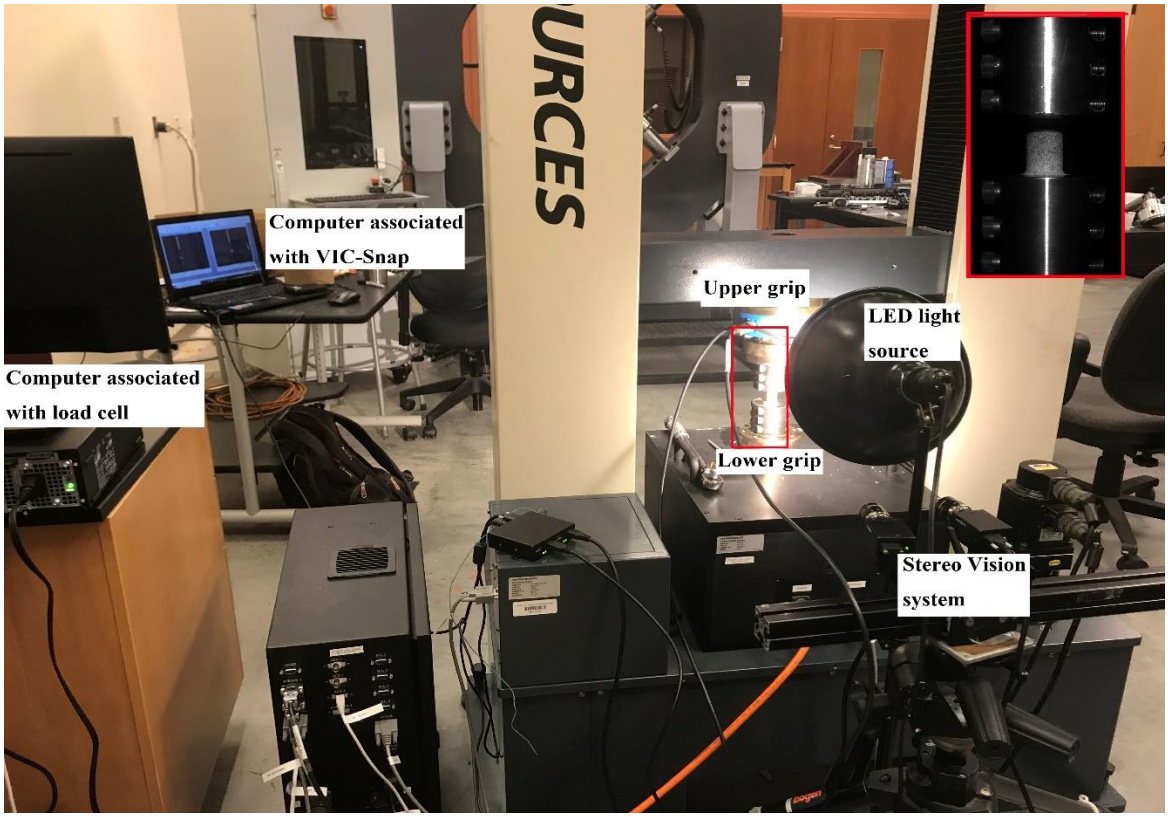

Figure 4.23 Electromechanical testing system with stereovision system, lighting and load frame for combined tension torsion experiments with tubular specimens.

Experiments for the miniature dog-bone specimens, RDD0, RDD45, and RDD90, required the most complex experimental setup, including (a) the Psylotech micro-tensile test system(Psylotech Incorporated, 2006) shown in Fig. 4.15, (b) the adjustable CSI optical microscope shown in Fig. 4.19 and (c) the specialized back-lit calibration pattern manufactured by CSI shown in Fig. 4.22(b)) with calibration methodology for microscopic StereoDIC (Correlated Solutions, Inc, 1998). The microscale speckle pattern is produced by applying a thin coat of white paint and sprinkling black paint using an airbrush system. The speckle pattern and gray level histogram for microscope imaging is shown in Fig. 4.25. The detailed experimental setup of a microscale tensile loading system with stereo-microscope (Correlated Solutions, Inc,1998) for surface strain measurements is shown in Fig. 4.26. Details regarding the StereoDIC measurements are given in Table 4.9. For a flat tensile specimen, Table 4.10 shows the average axial strain $\varepsilon_{yy\ mean}$, the amplitude of the

total strain range (designated $\varepsilon_{yy\ var}$), the ratio $(\varepsilon_{yy\ mean})/(\varepsilon_{xy\ var})$ and the ratio $(\varepsilon_{yy\ var})/NL$. Though not shown in the table, similar results are obtained for the variability in strains, $\varepsilon_{xx\ mean}$ and $\varepsilon_{xy\ mean,}$ both of which are small in comparison to the axial strain.

Table 4.5 Camera lenses, StereoDIC (VIC-3D)system parameters

Parameter#	Vic-3D
Test Type	Tension, torsion, combined tension torsion
Specimen	Al 6061 T6 Tube
Cameras	Grasshopper3 GS3-U3-91S6M (8bits,
Lenses	Schneider XENOPLAN 1.9/35-0511
Lighting	White LED Lighting
Calibration	14 × 10 dot grid, 5 mm dot size (H95-00-03),
Lens distortion	As 1st order radial distortion correction
Subset size	29 × 29 pixels^2
Step size	7 pixels
Filter type	Center-weighted
Shape function	Affine
Strain filter	5 x 5
Strain	Lagrangian large strain tensor definition for all
Field of View	150mm X 120 mm
Average	0.25mm

Table 4.6 Variability in Strain components at no loading condition

Strain component	Standard deviation (mm/mm)
ε_{xx}	$\pm 3.936 \times 10^{-5}$
ε_{xy}	$\pm 3.160 \times 10^{-5}$
ε_{yy}	$\pm 4.710 \times 10^{-5}$

Table 4.7 Typical variability in strain measurements using macro-scale stereovison system LDT specimen ($\beta = 0.936$)

σ_{yy} (Mpa)	$(\varepsilon_{yy})_{mean}$ ($\mu\varepsilon$)	$(\varepsilon_{yy})_{var}$ ($\mu\varepsilon$)	$(\varepsilon_{yy})_{var}/(\varepsilon_{yy})_{mean}$	$(\varepsilon_{yy})_{var}$/ NL	$(\varepsilon_{xy})_{mean}$ ($\mu\varepsilon$)	$(\varepsilon_{xy})_{var}$ ($\mu\varepsilon$)	$(\varepsilon_{xy})_{var}/(\varepsilon_{xy})_{mean}$	$(\varepsilon_{xy})_{var}$/ NL
0 (No	20	30	-	-	50	41	-	-
14.51	234.80	114.00	0.49	3.80	180.00	101.00	0.56	2.46
72.56	1138.00	114.00	0.10	3.80	1257.00	178.00	0.14	4.34
116.09	1773.00	152.00	0.09	5.07	2050.00	237.00	0.12	5.78
139.31	2250.00	175.00	0.08	5.83	2550.00	145.00	0.06	2.90
159.62	3502.00	265.00	0.08	8.83	3850.00	267.00	0.07	6.51
166.88	7301.00	511.00	0.07	17.03	8050.00	551.00	0.07	13.44
171.23	17700.00	838.00	0.05	27.93	19050.00	900.00	0.05	21.95

Table 4.8 Experimental Specimens and Loading Conditions

Trial No	Material	Mode	Load cell	Strain Measurement Approach	Specimen Type	Number of Experiments
1	Al 6061-T6 MT1 and MT2	Tension	MTS	Extensometer	LDD	2
2		Tension	Psylotech micro- tensile tester	VIC 3D with stereo microscope	RDD0	2
					RDD45	2
					RDD90	2

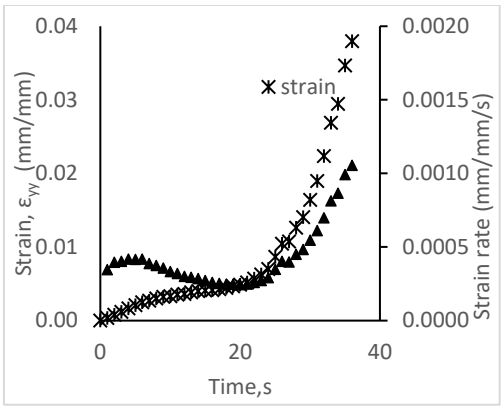

(a) β = 0

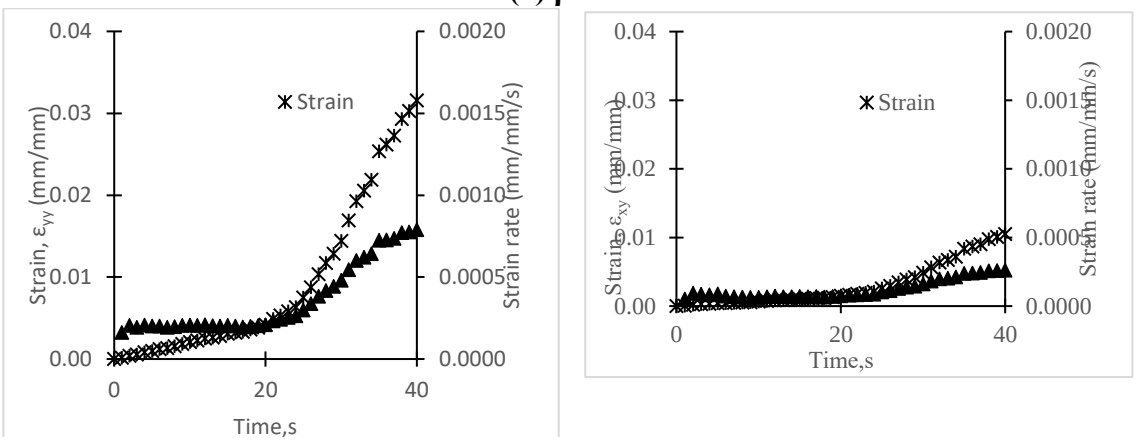

(b) β = 0.234

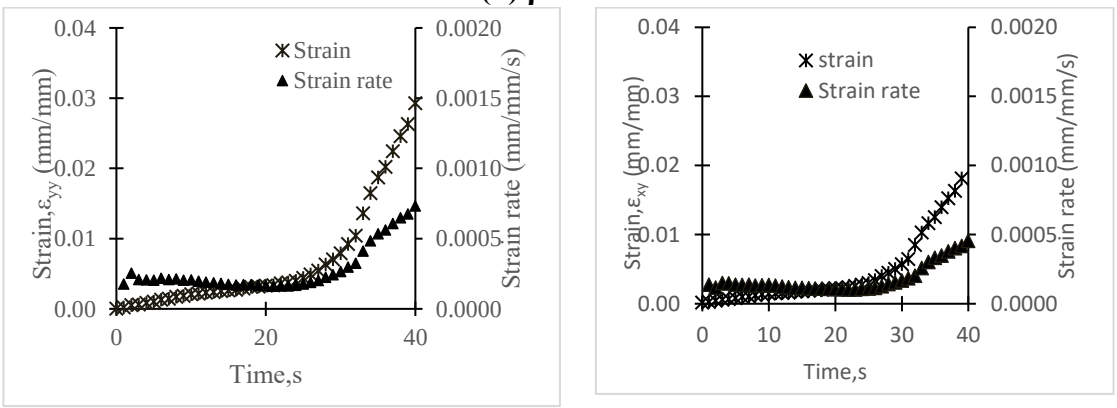

(c) β = 0.468

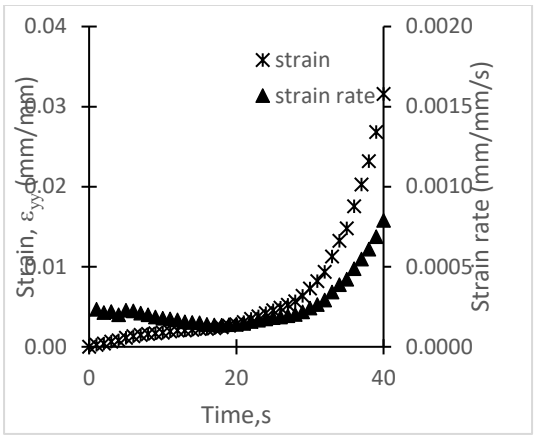

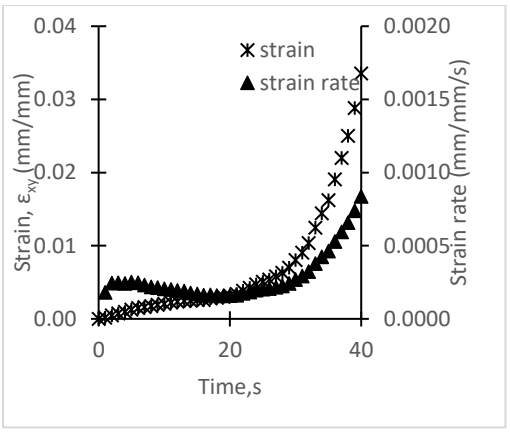

(d) β = 0.936

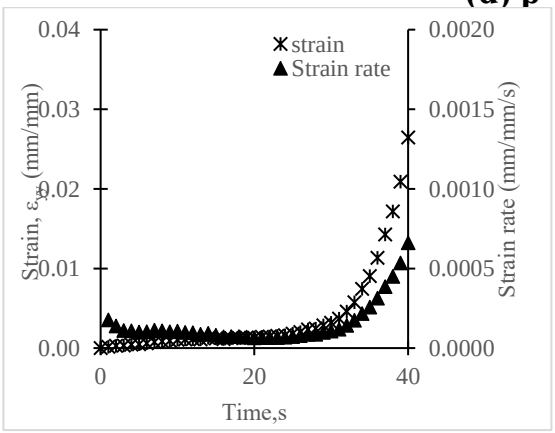

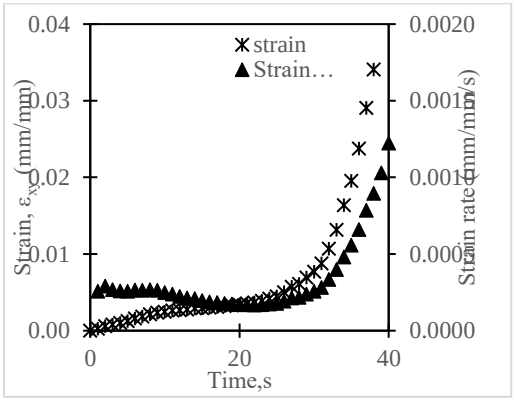

(e) β = 1.872

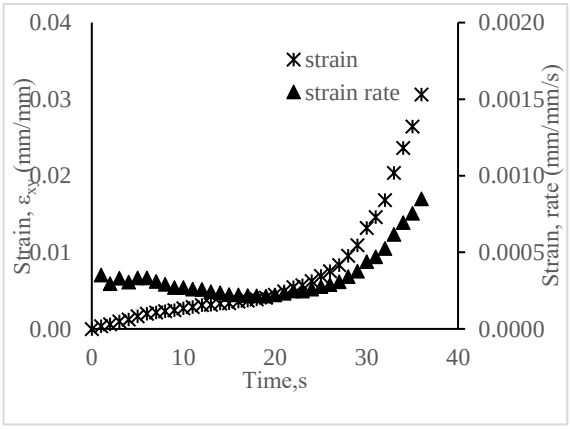

(f) β = ∞

Figure 4.24 Strain and strain rate vs. time for tubular specimens subjected to (a) uniaxial tension, β = 0, (b) tension-torsion, β = 0.234, (c) tension-torsion, β = 0.468, (d) tension-torsion, β = 0.936, (e) tension-torsion, β = 1.872, (f) torsion, β = ∞

The LDD specimens were uniaxially loaded in the table-top MTS system shown in Fig. 4.6 with an MTS extensometer attached to the gauge section for axial strain measurements. An expanded view of the entire experimental setup for the uniaxial LDD tensile experimental test with the extensometer is presented in Fig. 4.27.

Table 4.9 Camera and lenses for Vic-3D stereo-microscope

Parameter#	CSI stereomicroscope
Test Type	Tension
Specimens	Dogbone specimens RDD0, RDD45, RDD90
Cameras	5 MP CMOS Point Grey cameras, 2448 X 2048 pixels^2 array, 3.45 µm pixel size
Lens Filter	Linear polarizer
Lighting	LED with linear polarizing film
Calibration	15×15 dot grid, 0.28 mm dot size, 70 stereo calibration image pairs
Lens distortion	10 stereo distortion image pairs
Subset size	31 × 31 pixels^2
Step size	11 pixels
Strain filter size	5 x 5 data points (area of 35 X 35 pixels^2)
Speckle pattern	Produced by applying thin coat of white paint, followed by sprinkling black paint using an airbrush system.
Field of View	6.7 mm X 7.5 mm
Speckle size	Average size of 13µm

Table 4.10 Variability in strain measurements for RDD specimen

σ_{yy} (Mpa)	$(\varepsilon_{yy})_{mean}$ ($\mu\varepsilon$)	$(\varepsilon_{yy})_{var}$ ($\mu\varepsilon$)	$(\varepsilon_{yy})_{var}/(\varepsilon_{yy})_{mean}$	$(\varepsilon_{yy})_{var}$/NL
0 (No loading-NL)	50	50	-	-
43.76	834.00	76.70	0.09	1.53
88.49	1457.00	118.00	0.08	2.36
132.89	2056.00	152.00	0.07	3.04
177.10	2710.00	186.00	0.07	3.72
221.40	3422.00	211.00	0.06	4.22
264.34	5748.00	386.80	0.07	7.74
283.29	15810.00	936.00	0.06	18.72

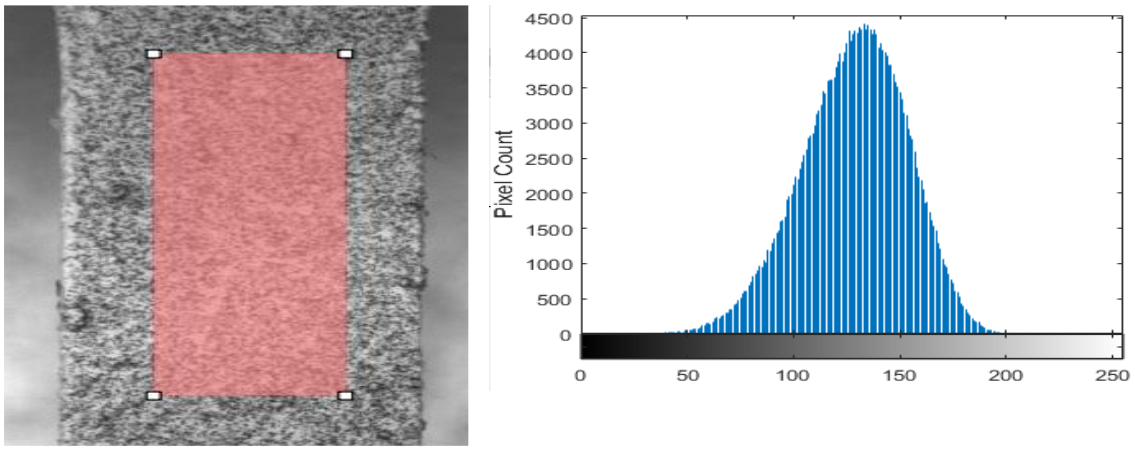

(a) (b)

Figure 4.25 Speckle Pattern on Dogbone (RDD) specimen with (a) 50 x200 pixel^2 region where strain data is analyzed and (b) grey level histogram for the pattern.

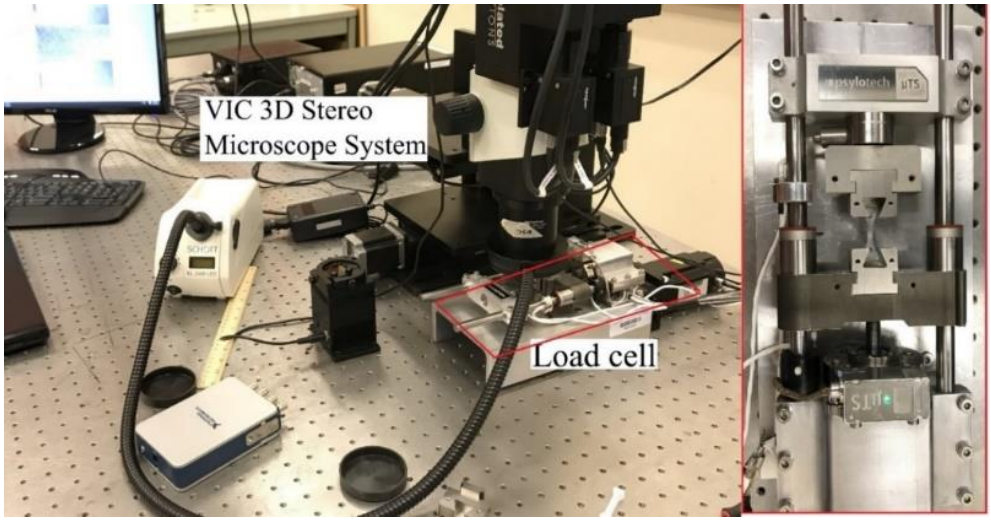

Figure 4.26 Experimental setup for uniaxial tension (RDD 0^0, 45^0, 90^0)test

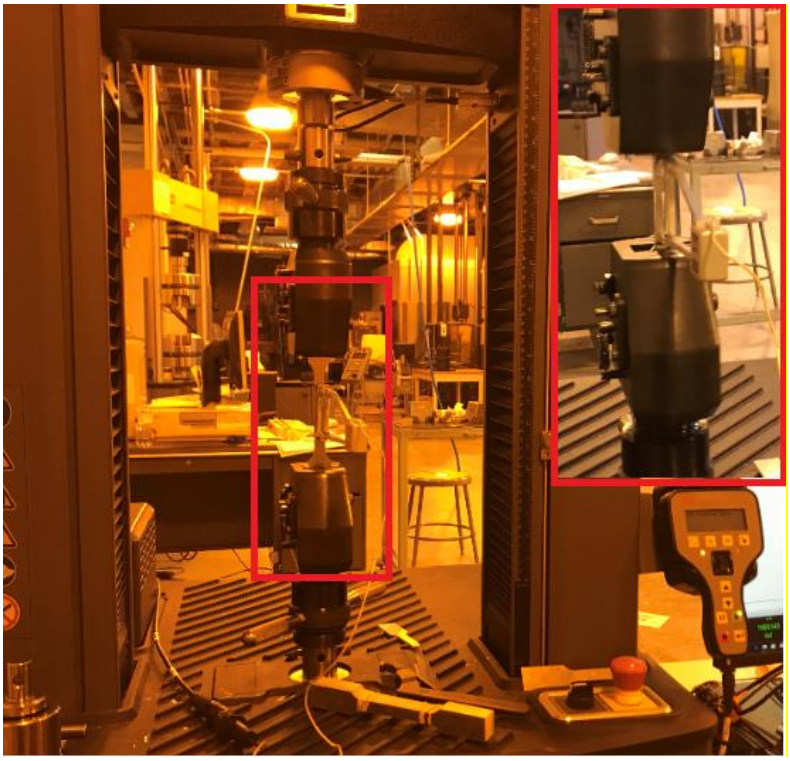

Figure 4.27 Experimental setup for uniaxial tension (LDD) test with an extensometer

CHAPTER 5

RESULTS

5.1 PARAMETER DETERMINATION

5.1.1 Anisotropic yield function parameter determination for MT1 and MT2 bar materials

Figs. 5.1 and 5.2 present true normal stress vs. true normal strain data for the uniaxial tension experiments (LDD, RDD0, RDD45, and RDD90 specimens) and shear stress vs. shear strain (γ) from torsion experiments (LDT specimens) for MT1 and MT2 materials, respectively. True normal stress and true normal strain are calculated using standard formulae:

$$\sigma = \sigma_{eng}\left(1 + \varepsilon_{eng}\right) \tag{5-1}$$

$$\varepsilon = ln(1 + \varepsilon_{eng}) \tag{5-2}$$

where ε and σ are true strain and stress, respectively and σ_{eng} and ε_{eng} are engineering stress and engineering strain, respectively. Since strains are less than 0.05 in these studies, Lagrangian strain measurements obtained by StereoDIC are excellent estimates for the engineering strains and hence are used in Eqs. 5.1 and 5.2 to determine the true strain.

A cursory inspection of the data in Figs. 5.1 and 5.2 indicate that the longitudinal extrusion process results in (a) circumferential symmetry in the material response for both MT1 and MT2 specimens, (b) a 20% increase in tensile yield stress for the MT2 LDD specimen, and

(c) a reduction in shear yield by 12% for the MT2 specimens. The measured increase in tensile yield stress is consistent with manufacturer data shown in Table 4.1. Interestingly, the radial tensile results for both MT1 and MT2 specimens are quite similar.

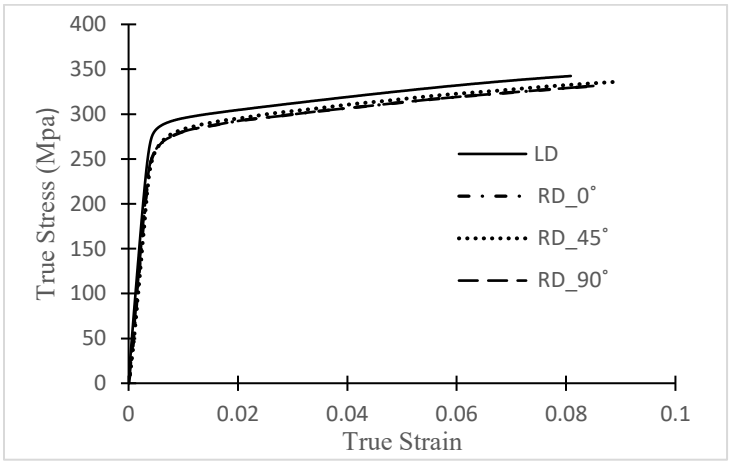

(a)

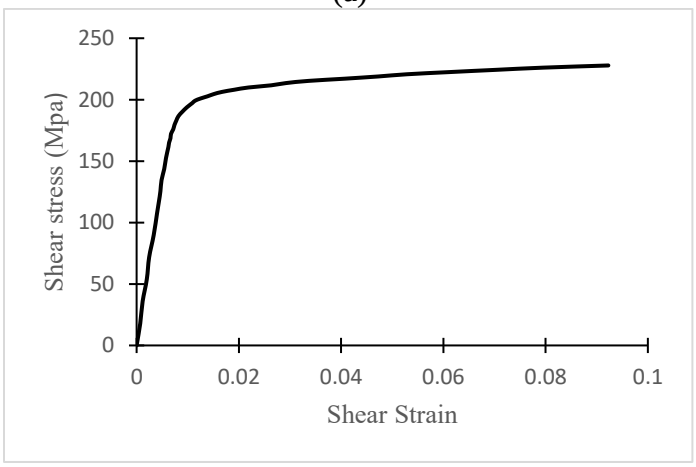

(b)

Figure 5.1 MT1 specimen results for (a) true stress vs. true strain measurements for tension loading of the LDD, RDD0, RDD45, and RDD90 specimens and (b) shear stress vs shear strain for torsion of LDT specimens.

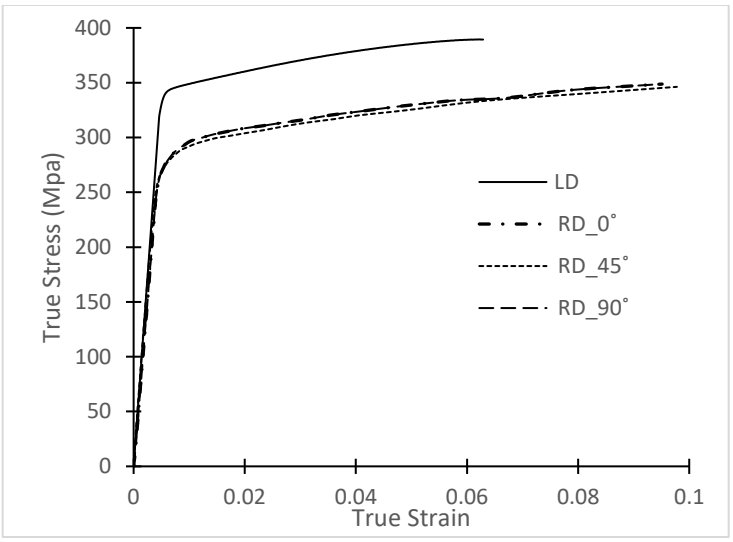

(a)

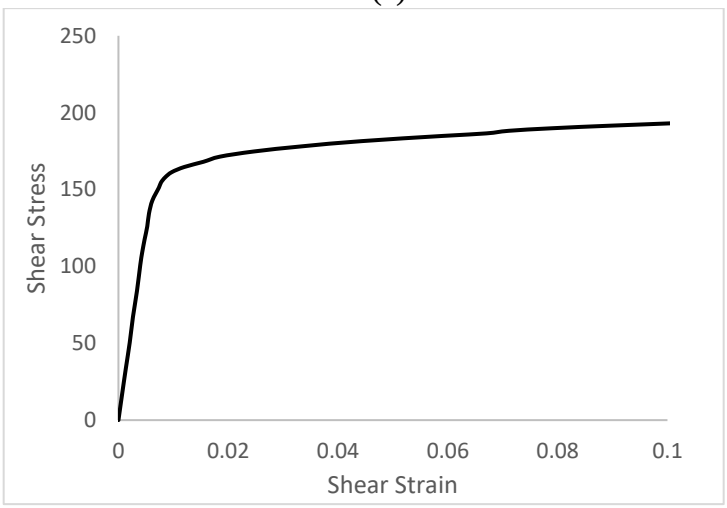

(b)

Figure 5.2 MT2 specimen results for (a) true stress vs. true strain measurements for tension loading of the LDD, RDD0, RDD45, and RDD90 specimens and (b) shear stress vs. shear strain for torsion of LDT specimens.

The Barlat Yld91 six parameter anisotropic yield function was selected as the calibration yield function in this dissertation. There were two reasons for selecting this yield function. The first reason is that for the relatively small outer diameter bars (d_o = 28.575 mm) of the original bars, there are limited options to extract usable specimens in a different direction for material characterization. The other reason is that the original bars' longitudinal extrusion process results in similar material responses in all circumferential

directions. Since the yield stresses in three orthogonal orientations for MT1 and MT2 extrusions can be determined using the tensile data from the LDD, RDD0, and RDD90 experiments, then three of the six anisotropic coefficients in Eq. (3-25) are obtained from the three uniaxial stresses at yielding in the directions of the orthotropic symmetry axes X, Y and Z in Fig. 4.2 using a Newton-Raphson numerical procedure to solve the non-linear set of equations. Specifically, a, b, and c in Eq. (3-25) are computed using the yield stresses determined experimentally from RDD0, RDD90, and LDD data, with the LDD measurements and the associated effective stress ($\bar{\sigma}$), considered to be the "reference" stress state. The other three coefficients are derived from the stresses at yielding for the LDT and RDD45 specimens. The parameter, g, is obtained using (a) the estimated a, b and c parameters, (b) the plane stress transformation equations for the Z-X plane with $\phi = -45^{o}$ to relate the applied axial stress in the rotated specimen to the stresses in the X-Y-Z coordinate system and (c) Eq. 3-25 to define a single equation for g. Finally, to determine the parameters f and h using the LDT specimen torsion data, the authors assumed that the yield stress in a specimen subjected to shear stress in either the X-Y plane or the Y-Z plane would be equal so that f = h. The six yield function parameters for the two 28.575mm diameters extruded Al 6061-rods are shown in Table 5.1.

Table 5.1 Parameters for the anisotropic yield function for d_o = 28.575 mm Al6061-T6 longitudinally extruded bars

Al6061-T6	m	a	b	c	f	g	h
MT1	8	1.0000	1.1571	1.000	0.8771	1.0835	0.8771
MT2	8	1.0000	1.4452	1.000	1.2069	1.3059	1.2069

Fig. 5.3 presents a comparison of the Barlat Yld91 anisotropic yield function predictions and the von Mises isotropic yield function predictions for the case of biaxial loading in the X-Y plane (which corresponds to loading and deformation in the Y-θ plane for the longitudinally extruded material) of MT1 and MT2. Fig. 5.4 presents similar comparisons for torsion-tension states of stress in the MT1 material system. Also shown in Figs. 5.3 and 5.4 are the two experimental data points for uniaxial tension loading (MT1 & MT2), and the six torsion-tension experimental data points (MT1). As shown in Figs. 5.3 and 5.4, theoretical predictions indicate that the von Mises criterion will overpredict the yield stress relative to the Yld91 for a biaxial stress state and underpredict the yield stress for a torsion-tension stress state in the X-Y plane, with the maximum difference of ~ 17%. For a biaxial stress state, the maximum difference is predicted for stress states where σ_{XX} is the largest. For a torsion-tension state of stress, the largest difference is predicted to occur when σ_{XY} is the dominant stress.

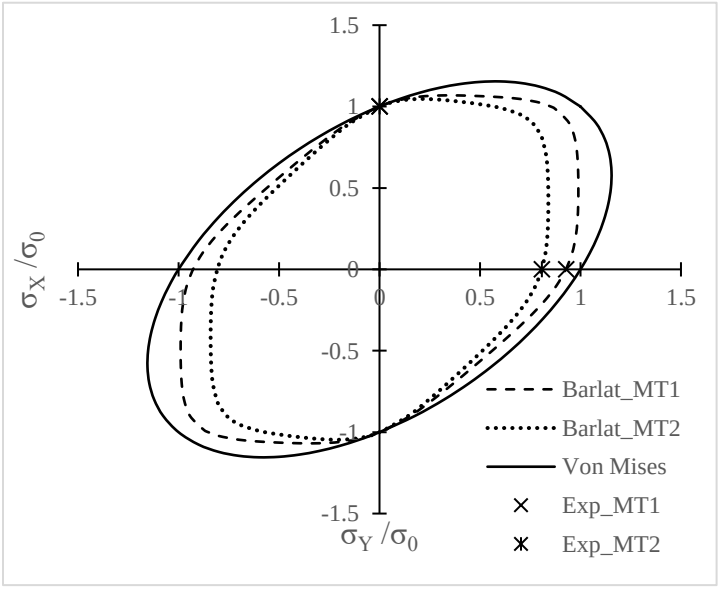

Figure 5.3 Predicted normalized yield surfaces for biaxial stress states with Barlat and Von Mises yield function for MT1 and MT2 bars.

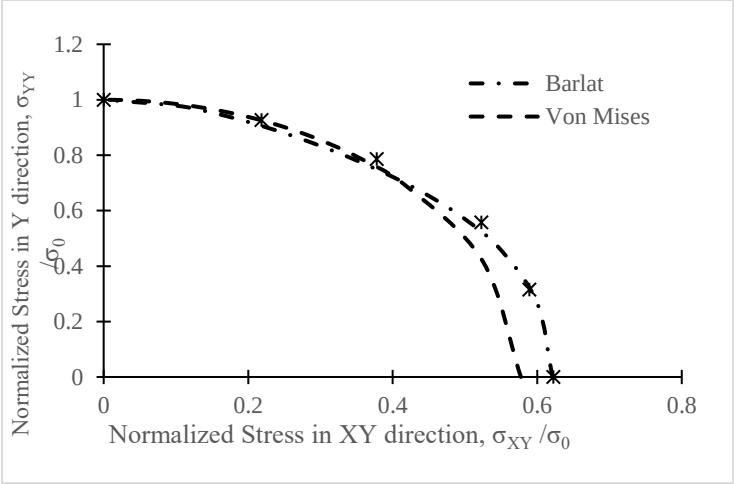

Figure 5.4 The normalized yield surfaces with Barlat and Von Mises yield function for Al 6061-T6 bar tension torsion yield surfaces.

5.1.2 Modulus of Elasticity, Poisson's ratio, and hardening parameter determination

The Modulus of Elasticity and Poisson's ratio are determined from the uniaxial tension experiment using Eq. (3-1) and (3-4), respectively, with data from the RDD0 specimen. The Moduli of Elasticity and Poisson's ratios for the MT1 and MT2 extruded Al 6061-T6 bars are presented in Table 5.2. The hardening parameter was determined from the uniaxial tension data obtained from LDD experiments and is shown in Table 5.2 for both materials. In addition to that, the comparable true stress vs. true strain data for the MT1 and MT2 Al6061-T6 bars is shown Fig. 5.5.

The most commonly used expression for strain hardening is the simple power law. The true strain and true stress relation can be express as

$$\sigma = K(\varepsilon)^n \tag{5-3}$$

where *K* is a material constant and *n* is the corresponding strain hardening parameter and strain hardening exponent, respectively.

Taking logarithms of both sides of Eq. (5-3) gives

$$log\sigma = nlog\varepsilon + logK \tag{5-4}$$

Eq. (5-4) is the equation of a straight line with n as the slope and log K as the intercept. The hardening parameters and hardening exponents for the MT1 and MT2 Al6061-T6 bars are shown in Table 5.2

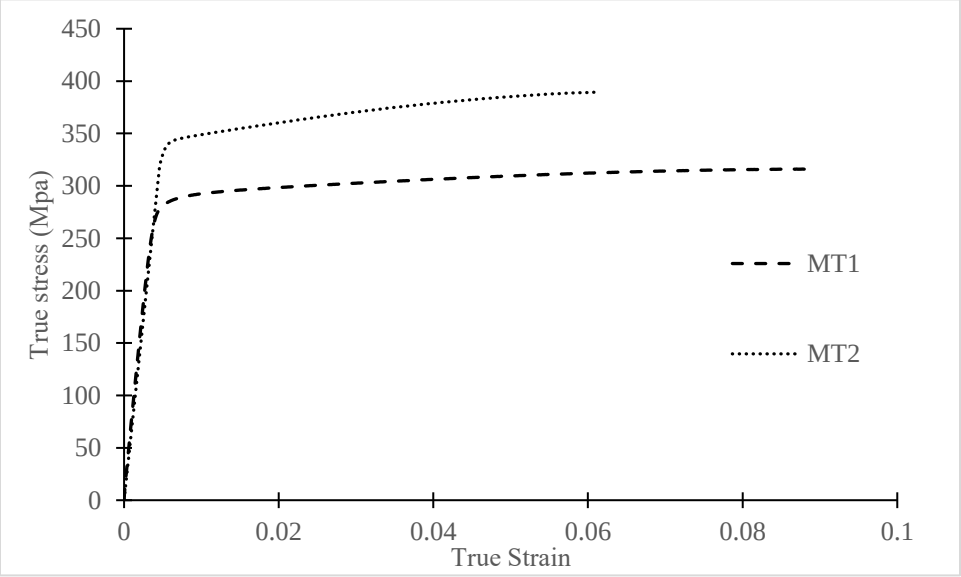

Figure 5.5 True stress vs. true strain curve from uniaxial tension LDD experiment for two Al6061-T6 bar

Table 5.2 Material and Hardening properties for predictive models

Material Properties	6061-T6 Al Tube (MT1)	6061-T6 Al Tube (MT2)
Modulus of Elasticity	69Gpa	69Gpa
Poisson's ratio	0.33	0.33
Hardening Parameter, n	0.0743	0.0607
Hardening Parameter, N=$\frac{1}{n}$	13.51	16.47
K	410Mpa	460Mpa

5.2 EXPERIMENTAL RESULTS OF UNIAXIAL TENSION, COMBINED TENSION TORSION, AND SIMPLE TORSION USING ISOTROPIC YIELD FUNCTION

As detailed in Chapter 4, a series of uniaxial tension, combined tension torsion, and simple torsion experiments were performed using the LDT sample machined from the MT1 extruded bar. A plot of effective stress, $\bar{\bar{\sigma}}$ vs. equivalent strain, $\bar{\bar{\varepsilon}}$ using the von Mises effective stress for tension, torsion, and several combinations of tension-torsion loading of the LDT specimens is given in Fig. 5.6. Section 5.4 outlines the comparison between Barlat and von Mises effective stress, $\bar{\bar{\sigma}}$ vs. equivalent strain, $\bar{\bar{\varepsilon}}$. The von Mises effective stress, $\bar{\sigma}_{VM}$, is determined from Eq. (3-17). The increments in plastic work/dissipation (dW^p) in terms of increments in equivalent plastic ($d\bar{\bar{\varepsilon}}^p$) strain are employed to define effective stress, ($\bar{\bar{\sigma}}$). Multiaxial stress states connect to the uniaxial experimental results in the following way;

$$dW^p = \bar{\bar{\sigma}}.d\bar{\bar{\varepsilon}}^p = \sigma_{ij}.d\varepsilon_{ij}^p \tag{5-5}$$

Using $\bar{\bar{\sigma}}$ and $\bar{\bar{\varepsilon}}$ to represent either the von Mises effective stress and effective strain variables or the Barlat effective stress and effective strain variables;

$$dW^p = \bar{\sigma}_{VM}.d\bar{\varepsilon}^p{}_{VM} = \sigma_{ij}.d\varepsilon_{ij}^p$$

$$dW^p = \bar{\sigma}_B.d\bar{\varepsilon}^p{}_B = \sigma_{ij}.d\varepsilon_{ij}^p$$

The Barlat effective stress, $\bar{\sigma}_B$, is determined from Eq. (3-25)

For combined torsion-tension experiments, we can write;

$$d\bar{\bar{\varepsilon}}^p = \frac{\sigma_{ij}.d\varepsilon_{ij}^p}{\bar{\bar{\sigma}}} = \frac{\sigma_{XX}.d\varepsilon_{XX}^p + 2\sigma_{XY}.d\varepsilon_{XY}^p + \sigma_{YY}.d\varepsilon_{YY}^p + \sigma_{ZZ}.d\varepsilon_{ZZ}^p}{\bar{\bar{\sigma}}} \tag{5-6}$$

If the elastic components of the strain increments are again neglected

$$d\bar{\bar{\varepsilon}} = \frac{\sigma_{ij} d\varepsilon_{ij}}{\bar{\bar{\sigma}}} = \frac{\sigma_{XX} d\varepsilon_{XX} + 2\sigma_{XY} d\varepsilon_{XY} + \sigma_{YY} d\varepsilon_{YY} + \sigma_{ZZ} d\varepsilon_{ZZ}}{\bar{\bar{\sigma}}} \quad (5\text{-}7)$$

Based on finite element results for a thin-walled cylinder (d_i = 16mm, d_o =18.54 mm, wall thickness, t = 1.27mm and length l = 24.25mm) under a uniaxial tension load of 15,000N, the stresses σ_{xx} and σ_{zz} are negligible. Thus, Eq. (5-7) can be further simplified with $\sigma_{xx} = 0$ and $\sigma_{zz} = 0$, to give

$$d\bar{\bar{\varepsilon}} = \frac{\sigma_{ij} d\varepsilon_{ij}}{\bar{\bar{\sigma}}} = \frac{2\sigma_{XY} d\varepsilon_{XY} + \sigma_{YY} d\varepsilon_{YY}}{\bar{\bar{\sigma}}} \quad (5\text{-}8)$$

Finally, the total effective strain can be determined by integrating from the reference (r) to the current step (n),

$$\bar{\bar{\varepsilon}} = \int_r^n d\bar{\bar{\varepsilon}} = \sum_{r=1}^{n} d\bar{\bar{\varepsilon}} \quad (5\text{-}9)$$

As shown in Fig. 5.6, beyond the linear elastic regime, there is a significant difference between the various experimental results. This observation is inconsistent with the assumption of isotropic elastic-plastic stress-strain response where all loading combinations should coalesce into a single $\bar{\bar{\sigma}} vs\ \bar{\bar{\varepsilon}}$ response function. In particular, results clearly show an upward shift in initial yield response that is a monotonic function of $\beta = \frac{\sigma_{XY}}{\sigma_{YY}}$. According to effective stress vs. equivalent strain response presented in Fig. 5.6. the yield stress defined by the von Mises criterion varies with β by up to 14%.

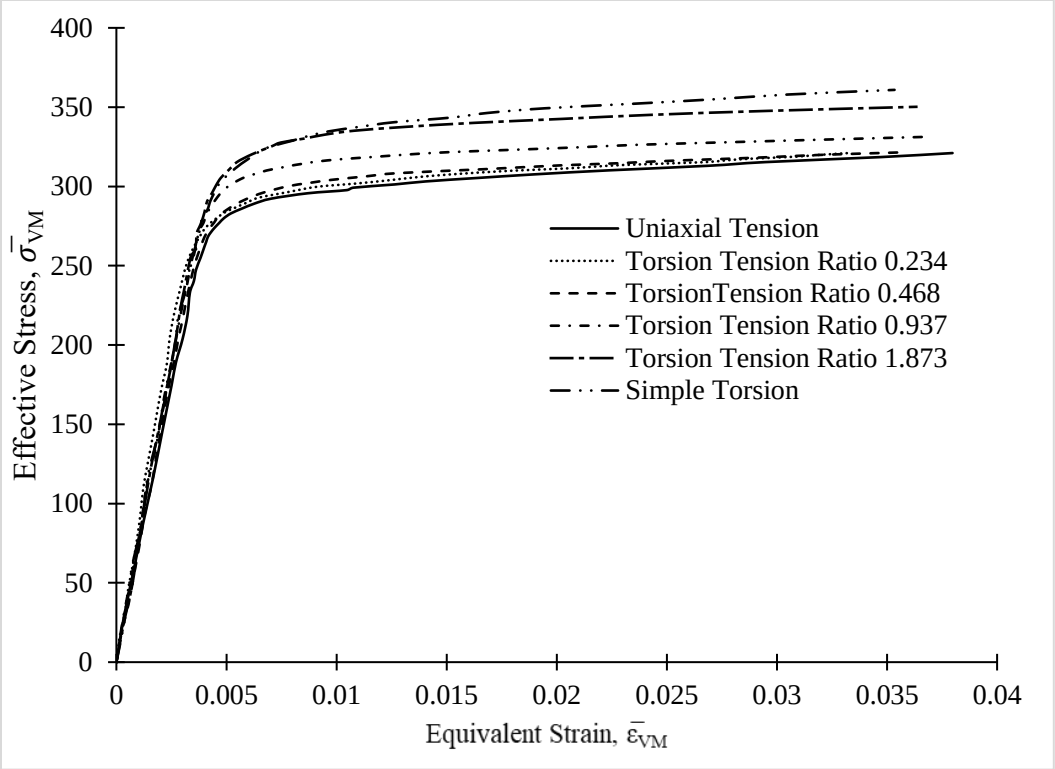

Figure 5.6 Comparison of von Mises effective stress vs. equivalent strain responses in LDT specimens extracted from the MT1 bar for a range of β parameters.

5.3 STRAIN RATIO FROM TORSION-TENSION EXPERIMENTS

The strain ratio ($\Gamma_\beta = \varepsilon_{xy} / \varepsilon_{yy}$) was derived from the slope of ε_{xy} and. ε_{yy} (true strain) measurements on the LDT specimen. A plot of ε_{xy} vs. ε_{yy} for several combinations of proportional torsion-tension loading using the LDT specimen is given in Fig. 5.7. The general trends shown in Fig. 5.7 indicate that proportional torsion-tension loading of the specimens results in approximately proportional torsion-tension straining, though the Γ_β data are between 10% to 40% higher than the corresponding β values, with the maximum difference occurring when the shear stresses are smallest.

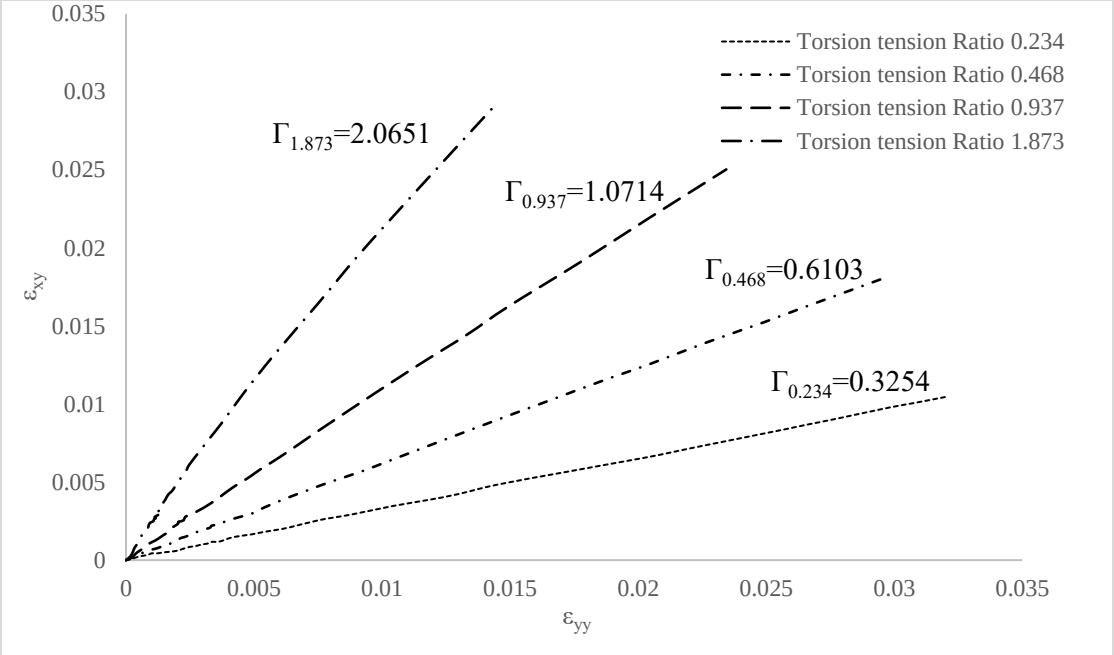

Figure 5.7 Measured ε_{xy} vs. ε_{yy} strains for the LDT specimen obtained during torsion-tension experiments for a range of β parameters

5.4 COMPARISON BETWEEN BARLAT AND MISES EFFECTIVE STRESS RESULTS

For β = 0.234, 0.468, 0.936, 1.872 and ∞, Figs. 5.8-5.12 compare the effective stress versus equivalent strain results for the MT1 material using the von Mises and Barlat anisotropic models. In general, the Barlat model is within +/- 4% of the uniaxial data for all tension-torsion ratios, β. The von Mises results overpredict the uniaxial results for all β, with the largest offset of +14% for simple torsion (β = ∞). As β decreases, the Von Mises representation becomes increasingly accurate, eventually matching the uniaxial results for tension loading. Detailed inspection of the Barlat Anisotropic results show that the model (a) slightly overpredicts the uniaxial results for β > 1, (b) slightly underpredicts the uniaxial results for 0.47 < β < 1 and (c) matches the uniaxial results when β = 1 and β < 0.47.

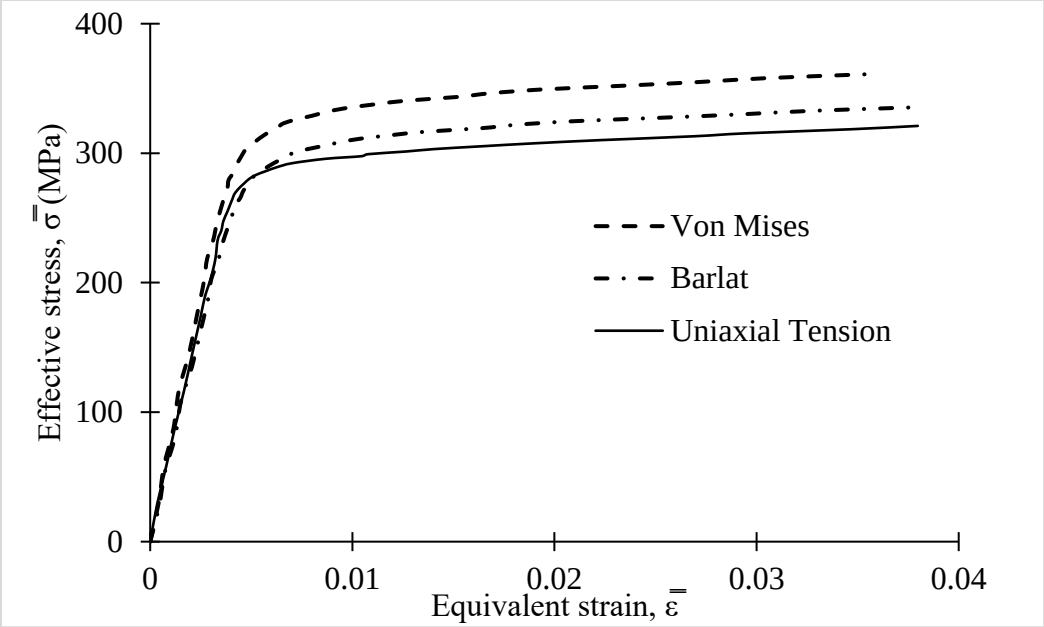

Figure 5.8 Comparison of Barlat, Von Mises, and uniaxial effective stress vs. effective strain results for simple torsion with $\beta = \infty$.

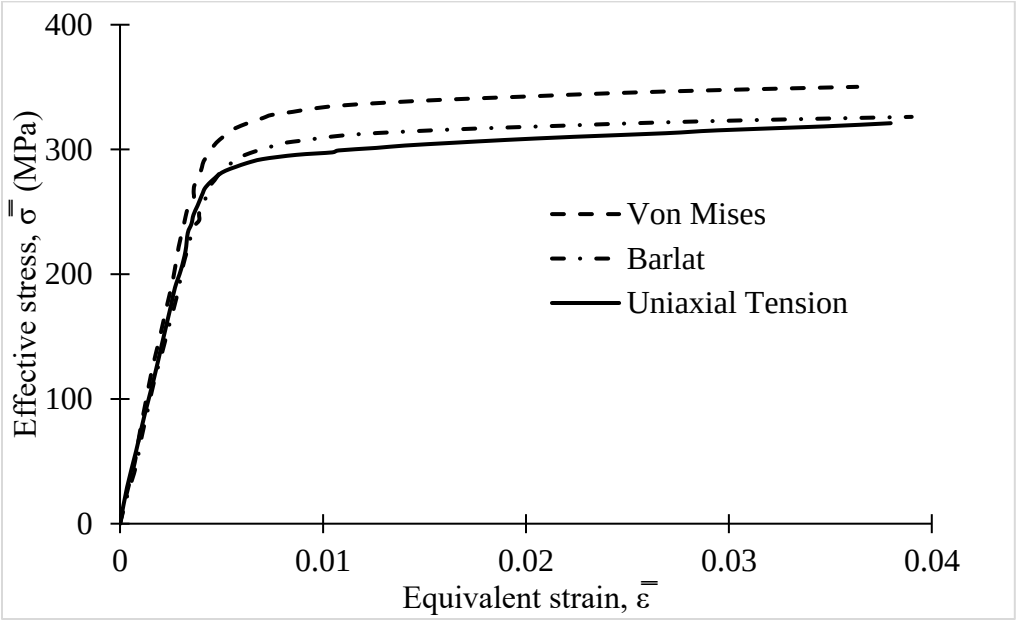

Figure 5.9 Comparison of Barlat, Von Mises, and uniaxial effective stress vs. effective strain results for combined tension and torsion, $\beta = 1.873$.

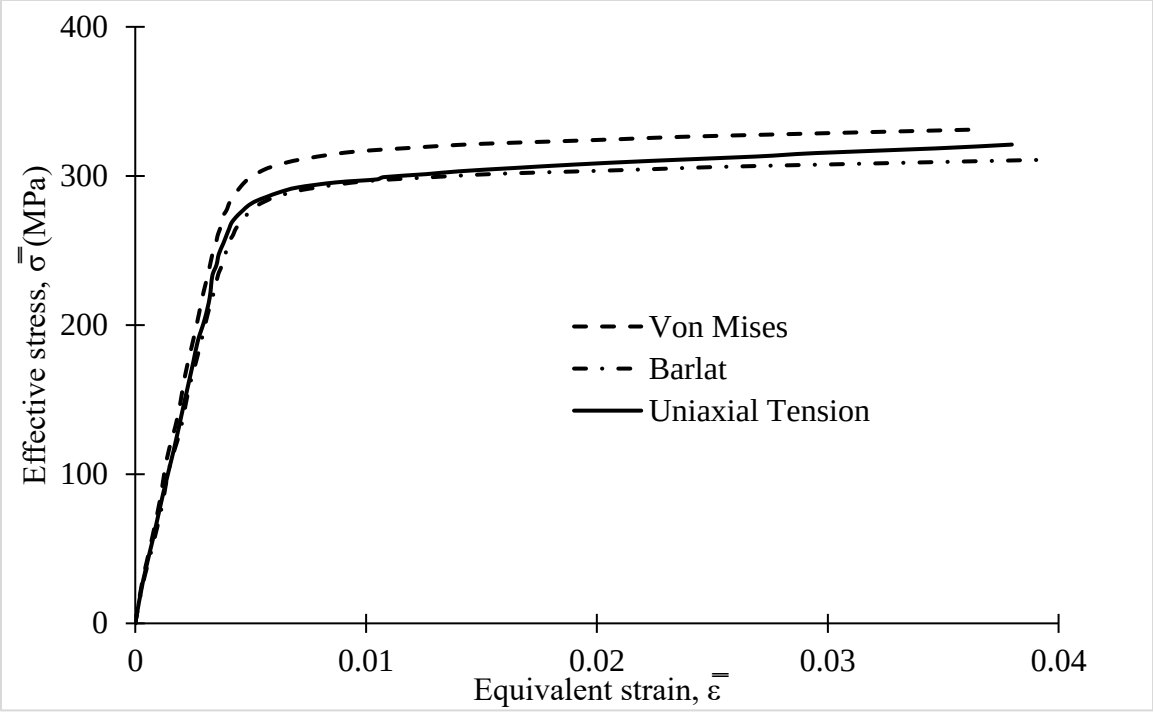

Figure 5.10 Comparison of Barlat, Von Mises, and uniaxial effective stress vs. effective strain results for combined tension and torsion, $\beta = 0.973$.

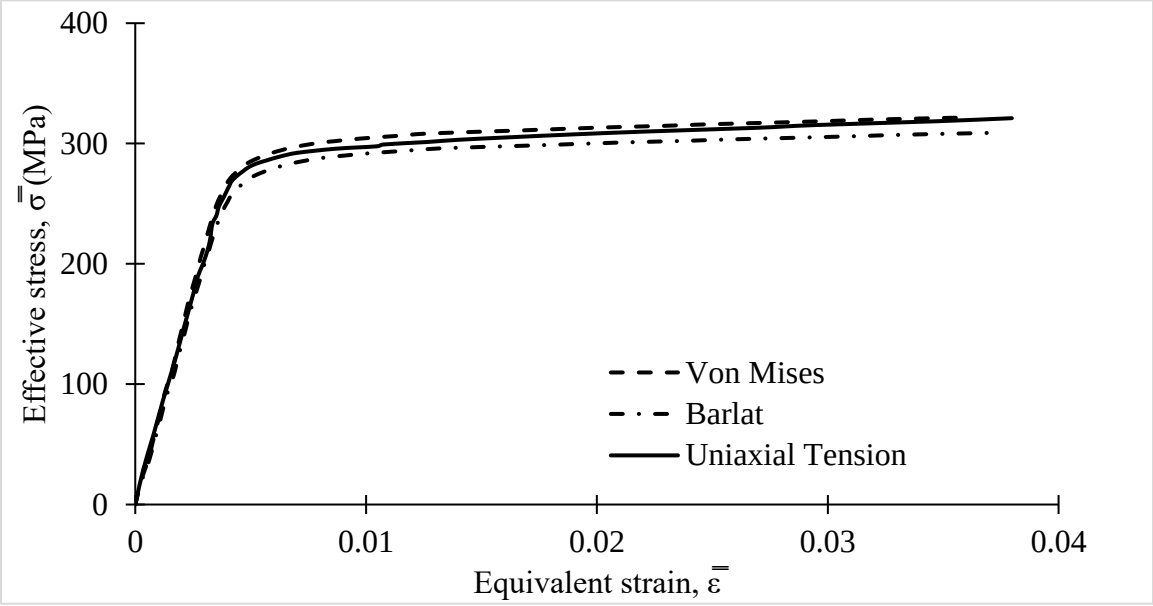

Figure 5.11 Comparison of Barlat, Von Mises, and uniaxial effective stress vs. effective strain results for combined tension and torsion, $\beta = 0.468$.

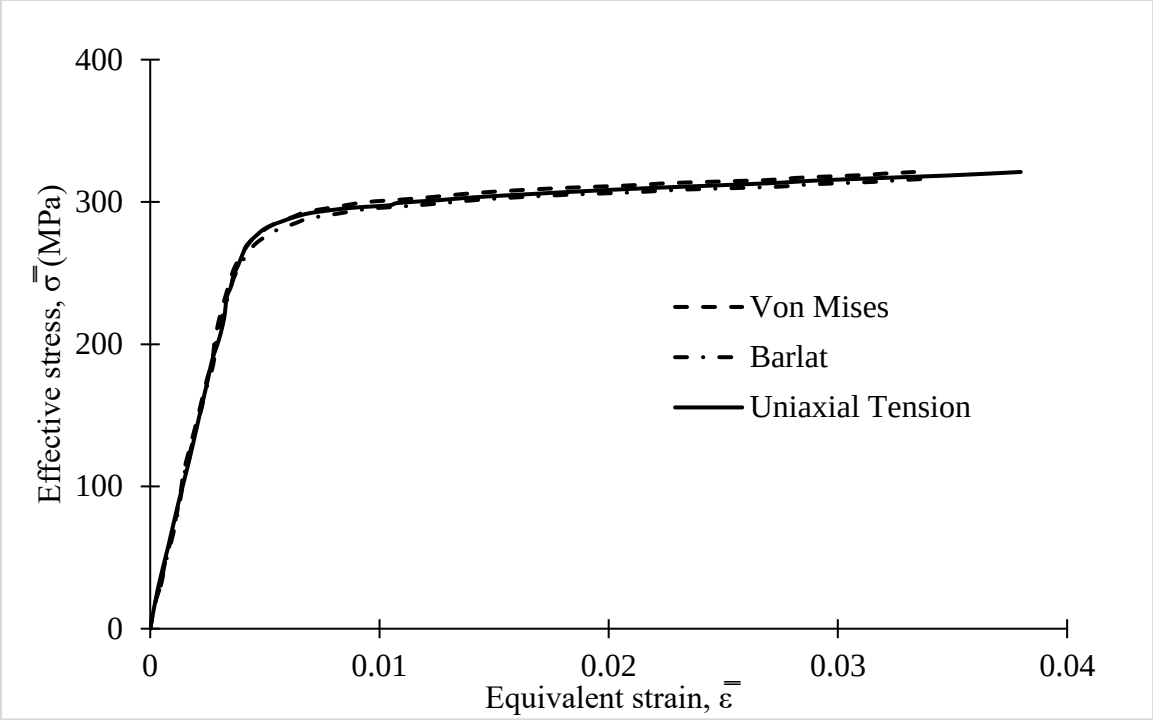

Figure 5.12 Comparison of Barlat, Von Mises, and uniaxial effective stress vs. effective strain results for combined tension and torsion, $\beta = 0.234$.

5.5 COMPARISON OF THEORETICAL AND EXPERIMENT TOTAL SHEAR STRAIN

Incremental plasticity is used to predict total strain for a torsion specimen subjected to known applied shear stress that is determined using input load cell data torque vs. time acquired from a simple torsion experiment. A flow chart for the numerical program used to implement the theoretical formulae and predict the elastic and plastic strains is shown in Fig. 5.13. The input load cell data is presented in Fig. 5.14. The accuracy of the predictions is assessed by direct comparison to the experimental measurements for the total shear strain on the specimen surface during torsional loading using the same loading path as shown in Fig. 14. Numerical predictions of the mechanical response of torsion specimens are obtained using both an isotropic yield criterion with von Mises effective stress Eq.(3-17) and the anisotropic Barlat Yld91 yield criterion in Eq. (3-25). Incremental equivalent

plastic strain ($d\bar{\varepsilon}^p$) is represented through the hardening power-law rule, as shown in Eq. (5.3). This equation can be simplified in the following way

$$\sigma(\bar{\varepsilon}^p) = \sigma_0(\frac{\varepsilon}{\varepsilon_0})^{\frac{1}{N}}$$

$$\frac{\partial \bar{\varepsilon}^p}{\partial \bar{\sigma}} = \frac{N(\frac{\sigma}{\sigma_0})^{N-1}-1}{E} \tag{5-10}$$

where, $\frac{1}{N} = n, and\ \ \sigma_0(\frac{1}{\varepsilon_0})^{\frac{1}{N}} = K,$

Figs. 5.15 and 5.16 present direct comparisons of the shear stress vs. shear strain results using experimental strain measurements and theoretical predictions using isotropic and anisotropic yield criteria for both MT1 and MT2 specimens, respectively.

5.6 EXPERIMENTAL RESULTS FOR NON-PROPORTIONAL LOADING PATHS

Two different non-proportional loading experiments were conducted in this work for the MT2 material system. During the first non-proportional loading experiments, the tube is twisted up to the yield point. Torsion is then halted, and tension load is applied, holding the angle of twist constant. Fig. 5.17 shows the applied experimental axial stress and shear stress with respect to time. The loading paths shown in Fig. 5.17, Fig. 5.18-5.20 present (a) experimental shear stress versus axial stress, (b) experimental total axial strain and axial plastic strain versus time, and (c) experimental total shear strain and shear plastic strain versus time, respectively.

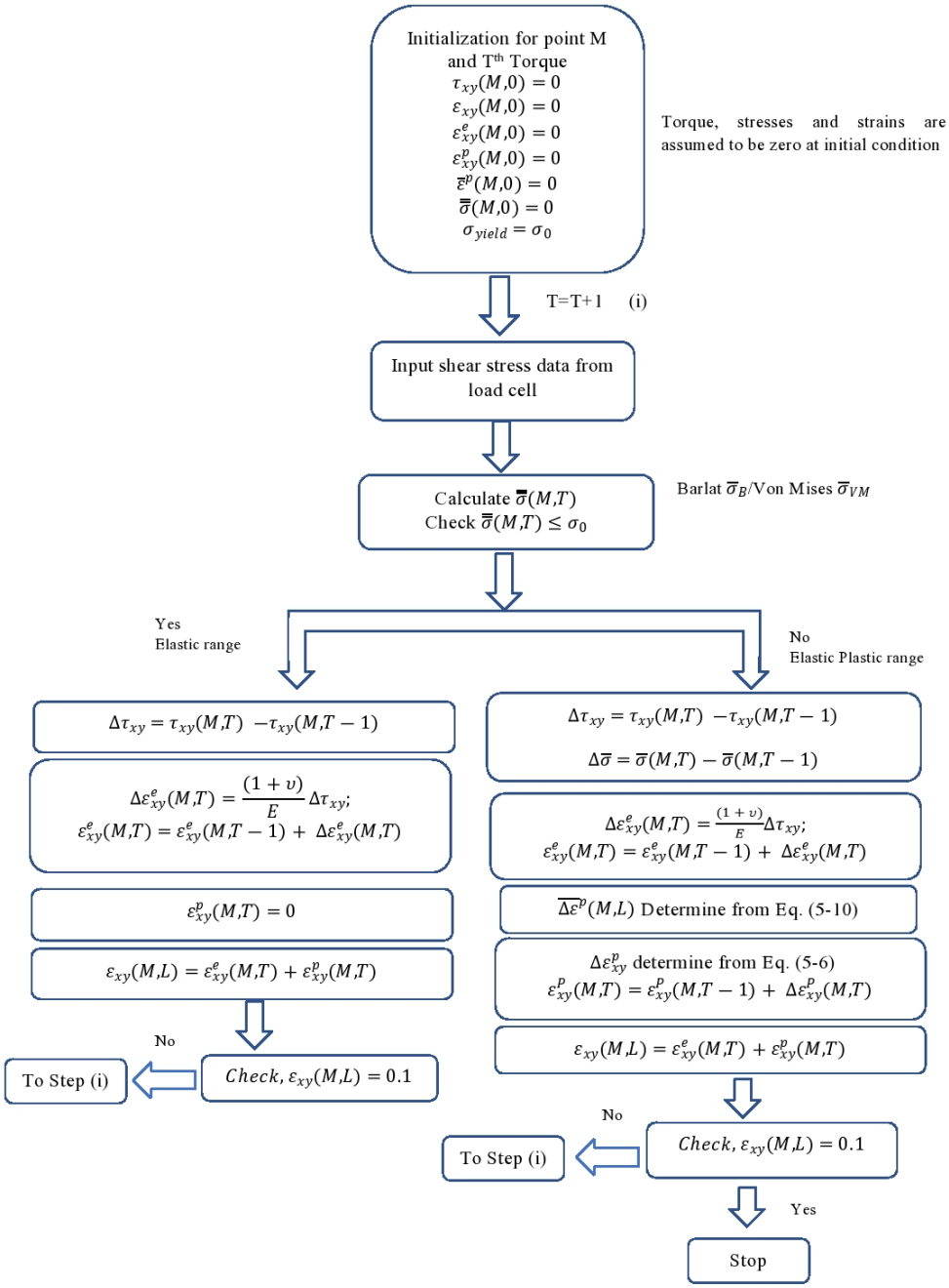

Figure 5.13 Flow chart for numerical program implementing theoretical formulae and predicting the elastic and plastic strains

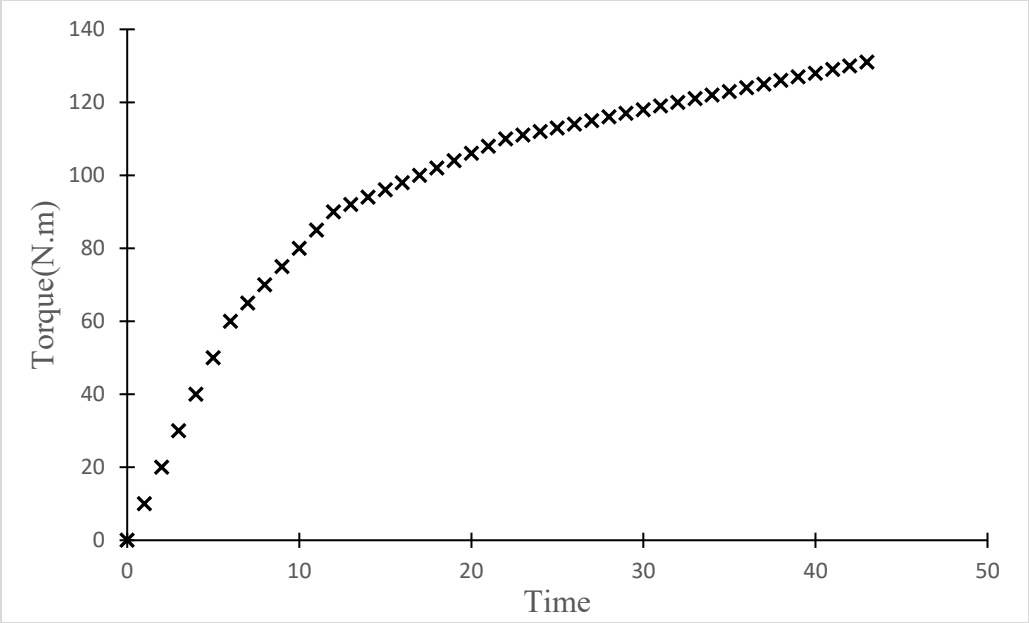

Figure 5.14 Torque vs time data acquired from electromechanical load cell during simple torsion experiments

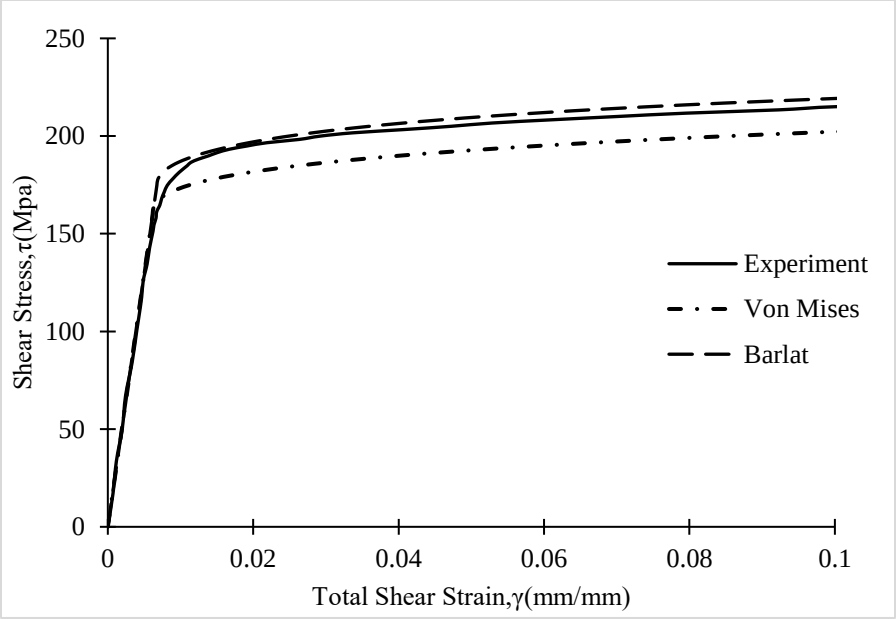

Figure 5.15 Experimental and theoretical shear stress vs shear strain comparisons for Al6061-T6 MT1 extrusion.

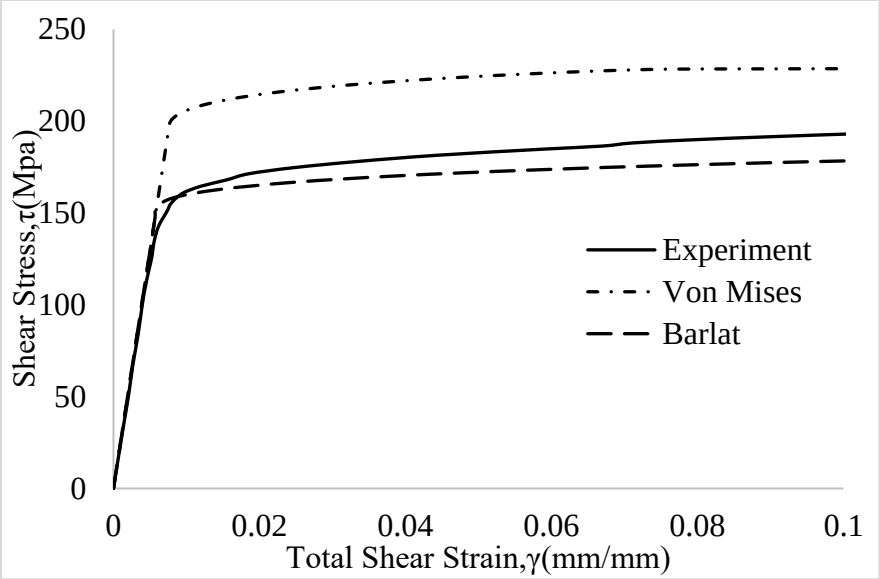

Figure 5.16 Experimental and Theoretical Shear stress vs shear strain curve comparison for Al6061-T6, MT2 extrusion

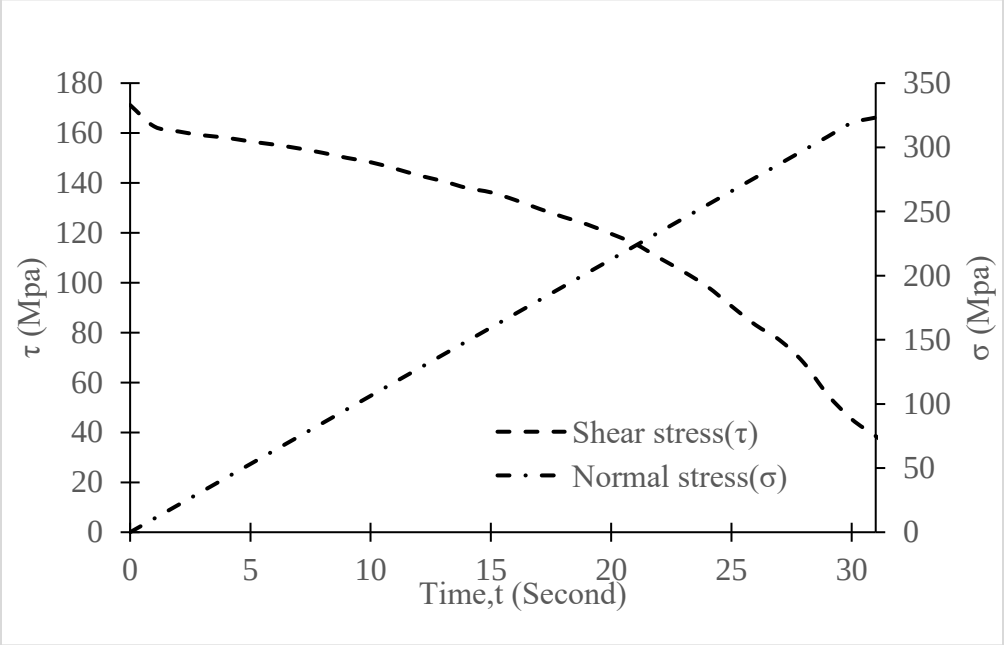

Figure 5.17 Experimental axial stress and shear stress versus time for non-proportional (Tension after torsion) loading

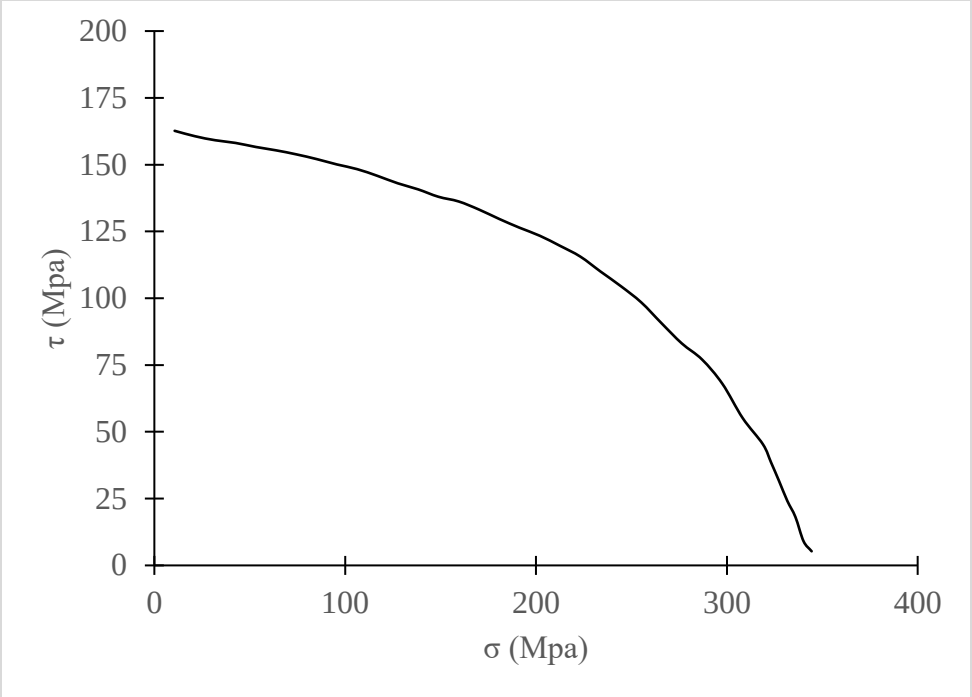

Figure 5.18 Experimental shear stress versus axial stress for non-proportional (Tension after torsion) loading

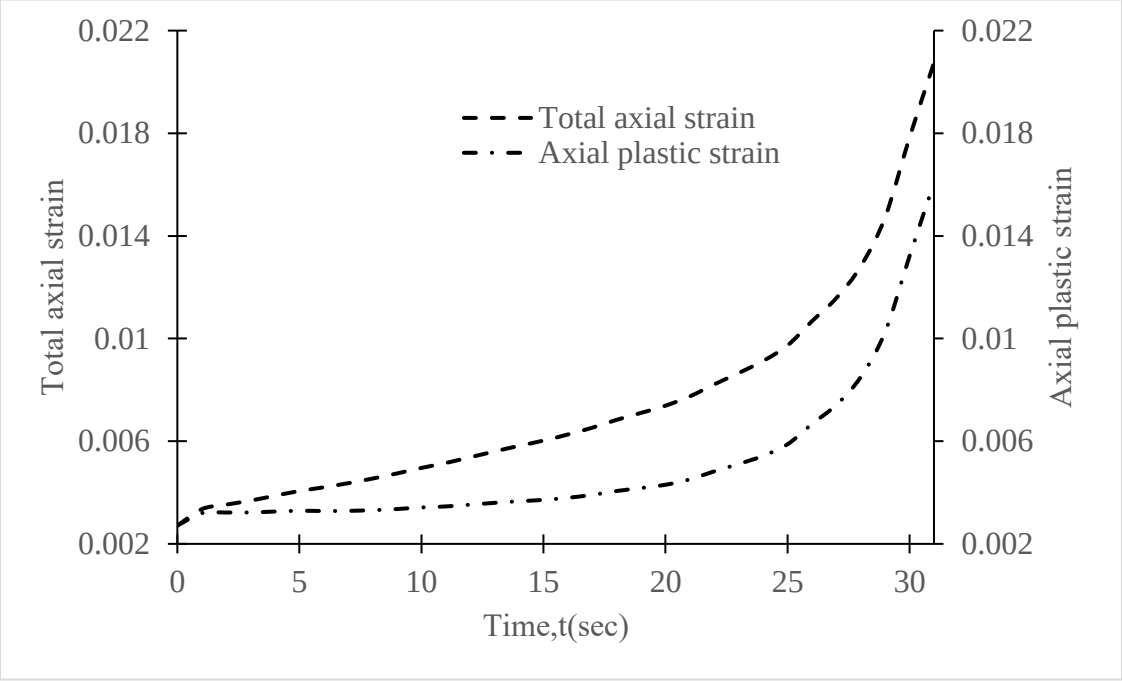

Figure 5.19 Experimental total axial strain and the axial plastic strain versus time for non-proportional (tension after torsion) loading

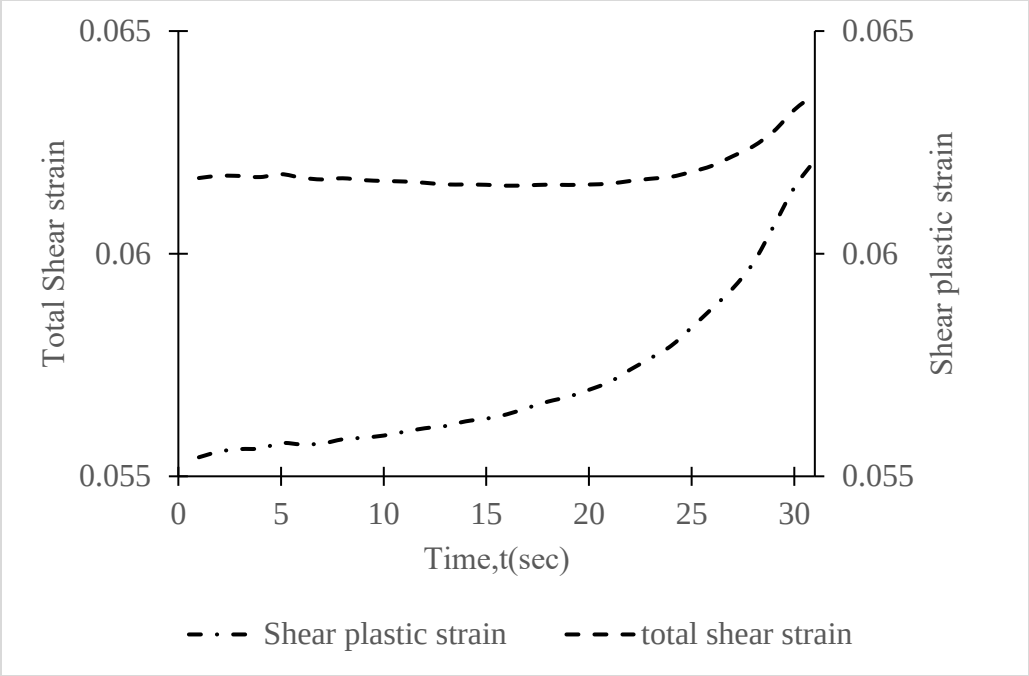

Figure 5.20 Experimental total shear strain and shear plastic strain versus time for non-proportional (tension after torsion) loading

During the second non-proportional experiment, the tube is loaded to the yield point in tension while holding the axial displacement constant, then torsion load is applied. Fig. 5.21 shows the applied axial stress and shear stress with respect to time. Figs. 5.22 -5.24 presents (sa) experimental shear stress versus axial stress, (b) experimental total axial strain and the axial plastic strain versus time, and (c) the experimental total shear strain and shear plastic strain versus time, respectively.

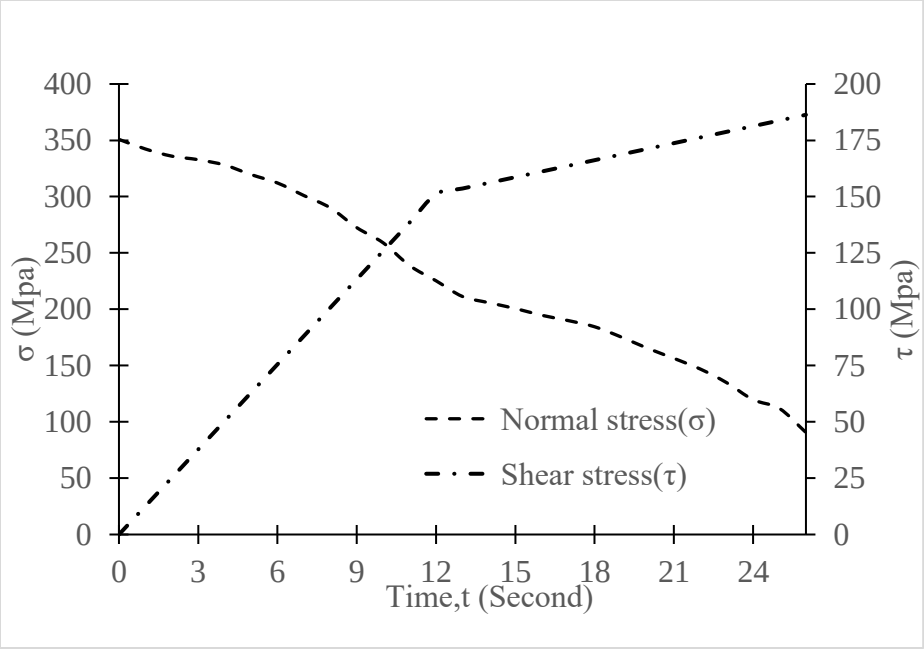

Figure 5.21 The axial stress and the shear stress versus time for non-proportional (Torsion after tension) loading

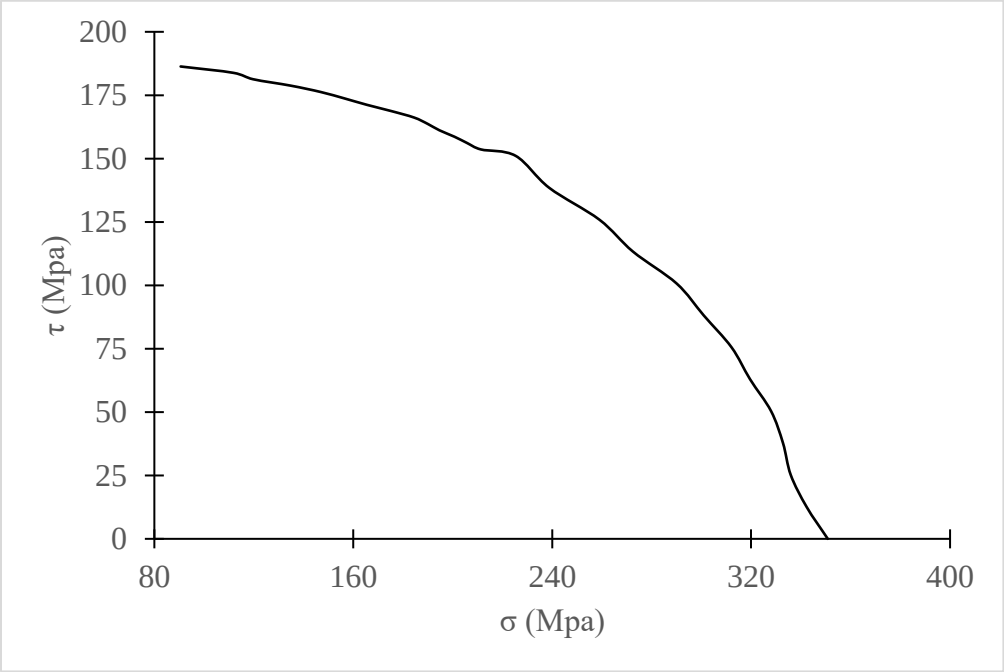

Figure 5.22 The shear stress versus the axial stress for non-proportional (Torsion after tension) loading

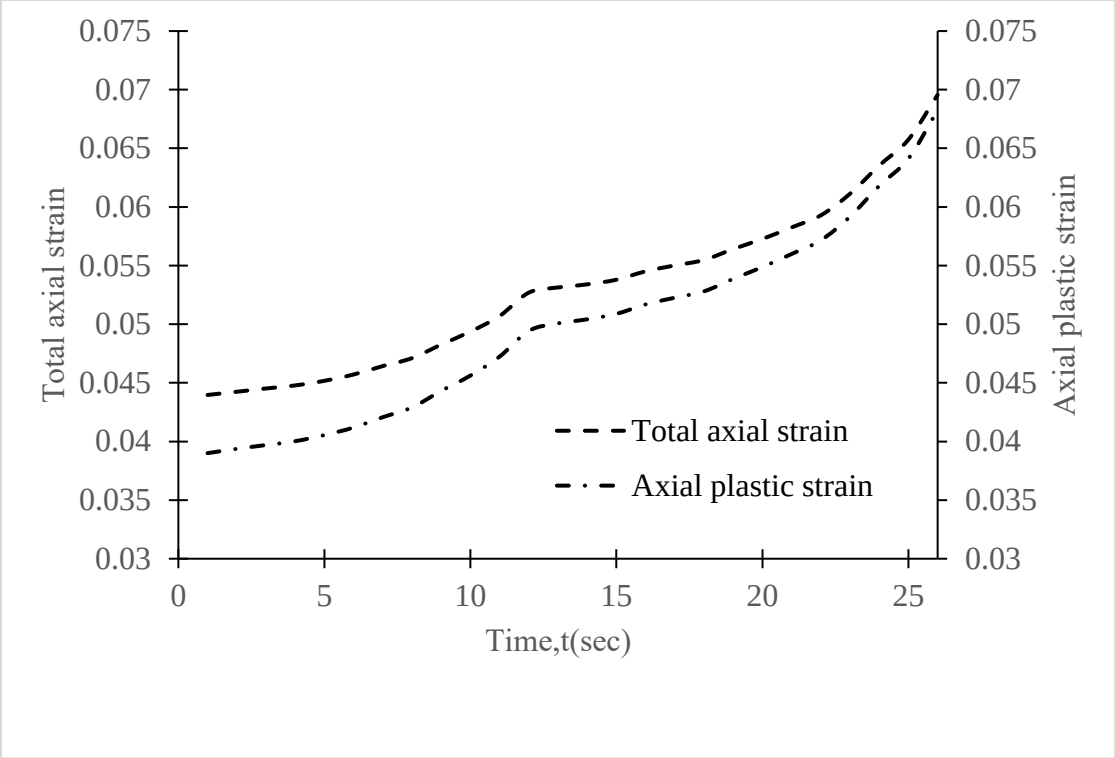

Figure 5.23 The total axial strain and the axial plastic strain versus time for non-proportional (Torsion after tension) loading

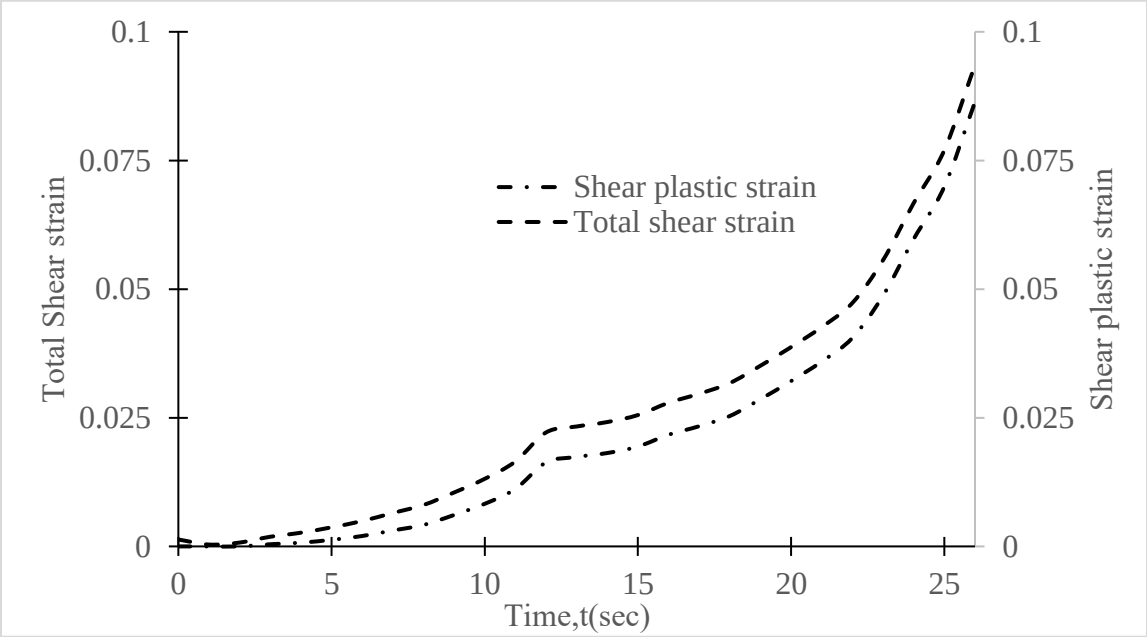

Figure 5.24 The total shear strain and the shear plastic strain versus time for non-proportional (Torsion after tension) loading

CHAPTER 6

DISCUSSION

Manufacturing the thin-walled cylindrical specimens shown in Fig. 4.4 was not a simple process. Initial attempts using generally accepted machining practices to bore a concentric central hole over a 144.78 mm length resulted in non-concentric boring and oscillations in thickness that was unacceptable for our experiments. Through several iterations and purchase of stable, lathe-mounted boring bits, machining of the specimens was performed to standards exceeding those required for our experiments.

The unacceptability of the original machined specimens was first identified using StereoDIC to obtain full-field strain measurements. The full-field strain data clearly showed visible bands of strain oscillations along the gauge length, indicative of unwanted thickness changes due to machining. In addition, linear gradients were observed in the strain data that were later shown to be due to slight non-concentricity in specimen machining. It is noted that the investigators also used surface-mounted strain gauges during the early stages to identify manufacturing flaws but were unable to identify strain oscillations in the data. Based on these observations, the investigators always used the StereoDIC full-field strain data to identify unexpected anomalies due to machining, gripping, or loading problems, performing replacement experiments when strain field anomalies were seen.

Regarding the various specimen types extracted from the original rod, it is noted that the authors did not specifically determine whether material directions changed across the reduced width for the limited number of LDD specimens. The authors have shown that the stress-strain response of the LDD specimens extracted from different locations along the length are nearly identical, indicating that axial homogeneity in the LDD response is a reasonable assumption that is justified by the limited data obtained in this study. Though not shown in the dissertation, the tensile results from the LDT specimens that have the material in the gauge section at different radial positions than the LDD specimens were nearly identical to the LDD true stress vs. true strain data, indicating that axial material response across the bar diameter does not change appreciably, an observation that is consistent with the assumption of axial homogeneity in the radial direction. Though the authors did not perform specific metallurgical analysis to quantify texture variations along the radial direction, micrographs across the radial direction were uniformly similar in appearance at several axial locations along the bar length, suggesting there is consistency in material structure.

The gripping specimen system shown in Figs 4.9 and 4.10 was developed successfully by the investigators so that alignment of the specimen was achievable on a consistent basis. Though physical displacement of the gripping system is small during mechanical loading, slight rotational and vertical slippage of the specimen was observed at high loads and measured by the StereoDIC system. However, since all experiments are performed in load and torque control, and the actual surface strain fields are measured using StereoDIC at each applied force/torque, these slight motions have no effect on the quality of the experimental data used in our study.

A cursory inspection of the data in Figs. 5.1 and 5.2 indicate the longitudinal extrusion process results in (a) circumferential symmetry in the material response for both MT1 and MT2 specimens, (b) greater than 20% increase in tensile yield stress for the MT2 specimen, and (c) a reduction in shear yield stress by 12% for the MT2 specimens. The measured increase in tensile yield stress is nominally consistent with manufacturer data shown in Table 4.1. Interestingly and consistent with (a) above, the radial tensile results for both MT1 and MT2 specimens are quite similar.

The effect of anisotropy in the behavior of both longitudinally extruded Al6061-T6 cylindrical tubes is evident in the values of the six Yld61 parameters in Table 5.1 for both MT1 and MT2 bars. Several of the parameters show significant deviation from unity, where unity is the value required for isotropic yielding. The deviation from isotropy evident in our anisotropic parameters for extrusion of aluminum tubes is generally consistent with the results obtained by Fjeldly and Roven,1996, Lademo et al.,1999, and Achani et al.,2009, providing a level of confidence in the as-computed Barlat anisotropic yield function.

Though there are slight changes in elemental composition shown in Table 4.1, the most likely source of the different material behavior for MT1 and MT2 specimens is the longitudinal extrusion process that resulted in significant changes in material microstructure shown in Fig. 4.1. As noted previously, the large difference in microstructure for MT1 and MT2 original bars (Fig.4.1) shows that the MT2 specimen has undergone much higher elongation and transverse compression than MT1 during the "nominally similar" extrusion processes. Such differences are consistent with the observed increase in work-hardening shown in Table 5.2 and the higher yield stress and higher ultimate stress shown in Table 4.1 for MT2 relative to MT1.

As shown in Fig. 5.3, the Barlat Yld91 predictions for tensile loading in the radial direction (X) and axial direction (Y) are in excellent agreement with the very limited experimental data (3 points), whereas the Von Mises yield criterion overpredicts the required yield stress for loading in the radial direction by up to 25%. The source of the relatively strong yield anisotropy is most evident in Fig. 5.2, where the true yield stress in radial directions for the MT2 material is ~ 25% lower than in the longitudinal direction (270 MPa vs 340 MPa). Furthermore, as shown in Fig. 5.3, the effect of yield anisotropy is largest for $\sigma_X/\sigma_Y \approx 0.5$, with the Barlat criteria predicting yielding for lower stresses (15 % lower for MT1, 30% for MT2) than the Von Mises criteria. Thus, the Barlat yield criteria provides substantially improved accuracy in the prediction of yielding for those applications where such differences are truly important. As shown in Fig. 5.4, the set of experimental data is in excellent agreement with the Barlat Yld91 predictions. As presented in Fig. 5.7, the proportional torsion-tension loading of the specimens results in approximately proportional torsion-tension straining with a deviation between 10% to 40%.

The von Mises effective stress vs. equivalent strain response presented in Fig 5.6 does not show a unique solution, an observation that is consistent with previous studies by Hecker, 1976, IIyushin and Lensky, 1968, Ohashi and Tokuda, 1973 and Meguid and Malvern, 1983. In our studies, the investigators have shown that these differences can be explained by the presence of plastic anisotropy in the extruded tubular Al6061-T6 material. Considering Barlat anisotropic yield function, the deviation of effective strain vs. equivalent strain of combined tension torsion experiment to uniaxial tension case improved from +/-14% (von Mises) to +/- 4%, as shown in Figs. 5.8-5.12.

As shown in Figs. 5.15 and 5.16, prediction of the torsional specimen response during loading shows that (a) isotropic yield models underestimate by ~ 10% the experimental results for MT1 and substantially over-estimate the response by ~ 25% for MT2. When using the Barlat Yld91 anisotropic yield criterion, the deviation is less than 5% for both specimens, again demonstrating the importance of anisotropy for the accurate prediction of material response in extruded material systems. This observation is consistent with previous studies by Fourmeau et al. (2011) and Tardif & Kyriakides (2012).

Regarding the choice of yield criteria, the investigators selected the Barlat Yld9 (1991) anisotropic yield function with six material parameters (rather than the Yld2000-2d, Yld 2004-8d or Yld2004-18p (2003,2005) models) for two reasons. First, the diameter of two original bars was 28.575 mm, which was relatively small, limiting the investigators ability to extract usable specimens from different directions for parameter identification. Secondly, the longitudinal extrusion process of the Al6061-T6 tubes develops similar material responses in all circumferential directions, limiting the number of required specimen orientations necessary for anisotropic model calibration. Based on the results shown in Figs. 5.15 and 5.16, the selection of the Yld91 criterion reduced the complexity of the experimental program while also providing excellent agreement with experimental observations.

CHAPTER 7

SUMMARY, CONCLUSIONS AND RECOMMENDATIONS FOR FUTURE WORK

7.1 SUMMARY AND CONCLUSION

In this study, the anisotropic behavior of 28.575 mm diameter longitudinally extruded Al 6061-T6 cylindrical bars is studied both experimentally and with models to predict the elastic-plastic deformation of the material when subjected to combinations of uniaxial tension and torsion. Experimental surface strain measurements in the thin-walled tubular specimens were with StereoDIC, and the stresses were calculated using measured axial and torsion loads with the measured specimen geometry. In addition, the elastic, plastic, and total shear strain components are obtained theoretically using multiple yield criteria and incremental plasticity, with StereoDIC providing the experimentally measured total strains for extruded tubular specimens subjected to applied axial and torsional loads. Results from the combined experimental-modeling effort are summarized as follows;

- Uniaxial tension, simple torsion, and combined tension-torsion experiments are performed on a series of specially machined tubular and dog-boned rectangular specimens extracted from a longitudinally extruded Al6061-T6 cylindrical rod.
- StereoDIC is used extensively to identify anomalies in the specimen geometry and/or mechanical loading and quantify the full-field surface deformations on the

outer surface in the gage section of each tubular specimen and each radially oriented dog bone specimen.

- The Von Mises, Barlat anisotropic, and uniaxial data for effective stress versus measured equivalent strain are shown to be the same in the elastic regime, regardless of the type of loading applied to the specimen.
- The Von Mises effective stress at yielding is a strong function of the tension-torsion ratio, β, with subsequent hardening being similar in each case.
- The anisotropic yield function developed by Barlat et al. (1991) is used to model the response of the extruded aluminum material, with the anisotropic model parameters are quantified using experimental data obtained from samples extracted from various orientations from the Al6061-T6 rods. Data indicated that both extruded Al6061-T6 materials are significantly anisotropic, with the longitudinal yield stress deviating from the radial yield behavior in the extruded material. Since the extrusion process is circumferentially symmetric, yield stresses in all radial directions are expected to be similar.
- The calibrated anisotropic yield function developed by Barlat et al. (1991) is used to model the response of the extruded aluminum material by performing an additional set of independent experiments.
- In general, the Barlat model predictions are within +/- 4% of the uniaxial data for all tension torsion ratios, β, whereas the von Mises results overpredict the uniaxial results for all β, The largest offset using the von Mises effective stress is +14% for simple torsion, $\beta = \infty$, eventually matching the uniaxial results for tension loading when $\beta = 0$.

- By determining the isotropic hardening parameters for both aluminum bars, the von Mises isotropic yield function and the Barlat Yld91 anisotropic yield function are constructed with power-law hardening and then used with and the incremental theory of plasticity to develop separate constitutive models to predict the elastoplastic behavior of the materials.
- Predictions obtained using a numerical program implement the Barlat Yld91 anisotropic yield function are in excellent agreement with simple torsion experiments for both materials and within +/- 5% for generally mixed tension torsion loading for the MT1 material. In particular, results show the von Mises isotropic yield function will substantially under-estimate or over-estimate the yield response of the MT1 and MT2 extruded materials, respectively.

7.2 RECOMMENDATION

Regarding the theoretical and experimental anisotropic and hardening behavior described in this work, the following areas can be potential future research topics.

- The theory and the corresponding numerical implementation program should be extended to study the effectiveness of incremental plasticity theory when performing mixed mode tension torsion loading using anisotropic yield functions.
- The effective strain formulation coding can be built with python software and can be integrated with the digital image correlation software for faster data analysis.
- This research only covers the effectiveness of isotropic and Barlat anisotropic yield functions on uniaxial, proportional, and simple torsion cases. It would be ideal if

experimental results with non-proportional loading cases could be checked and the accuracy of existing anisotropic and isotropic yield function clearly delineated.

- During non-proportional tension-torsion test experiments, the current fixtured grip can not hold the displacement or reliably twist the specimen as programmed during the entire experimental process. To continue the experimental procedure, the fixtures should be modified to perform experiments under either displacement or twist control.
- A long-term goal would be to develop numerical and theoretical models considering anisotropy for non-proportional tension torsion loading and provide accurate experimental data for continuous improvement in the models.

REFERENCES

Achani, D., Hopperstad, O. S., & Lademo, O. G. (2009). Behaviour of extruded aluminium alloys under proportional and non-proportional strain paths. Journal of Materials Processing Technology, 209(10), 4750-4764.

Asnafi, N., Shams, T., Aspenberg, D., & Öberg, C. (2019). 3D metal printing from an industrial perspective—product design, production, and business models. *BHM Berg-und Hüttenmännische Monatshefte*, *164*(3), 91-100.

Avril, S., Pierron, F., Pannier, Y., & Rotinat, R. (2008). Stress reconstruction and constitutive parameter identification in plane-stress elasto-plastic problems using surface measurements of deformation fields. Experimental Mechanics, 48(4), 403-419.

https://aviation.stackexchange.com/questions/35441/why-are-the-leading-edges-on-the-boeing-787-made-from-aluminum

Bai, Y., Wierzbicki, T., 2008. A new model of metal plasticity and fracture with pressure and lode dependence. International Journal of Plasticity 24, 1071–1096.

Barlat, F., & Lian, K. (1989). Plastic behavior and stretchability of sheet metals. Part I: A yield function for orthotropic sheets under plane stress conditions. International journal of plasticity, 5(1), 51-66.

Barlat, F., Aretz, H., Yoon, J. W., Karabin, M. E., Brem, J. C., & Dick, R. E. (2005). Linear transfomation-based anisotropic yield functions. International Journal of Plasticity, 21(5), 1009-1039.

Barlat, F., Becker, R. C., Hayashida, Y., Maeda, Y., Yanagawa, M., Chung, K., & Hattori, S. (1997). Yielding description for solution strengthened aluminum alloys. International Journal of Plasticity, 13(4), 385-401.

Barlat, F., Brem, J. C., Yoon, J. W., Chung, K., Dick, R. E., Lege, D. J., & Chu, E. (2003). Plane stress yield function for aluminum alloy sheets—part 1: theory. International Journal of Plasticity, 19(9), 1297-1319.

Barlat, F., Lege, D. J., & Brem, J. C. (1991). A six-component yield function for anisotropic materials. International journal of plasticity, 7(7), 693-712.

Barlat, F., Maeda, Y., Chung, K., Yanagawa, M., Brem, J. C., Hayashida, Y., ... & Becker, R. C. (1997). Yield function development for aluminum alloy sheets. Journal of the Mechanics and Physics of Solids, 45(11-12), 1727-1763.

Batterman, S. C. (1968). Strength of materials: By AA Ilyushin and VS Lensky, published by Pergamon Press, Oxford, 1967; 320 pp., 249 illus.; price:£ 6.10. 0, US $20.0.

Bauschinger, J. (1881). Change of position of the elastic limit under cyclical variations of stress. Mitteilungen des Mechanisch-Technischen Laboratorium.

Bell, J. F. (2013). The physics of large deformation of crystalline solids (Vol. 14). Springer Science & Business Media.

Bertsch, P. K., & Findley, W. N. (1962). An experimental study of subsequent yield surfaces. corners, normality, Bauschinger and allied effects (No. TR27). BROWN UNIV PROVIDENCE RI.

Bland, D. R. (1957). The associated flow rule of plasticity. Journal of the Mechanics and Physics of Solids, 6(1), 71-78.

Bron, F., & Besson, J. (2004). A yield function for anisotropic materials application to aluminum alloys. International Journal of Plasticity, 20(4-5), 937-963.

Budiansky, B. (1958). A reassessment of deformation theories of plasticity. HARVARD UNIV CAMBRIDGE MA.

Cazacu, O., Plunkett, B., & Barlat, F. (2006). Orthotropic yield criterion for hexagonal closed packed metals. International Journal of Plasticity, 22(7), 1171-1194.

Chen, F., Chen, X., Xie, X., Feng, X., & Yang, L. (2013). Full-field 3D measurement using multi-camera digital image correlation system. Optics and Lasers in Engineering, 51(9), 1044-1052.

Chen, K., Scales, M., & Kyriakides, S. (2019). Material response, localization and failure of an aluminum alloy under combined shear and tension: Part II analysis. International Journal of Plasticity, 120, 361-379.

Chu, T. C., Ranson, W. F., & Sutton, M. A. (1985). Applications of digital-image-correlation techniques to experimental mechanics. *Experimental mechanics*, *25*(3), 232-244.

Coppieters, S., Cooreman, S., Sol, H., Van Houtte, P., & Debruyne, D. (2011). Identification of the post-necking hardening behaviour of sheet metal by

comparison of the internal and external work in the necking zone. Journal of Materials Processing Technology, 211(3), 545-552.

Coppieters, S., & Kuwabara, T. (2014). Identification of post-necking hardening phenomena in ductile sheet metal. Experimental mechanics, 54(8), 1355-1371.

Correlated Solutions, Inc., https://www.correlatedsolutions.com/ (Accessed June 1st, 2020).

Del Rey Castillo, E., Allen, T., Henry, R., Griffith, M., & Ingham, J. (2019). Digital image correlation (DIC) for measurement of strains and displacements in coarse, low volume-fraction FRP composites used in civil infrastructure. Composite Structures, 212, 43-57.

Dzaye, E. D., Tsangouri, E., Spiessens, K., De Schutter, G., & Aggelis, D. G. (2019). Digital image correlation (DIC) on fresh cement mortar to quantify settlement and shrinkage. Archives of Civil and Mechanical Engineering, 19, 205-214.

Elliotis, M. C. (2013). A Finite Element Approach for the Elastic-Plastic Behavior of a Steel Pipe Used to Transport Natural Gas. In Conference Papers in Energy (Vol. 2013). Hindawi.

Esmaeilpour, R., Kim, H., Park, T., Pourboghrat, F., & Mohammed, B. (2017). Comparison of 3D yield functions for finite element simulation of single point incremental forming (SPIF) of aluminum 7075. International Journal of Mechanical Sciences, 133, 544-554.

Esmaeilpour, R., Kim, H., Park, T., Pourboghrat, F., Xu, Z., Mohammed, B., & Abu-Farha, F. (2018). Calibration of Barlat Yld2004-18P yield function using CPFEM and 3D

RVE for the simulation of single point incremental forming (SPIF) of 7075-O aluminum sheet. International Journal of Mechanical Sciences, 145, 24-41.

Fjeldly, A., & Roven, H. J. (1996). Observations and calculations on mechanical anisotropy and plastic flow of an AlZnMg extrusion. Acta materialia, 44(9), 3497-3504.

Fourmeau, M., Børvik, T., Benallal, A., Lademo, O. G., & Hopperstad, O. S. (2011). On the plastic anisotropy of an aluminium alloy and its influence on constrained multiaxial flow. International journal of plasticity, 27(12), 2005-2025.

G. Geymonat and S. Pagano. Identification of mechanical properties by displacement field measurement: A variational approach. Meccanica, 38(5):535–545, October 2003.

Giagmouris, T., Kyriakides, S., Korkolis, Y. P., & Lee, L. H. (2010). On the localization and failure in aluminum shells due to crushing induced bending and tension. International journal of solids and structures, 47(20), 2680-2692.

Gotoh, M. (1977). A theory of plastic anisotropy based on a yield function of fourth order (plane stress state)—I. International Journal of Mechanical Sciences, 19(9), 505-512.

Haltom, S. S., Kyriakides, S., & Ravi-Chandar, K. (2013). Ductile failure under combined shear and tension. International Journal of Solids and Structures, 50(10), 1507-1522.

Hecker, S. S. (1976). Experimental studies of yield phenomena in biaxially loaded metals (No. LA-UR-76-1413; CONF-761107-1). Los Alamos Scientific Lab., NM (USA).

Helfrick, M. N., Niezrecki, C., Avitabile, P., & Schmidt, T. (2011). 3D digital image correlation methods for full-field vibration measurement. Mechanical systems and signal processing, 25(3), 917-927.

Helm, J. D., Sutton, M. A., & McNeill, S. R. (2003). Deformations in wide, center-notched, thin panels, part I: three-dimensional shape and deformation measurements by computer vision. Optical Engineering, 42(5), 1293-1306.

Hencky, H. (1924). Zur Theorie plastischer Deformationen und der hierdurch im Material hervorgerufenen Nachspannungen. ZAMM-Journal of Applied Mathematics and Mechanics/Zeitschrift für Angewandte Mathematik und Mechanik, 4(4), 323-334.

Hill, R. (1948). A theory of the yielding and plastic flow of anisotropic metals. Proceedings of the Royal Society of London. Series A. Mathematical and Physical Sciences, 193(1033), 281-297.

Hill, R. (1979, January). Theoretical plasticity of textured aggregates. In Mathematical Proceedings of the Cambridge Philosophical Society (Vol. 85, No. 1, pp. 179-191). Cambridge University Press.

Hill, R. (1990). Constitutive modelling of orthotropic plasticity in sheet metals. Journal of the Mechanics and Physics of Solids, 38(3), 405-417.

Hill, R. (1993). A user-friendly theory of orthotropic plasticity in sheet metals. International Journal of Mechanical Sciences, 35(1), 19-25.

Hill, R. (1998). The mathematical theory of plasticity (Vol. 11). Oxford university press.

Hodge Jr, P. G. (1957). A new method of analyzing stress and strains in work hardening solids. J. appl. Mech., 24, 482.

Hollomon, J. H. (1945). Tensile deformation. Aime Trans, 12(4), 1-22.

Hosford, W.F., 2006. The anisotropy of aluminum and aluminum alloys. Journal of the Minerals, Metals and Materials Society 58 (5), 70–74.

Huňady, R., Pavelka, P., & Lengvarský, P. (2019). Vibration and modal analysis of a rotating disc using high-speed 3D digital image correlation. Mechanical Systems and Signal Processing, 121, 201-214.

https://www.nasa.gov/centers/johnson/pdf/584733main_Wings-ch4g-pgs270-285.pdf (Accessed September 1st, 2021).

https://aviation.stackexchange.com/questions/35441/why-are-the-leading-edges-on-the-boeing-787-made-from aluminum?fbclid=IwAR0WvTSMruqOaM3xC5PLtUik0PRnxKF0EZKohmMslwRLjYxpa8Cy8XijT9Q (Accessed September 1st, 2021).

http://www1.us.elsevierhealth.com/books.elsevier/companionsites/JenkinsKhanna/mmd/yieldpoint/yieldpointa.html (Accessed September 1st, 2021).

https://en.wikipedia.org/wiki/Von_Mises_yield_criterion (Accessed October 1st, 2020).

https://www.hydro.com/en-US/products-and-services/extruded-profiles/north-america-resources/extruded-aluminum-products/aluminum-extrusion-alloys/6061-aluminum-properties--uses/(Accessed September 1st, 2021).

https://www.thomasnet.com/articles/metals-metal-products/6061-aluminum/ (Accessed September 1st, 2021).

Ilyushin, A. A. (1947). The Theory for Small Elastic-Plastic Deformations. Applied Mathematics Group, Brown University.

Ilyushin, A. A. (1961). On the postulate of plasticity.

Ilyushin, A. A. (1963). Plasticity: Fundamentals of general mathematical theory. Akademiia Nauk, SSSR.

Ilyushin, A. A. (1947). Theory of plasticity at simple loading of the bodies exhibiting plastic hardening. Prikl. Mat. Mekh, 11, 291.

Il'Iushin, A. A. (1961). On the postulate of plasticity. Journal of Applied Mathematics and Mechanics, 25(3), 746-752.

Ilyushin, A. A. (1963). Plasticity: Fundamentals of general mathematical theory. Академия Наук, СССР.

Ivey, H. J. (1961). Plastic stress–strain relations and yield surfaces for aluminium alloys. Journal of Mechanical Engineering Science, 3(1), 15-31.

Kachanov, L. M. (1971). Foundations of the Theory of Plasticity (Vol. 12). North-Holland.

Lubliner, J. (1990).Plasticity Theory. New York: Macmillan Publishing Company.

Kahn-Jetter, Z. L., & Chu, T. C. (1990). Three-dimensional displacement measurements using digital image correlation and photogrammic analysis. Experimental Mechanics, 30(1), 10-16.

Karafillis, A. P., & Boyce, M. C. (1993). A general anisotropic yield criterion using bounds and a transformation weighting tensor. Journal of the Mechanics and Physics of Solids, 41(12), 1859-1886.

Khan, A. S., Kazmi, R., Pandey, A., & Stoughton, T. (2009). Evolution of subsequent yield surfaces and elastic constants with finite plastic deformation. Part-I: A very low

work hardening aluminum alloy (Al6061-T6511). International Journal of Plasticity, 25 (9), 1611-1625.

Khan, A. S., Pandey, A., & Stoughton, T. (2010). Evolution of subsequent yield surfaces and elastic constants with finite plastic deformation. Part II: A very high work hardening aluminum alloy (annealed 1100 Al). International Journal of Plasticity, *26* (10), 1421-1431.

Kelly, P. (2013). Solid Mechanics Part II: Engineering Solid Mechanicssmall strain. The University of Auckland.

Kim, J. H., Serpantié, A., Barlat, F., Pierron, F., & Lee, M. G. (2013). Characterization of the post-necking strain hardening behavior using the virtual fields method. International Journal of Solids and Structures, 50(24), 3829-3842.

Kleemola, H. J., & Nieminen, M. A. (1974). On the strain-hardening parameters of metals. Metallurgical transactions, 5(8), 1863-1866.

Kondori, B., Madi, Y., Besson, J., & Benzerga, A. A. (2019). Evolution of the 3D plastic anisotropy of HCP metals: experiments and modeling. International Journal of Plasticity, 117, 71-92.

Korkolis, Y. P., & Kyriakides, S. (2008a). Inflation and burst of anisotropic aluminum tubes for hydroforming applications. International Journal of Plasticity, 24(3), 509-543.

Korkolis, Y. P., & Kyriakides, S. (2008b). Inflation and burst of aluminum tubes. Part II: an advanced yield function including deformation-induced anisotropy. International journal of plasticity, 24(9), 1625-1637.

Korkolis, Y. P., & Kyriakides, S. (2011). Hydroforming of anisotropic aluminum tubes: Part II analysis. International journal of mechanical sciences, 53(2), 83-90.

Korkolis, Y.P., Kyriakides, S., 2009. Path-dependent failure of inflated aluminum tubes. Int. J. Plast. 25, 2059–2080.

Korkolis, Y.P., Kyriakides, S., Giagmouris, T., Lee, L.-H., 2010. Constitutive modeling and rupture predictions of Al-6061-T6 tubes under biaxial loading paths. ASME J. Appl. Mech. 77 (5), 23, 064501, 1–5.

Kuwabara, T., Mori, T., Asano, M., Hakoyama, T., & Barlat, F. (2017). Material modeling of 6016-O and 6016-T4 aluminum alloy sheets and application to hole expansion forming simulation. International Journal of Plasticity, 93, 164-186.

Lademo, O. G., Hopperstad, O. S., & Langseth, M. (1999). An evaluation of yield criteria and flow rules for aluminium alloys. International Journal of Plasticity, 15(2), 191-208.

Levy, M. (1870). Mémoire sur les équations générales des mouvements intérieurs des corps solides ductiles au delà des limites où l'élasticité pourrait les ramener à leur premier état. *CR Acad. Sci. Paris*, *70*, 1323-1325.

Liu, M., Guo, J., Li, Z., Hui, C. Y., & Zehnder, A. T. (2019). Crack propagation in a PVA dual-crosslink hydrogel: Crack tip fields measured using digital image correlation. Mechanics of Materials, 138, 103158.

Logan, R. W., & Hosford, W. F. (1980). Upper-bound anisotropic yield locus calculations assuming< 111>-pencil glide. International Journal of Mechanical Sciences, 22(7), 419-430.

Lubarda, V. A., On the partition of rate of deformation in crystal plasticity, Int. J. Plasticity, Vol. 15, pp. 721-736 (1999).

Lubarda, V.A. and Lee, E. H., A correct de_nition of elastic and plastic deformation and its computational signi_cance, J. Appl. Mech., Vol. 48, pp. 35-40 (1981).

Lubarda, V. A. and Krajcinovic, D., Some fundamental issues in rate theory of damage-elastoplasticity, Int. J. Plasticity, Vol. 11, pp. 763-797 (1995).

Ludwik, P. (1909). Elemente der technologischen Mechanik. Springer.

Ludwigson, D. C. (1971). Modified stress-strain relation for FCC metals and alloys. Metallurgical Transactions, 2(10), 2825-2828.

Luo, P. F., Chao, Y. J., Sutton, M. A., & Peters Iii, W. H. (1993). Accurate measurement of three-dimensional deformations in deformable and rigid bodies using computer vision. Experimental Mechanics, 33(2), 123-132.

Luo, P. F., Chao, Y. J., & Sutton, M. A. (1994). Application of stereo vision to three-dimensional deformation analyses in fracture experiments. Optical Engineering, 33(3), 981-990.

Maier, G., & Hueckel, T. (1979, April). Nonassociated and coupled flow rules of elastoplasticity for rock-like materials. In International Journal of Rock Mechanics and Mining Sciences & Geomechanics Abstracts (Vol. 16, No. 2, pp. 77-92). Pergamon.

Meguid, S. A., & Malvern, L. E. (1983). An experimental investigation into the plastic flow and strain hardening of mild steel under proportional and abruptly changing

deformation paths at a controlled rate. Journal of Engineering Materials and Technology, 105(3), 147-154.

Mises, R. V. (1913). Mechanik der festen Körper im plastisch-deformablen Zustand. Nachrichten von der Gesellschaft der Wissenschaften zu Göttingen, Mathematisch-Physikalische Klasse, 1913, 582-592.

Mooney, B., Kourousis, K. I., Raghavendra, R., & Agius, D. (2019). Process phenomena influencing the tensile and anisotropic characteristics of additively manufactured maraging steel. Materials Science and Engineering: A, 745, 115-125.

Nicholas, T. (1981). Tensile testing of materials at high rates of strain. Experimental mechanics, 21(5), 177-185.

Ohashi, Y., & Tokuda, M. (1973). Precise measurement of plastic behaviour of mild steel tubular specimens subjected to combined torsion and axial force. Journal of the Mechanics and Physics of Solids, 21(4), 241-244.

Pahlevanpour, A. H., Behravesh, S. B., Adibnazari, S., & Jahed, H. (2019). Characterization of anisotropic behaviour of ZK60 extrusion under stress-control condition and notes on fatigue modeling. International Journal of Fatigue, 127, 101-109.

Pannier, Y., Avril, S., Rotinat, R., & Pierron, F. (2006). Identification of elasto-plastic constitutive parameters from statically undetermined tests using the virtual fields method. Experimental Mechanics, 46(6), 735-755.

Papasidero, J., Doquet, V., & Mohr, D. (2015). Ductile fracture of aluminum 2024-T351 under proportional and non-proportional multiaxial loading: Bao–Wierzbicki results revisited. International Journal of Solids and Structures, 69, 459-474.

Peters, W. H., Ranson, W. F. 1981. Digital imaging techniques in experimental stress analysis. Opt. Eng. 21: 427-31.

Peth, S., Nellesen, J., Fischer, G., & Horn, R. (2010). Non-invasive 3D analysis of local soil deformation under mechanical and hydraulic stresses by μCT and digital image correlation. Soil and Tillage Research, 111(1), 3-18.

Phillips, A., Liu, C. S., & Justusson, J. W. (1972). An experimental investigation of yield surfaces at elevated temperatures. *Acta Mechanica*, *14*(2-3), 119-146.

Phillips, A., & Juh-Ling, T. (1972). The effect of loading path on the yield surface at elevated temperatures. International Journal of Solids and Structures, 8(4), 463-474.

Phillips, A., Tang, J. L., & Ricciuti, M. (1974). Some new observations on yield surfaces. Acta Mechanica, 20(1-2), 23-39.

Phillips, A., & Moon, H. (1977). An experimental investigation concerning yield surfaces and loading surfaces. Acta Mechanica, 27(1-4), 91-102.

Plunkett, B., Cazacu, O., & Barlat, F. (2008). Orthotropic yield criteria for description of the anisotropy in tension and compression of sheet metals. International Journal of Plasticity, 24(5), 847-866.

Psylotech Incorporated, 2006, https://www.psylotech.com/μs/(Accessed June 1st , 2020).

Prager, W. (1938). On isotropic materials with continuous transition from elastic to plastic state. Proc. 5th Internat. Congr. Appl. Mech., Cambridge (Mass.), 234-237.

Prager, W. (1956). A new methods of analyzing stresses and strains in work hardening plastic solids. J. Appl. Mech.(ASME), 23, 493-496.

Rahmaan, T., Noder, J., Abedini, A., Zhou, P., Butcher, C., & Worswick, M. J. (2020). Anisotropic plasticity characterization of 6000-and 7000-series aluminum sheet alloys at various strain rates. International Journal of Impact Engineering, 135, 103390.

Ramberg, W., & Osgood, W. R. (1943). Description of stress-strain curves by three parameters.

Saint-Venant, D. B. (1870). Sur l'établissement des équations des mouvements intérieurs opérés dans les corps solides ductiles au delà des limites où l'élasticité pourrait les ramener á leur premier état/B. De Saint-Venant. Comptes Rendus de l'Ac. des Sciences, 473-480.

Scales, M., Tardif, N., & Kyriakides, S. (2016). Ductile failure of aluminum alloy tubes under combined torsion and tension. International Journal of Solids and Structures, 97, 116-128.

Scales, M., Chen, K., & Kyriakides, S. (2019). Material response, localization, and failure of an aluminum alloy under combined shear and tension: Part I experiments. International Journal of Plasticity, 120, 340-360.

Schreier, H. W., Orteu, J. J., & Sutton, M. A. (2009). Image correlation for shape, motion and deformation measurements. Springer US.

Seidt, J. D., & Gilat, A. (2013). Plastic deformation of 2024-T351 aluminum plate over a wide range of loading conditions. International journal of solids and structures, 50(10), 1781-1790.

Shao, X., Dai, X., Chen, Z., & He, X. (2016). Real-time 3D digital image correlation method and its application in human pulse monitoring. Applied optics, 55(4), 696-704.

Sutradhar, A., Park, J., Carrau, D., & Miller, M. J. (2014). Experimental validation of 3D printed patient-specific implants using digital image correlation and finite element analysis. Computers in biology and medicine, 52, 8-17.

Sutton, M. A., Wolters, W. J., Peters, W. H., Ranson, W. F., & McNeill, S. R. (1983). Determination of displacements using an improved digital correlation method. Image and vision computing, 1(3), 133-139.

Sutton, M. A., Mingqi, C., Peters, W. H., Chao, Y. J., & McNeill, S. R. (1986). Application of an optimized digital correlation method to planar deformation analysis. Image and Vision Computing, 4(3), 143-150.

Sutton, M. A., Yan, J. H., Tiwari, V., Schreier, H. W., & Orteu, J. J. (2008). The effect of out-of-plane motion on 2D and 3D digital image correlation measurements. Optics and Lasers in Engineering, 46(10), 746-757.

Sutton, M. A., Helm, J. D., & Boone, M. L. (2001). Experimental study of crack growth in thin sheet 2024-T3 aluminum under tension-torsion loading. International journal of fracture, 109(3), 285-301.

Sutton, M. A., Yan, J. H., Deng, X., Cheng, C. S., & Zavattieri, P. (2007). Three-dimensional digital image correlation to quantify deformation and crack-opening displacement in ductile aluminum under mixed-mode I/III loading. Optical Engineering, 46(5), 051003.

Sutton, M. A., Deng, X., Liu, J., & Yang, L. (1996). Determination of elastic-plastic stresses and strains from measured surface strain data. Experimental Mechanics, 36(2), 99-112.

Tardif, N., & Kyriakides, S. (2012). Determination of anisotropy and material hardening for aluminum sheet metal. International Journal of Solids and Structures, 49(25), 3496-3506.

Tresca, H. (1864). Memoire sur l'écoulement des solides à de forte pressions. Acad. Sci. Paris, 2(1), 59.

Swift, H.W., 1952. Plastic instability under plane stress. J. Mech. Phys. Solids 1, 1–18.

Voce, E., 1948. The relationship between stress and strain for homogeneous deformation. J. Inst. Met. 74, 537–562.

van den Boogaard, T., Havinga, J., Belin, A., & Barlat, F. (2016). Parameter reduction for the Yld2004-18p yield criterion. International journal of material forming, 9(2), 175-178.

Yan, J. H., Sutton, M. A., Deng, X., & Cheng, C. S. (2007). Mixed-mode fracture of ductile thin-sheet materials under combined in-plane and out-of-plane loading. International Journal of Fracture, 144(4), 297-321.

Yasmeen, F., Rajan, S., Sutton, M. A., & Schreier, H. W. (2017). Experimental study of measurement errors in 3d-DIC due to out-of-plane specimen rotation. In International Digital Imaging Correlation Society (pp. 211-215). Springer, Cham.

Yasmeen, F., Balcaen, R., Sutton, M. A., Debruyne, D., Rajan, S., & Schreier, H. W. (2018). Sensitivity of in-plane strain measurement to calibration parameter for out-of-plane specimen rotations. Experimental Mechanics, 58(7), 1115-1132.

Yasmeen, F., Sutton, M. A., Rajan, S., Schreier, H., & Campbell, A. (2021). Effect of surface normal variability on local surface strain measurements in StereoDIC. Optics and Lasers in Engineering, 138, 106373.

Yasmeen, F., Sutton, M.A., A Campbell. (2021), Investigation of Plastic Flow and Strain Hardening in Extruded Cylindrical Al6061-T6 Material: Implementation of Stereo Digital Image Correlation for In-plane Strain Measurements with Tension-Torsion Loading. Experimental Mechanics (Under Review)

Yasmeen F., M. A Sutton, X. Deng, M. Ryan, and A. P. Reynolds (2021), Parameter estimation and application of anisotropic yield criteria for cylindrical aluminum extrusions: Theoretical developments and StereoDIC measurements. Applied Mechanics(under review).

Zhou, X. P., Wang, Y. T., Zhang, J. Z., & Liu, F. N. (2019). Fracturing behavior study of three-flawed specimens by uniaxial compression and 3D digital image correlation: sensitivity to brittleness. Rock Mechanics and Rock Engineering, 52(3), 691-718.

Ziegler, H. (1959). A modification of Prager's hardening rule. Quarterly of Applied mathematics, 17(1), 55-65.